

Deformation-induced damage investigated through deep learning and microscale observations

Von der Fakultät für Georessourcen und Materialtechnik der
Rheinisch-Westfälischen Technischen Hochschule Aachen

zur Erlangung des akademischen Grades eines

Doktors der Ingenieurwissenschaften

genehmigte Dissertation

vorgelegt von

M. Sc. Carl F. Kusche

aus Köln

Berichter: Univ.-Prof. Dr. Sandra Korte-Kerzel
Prof. Dr.-Ing. Dr.-Ing. E.h. A. Erman Tekkaya

Tag der mündlichen Prüfung: 06.05.2021

Diese Dissertation ist auf den Internetseiten der Universitätsbibliothek online verfügbar.

Declaration on publications

This thesis includes the following articles that have been published in international peer-reviewed journals:

Publication #1

C. Kusche, T. Reclik, M. Freund, T. Al-Samman, U. Kerzel, S. Korte-Kerzel, Large-area, high-resolution characterisation and classification of damage mechanisms in dual-phase steel using deep learning, PloS one 14(5) (2019) e0216493.

Publication #2

C.F. Kusche, F. Pütz, S. Münstermann, T. Al-Samman, S. Korte-Kerzel, On the effect of strain and triaxiality on void evolution in a heterogeneous microstructure – A statistical and single void study of damage in DP800 steel, Materials Science and Engineering: A 799 (2021) 140332.

Publication #3

R. Meya, C.F. Kusche, C. Löbbe, T. Al-Samman, S. Korte-Kerzel, A.E. Tekkaya, Global and High-Resolution Damage Quantification in Dual-Phase Steel Bending Samples with Varying Stress States, Metals 9(3) (2019) 319.

Publication #4

C.F. Kusche, J.S.K.-L. Gibson, M.A. Wollenweber, S. Korte-Kerzel, On the mechanical properties and deformation mechanisms of manganese sulphide inclusions, Materials & Design (2020) 10880

D82 (Diss.RWTH Aachen University, 2021)

Danksagung

Wissenschaftliches Arbeiten lebt von dem Zusammenspiel vieler, hoch motivierter und kluger Köpfe - in diesem Sinne entsteht eine wissenschaftliche Arbeit niemals im Alleingang. Die in dieser Arbeit enthaltenen Publikationen sind ohne Ausnahme von solchen Wissenschaftlern in enger Zusammenarbeit erstellt worden. Ich danke daher zunächst sehr herzlich allen Co-Autoren dieser Publikationen für ihre Beiträge, die Diskussionen und Ideen auf dem Wege dorthin und das positive und konstruktive Umfeld, in dem diese Arbeiten entstanden.

Danken möchte ich Prof. Sandra Korte-Kerzel und Prof. A. Erman Tekkaya, sowohl für ihre Rolle als Prüfer dieser Dissertation, als auch für die Konzipierung des zu Grunde liegenden Projektes und ihre Betreuung und Unterstützung in den letzten Jahren, und die Schaffung einer positiven und produktiven wissenschaftlichen Arbeitsatmosphäre, am Institut wie im Transregio 188.

Aus dem Institut für Metallkunde und Materialphysik möchte ich einige Personen besonders hervorheben, die in meiner Promotionszeit von großem Wert für mich und meine wissenschaftliche Arbeit waren. Dr. Talal Al-Samman, für seine persönliche, freundschaftliche und vertrauensvolle Betreuung meiner Arbeit als Projektleiter. Dr. James Gibson, für seinen unermüdlichen Einsatz, auch in spontan entstandenen Projektideen. Frau Doreen Andre und Frau Fatim-Zahra Mouhib, für akademische Gespräche und Kaffeepausen, in denen mehr als nur eine dieser Ideen entstand. Herrn Gerhard Schütz, für die schwindelerregend exakte Fertigung von jeder noch so ungewöhnlich anmutenden Probengeometrie, stellvertretend für das gesamte Team der mechanischen Werkstatt. Und zuletzt Prof. Dmitri A. Molodov, der in den Jahren, die ich an diesem Institut verbracht habe für mich ein vertrauenswürdiger Mentor und moralischer Rückhalt geworden ist – er war es, der mir die Begeisterung für die Metallphysik nahe brachte.

Dr. Konstantin D. Molodov danke ich für die Hilfe bei der Adaptierung seines Panorama-Stitching-Skriptes auf die Anwendung im Dualphasenstahl.

Das Konsortium des Transregio 188 war ebenfalls eine wertvolle und positive Umgebung für interdisziplinäre, wissenschaftliche Arbeit, von der Ebene der Doktoranden bis zur Leitung des TRR durch Prof. A. E. Tekkaya, dem mein besonderer Dank für diese großartige Umgebung und Atmosphäre, sowie die stete Unterstützung, Würdigung und konstruktiver Kritik meiner Arbeit gilt. Aus dem TRR188 gilt weiterhin mein Dank Herrn Rickmer Meya, mit dem zusammen die Überbrückung der Skalen zwischen Umformtechnik und Metallphysik gelang. Außerdem danke ich Herrn Felix Pütz, mit dem durch gleichzeitig perfekte Kooperation wie anregende Konkurrenz stets neue Ideen dynamisch umgesetzt werden konnten.

Mein besonderer Dank gilt außerdem den Studenten, die in der Zeit mit mir gearbeitet haben. Auch auf dieser Ebene ergaben sich stets anregende, ideenreiche und produktive Gespräche, die die Arbeit an allen Projekten stets in entscheidendem Maße voranbrachten. Im Besonderen erwähnen möchte ich hier Herrn Maximilian A. Wollenweber, der zusätzlich zu seiner vor Begeisterung sprühenden Arbeitsweise ein echter Freund geworden ist. Mein ganz besonderer Dank gilt außerdem Frau Martina Freund, die in der gesamten Zeit meine rechte Hand war, jede noch so verrückte Idee mit umgesetzt hat, tausende von Schädigungsstellen sehen musste, hunderte von Proben präpariert hat und wissenschaftlich wie persönlich einen großen Beitrag zu dieser Arbeit geleistet hat.

Bedanken möchte ich mich außerdem bei meiner Familie, die mich auf dem Weg zur Promotion in unglaublichem Maße unterstützt und bestärkt hat.

Abstract

The occurrence of microstructural damage in the form of deformation-induced voids affects the properties and performance of a formed part on multiple scales. This process begins with the formation of microscale voids and ends with macroscopic failure due to accumulated damage during plastic deformation. It is because of this multi-scale effect, that the initiation and evolution of these deformation-induced voids needs to be viewed and analysed from a multi-scale point of view. Such an approach is expected to start with the mechanisms of plasticity in a mechanically heterogeneous microstructure, at the nanoscale, leading to the mechanisms of damage formation. To gain further insights about the formation of these types of deformation-induced damage, however, the viewpoint on these microscale events needs to be enlarged, gathering information about a whole plethora of damage sites, in order to achieve statistically sound assertions. Ideally, the scale can be enlarged in such a way that correlations to global parameters of the deformation process are possible, leading to a bridging of the scales from microstructural mechanisms to the order of magnitude required to engineer complete forming processes with respect to damage formation.

To achieve this bridging of scales between nanoscale investigations on damage mechanisms and damage quantification on the scale of a formed component, this work presents a complementary approach consisting of the characterisation of local plastic properties via nanomechanical experiments, and new methods for automated characterisation and quantification of deformation-induced voids, that has been developed as part of this dissertation, utilising automated SEM imaging and deep neural networks.

This dissertation consists of four research publications, three of which are concerned with the characterisation and quantification of emerging microstructural voids and their mechanisms of initiation and evolution in dual-phase steel DP800. A scale-bridging experimental and computational method that spans from automated imaging, void detection and mechanism classification utilising deep neural networks is introduced in **publication #1**. It therefore presents an approach to gain statistically relevant information about damage incidents and their originating mechanisms in a way that bridges the gap between the microscale mechanism and the global state and quantity of deformation-induced damage on the scale of a formed part. As such a method can be applied to larger scale specimens to quantify damage behaviour, it is used in **publication #2** to unravel the effects of the globally applied stress state in a systematic study on the influence of stress triaxiality on damage formation. Due to the large field of view, the previously assumed dependency could be proven for a real, heterogeneous microstructure, in which the evolution of a single void is dominated by the local stress state, exerted by local microstructural properties and morphology. Viewed in the statistically relevant ensemble of voids reached with this new approach, the expected dependency could be visualised. Having applied the approach to such a systematic study, it is applied to a technological forming process in **publication #3**, namely bending. Here, the effect of reduced triaxiality, due to superposed compressive stresses, on void formation could be proven due to the microscale measurements of single voids on an area large enough to be relevant to the scale of a sheet metal forming process. **Publication #4** is thematically concerned with characterising the plasticity of α -manganese sulphide (MnS), by applying the methods of nanoindentation and micropillar compression. As in many steels besides dual-phase steels, foreign phases like inclusions are a major cause for damage formation, the plasticity of such inclusions is of high interest to research and modelling on this mechanism of damage. MnS is a common inclusion phase in many case-hardened steels, which is why the

quantitative data on crystal plasticity gathered by this study is a vital addition to the research on how the plasticity of inclusions like MnS effect damage initiation.

As a whole, this work presents an approach to quantify deformation-induced damage on all scales, bringing a scientific benefit to the research on damage formation and its mechanisms through its considerably increased efficiency. It is applicable for researchers working on all steps in the chain of development for damage-tolerant materials and processes, and considers all length scales from the fundamentals of plasticity, applicable for crystal-plasticity simulations ultimately simulating the process of damage formation, to the research on the damage mechanisms itself - through its findings on the dominance of damage mechanisms and the observations on stress and strain dependence of initiation and growth. Finally, on the macroscopic scale of formed components, this approach originating from the microscale can be applied to make the quantification of damage in these parts more accurate and representative

Zusammenfassung

Das Auftreten von mikrostruktureller Schädigung in Form von verformungsinduzierten Poren beeinflusst die Eigenschaften und die Leistungsfähigkeit eines Bauteils auf mehreren Skalen. Dieser Prozess beginnt mit der Bildung von mikroskaligen Poren und endet mit makroskopischem Versagen aufgrund akkumulierter Schädigung während der plastischen Verformung. Aufgrund dieses Multiskaleneffekts muss die Entstehung und Entwicklung dieser verformungsinduzierten Poren mit einem Multi-Skalen-Ansatz betrachtet und analysiert werden. Ein solcher Ansatz beginnt mit den Mechanismen der Plastizität in einer mechanisch heterogenen Mikrostruktur auf der Nanoskala und führt zu den Mechanismen der Schädigung. Um weitere Erkenntnisse über die Entstehung dieser Arten von verformungsinduzierter Schädigung zu gewinnen, muss der Blickwinkel auf diese kleinskaligen Ereignisse jedoch erweitert werden, indem Informationen über eine ganze Fülle von Schädigungsstellen gesammelt werden, um statistisch fundierte Aussagen zu erhalten. Im Idealfall kann die Skala so vergrößert werden, dass Korrelationen zu globalen Parametern des Verformungsprozesses möglich sind, was zu einer Überbrückung der Skalen von mikrostrukturellen Mechanismen bis hin zu der Größenordnung führt, die für die schädigungskontrollierte Auslegung vollständiger Umformprozesse erforderlich ist.

Um diese Überbrückung der Skalen zwischen nanoskaligen Untersuchungen zu Schädigungsmechanismen und Schädigungsquantifizierung auf der Skala eines geformten Bauteils zu erreichen, wird in dieser Arbeit ein komplementärer Ansatz vorgestellt, der aus der Charakterisierung lokaler plastischer Eigenschaften mittels nanomechanischer Versuche und neuer Methoden zur automatisierten Charakterisierung und Quantifizierung von verformungsinduzierten Poren besteht, die im Rahmen dieser Dissertation unter Verwendung automatisierter REM-Bildgebung und neuronaler Netze entwickelt wurden.

Diese Dissertation besteht aus vier Forschungspublikationen, von denen sich drei mit der Charakterisierung und Quantifizierung von mikrostrukturellen Poren und deren Mechanismen der Entstehung und Evolution in Dualphasenstahl DP800 befassen. In **Publikation #1** wird eine skalenübergreifende Methode vorgestellt, die sich von der automatisierten Bildgebung über die Erkennung von Poren bis hin zur Klassifizierung der Mechanismen unter Verwendung von tiefen neuronalen Netzen erstreckt. Damit wird ein Ansatz vorgestellt, um statistisch relevante Informationen über Schädigung und deren Entstehungsmechanismen zu gewinnen, der die Lücke zwischen dem Mechanismus auf der Mikroskala und dem globalen Zustand und der Quantität der verformungsinduzierten Schädigung auf der Skala eines technologischen Bauteils überbrückt. Da eine solche Methode zur Quantifizierung des Schädigungsverhaltens auf Proben größeren Maßstabs angewendet werden kann, wird sie in **Publikation #2** verwendet, um die Auswirkungen des global angelegten Spannungszustands in einer systematischen Studie über den Einfluss der Spannungsmehrachsigkeit auf die Schädigungsbildung zu entschlüsseln. Aufgrund des vergrößerten Sichtfeldes konnte die zuvor angenommene Abhängigkeit für ein reales, heterogenes Gefüge nachgewiesen werden, in dem die Entwicklung einer einzelnen Pore durch den lokalen Spannungszustand dominiert wird, der durch lokale Gefügeeigenschaften und Morphologie ausgeübt wird. Betrachtet man das mit diesem neuen Ansatz aufgenommene statistisch relevante Ensemble von Poren, wird die erwartete Abhängigkeit sichtbar. Nach der Anwendung des Ansatzes auf eine solche systematische Untersuchung wird er in der **Publikation #3** auf den technologischen Umformprozess des Biegens von Blechen angewandt. Hier konnte die Auswirkung der reduzierten Spannungsmehrachsigkeit durch überlagerte Druckspannungen auf die Porenbildung durch die Messung einzelner Poren auf einer Fläche nachgewiesen

werden, die groß genug ist, um für den Maßstab eines Blechumformprozesses relevant zu sein. **Publikation #4** befasst sich thematisch mit der Charakterisierung der Plastizität von α -Mangansulfid (MnS) unter Anwendung nanomechanischer Methoden. Da in vielen Stählen außer Dualphasenstählen, Fremdphasen wie Einschlüsse eine Hauptursache für die Bildung von Schädigung sind, ist die Plastizität solcher Einschlüsse von hohem Interesse für die Erforschung und Modellierung dieses Schadensmechanismus. MnS ist eine häufige Einschlussphase in vielen Einsatzstählen, weshalb die in dieser Studie gesammelten quantitativen Daten zur Kristallplastizität eine wichtige Ergänzung für die Erforschung der Auswirkungen der Plastizität von Einschlüssen wie MnS auf die Schadensentstehung darstellen.

Insgesamt stellt diese Arbeit einen Ansatz zur Quantifizierung verformungsinduzierter Schädigung auf allen Skalen vor, der durch seine erheblich gesteigerte Effizienz einen wissenschaftlichen Nutzen für die Erforschung der Schädigungsbildung und ihrer Mechanismen bringt. Sie ist für Forscher anwendbar, die an allen Schritten in der Prozesskette für schädigungstolerante Materialien und Prozesse arbeiten, und berücksichtigt alle Längenskalen von den Grundlagen der Plastizität bis hin zur Erforschung der Schädigungsmechanismen selbst - durch ihre Erkenntnisse über die Dominanz von Schädigungsmechanismen und die Beobachtungen zur Spannungs- und Dehnungsabhängigkeit von Initiierung und Wachstum. Auf der makroskopischen Skala geformter Bauteile schließlich kann dieser aus der Mikroskala stammende Ansatz angewandt werden, um die Quantifizierung von Schädigungen in diesen Bauteilen genauer und repräsentativer zu machen

Table of contents

Declaration on publications	II
Danksagung.....	III
Abstract.....	IV
Zusammenfassung	VI
List of figures	IX
List of abbreviations	X
1. Motivation	1
2. Background on damage and deep learning	4
2.1 Definition of damage	4
2.2 Damage mechanisms in dual-phase steels.....	6
2.3 Deep learning in materials science.....	11
3. Materials and methods.....	12
3.1 Materials used in this work.....	12
3.2 Deep-learning-based characterisation of damage mechanisms.....	13
3.3 In- and ex-situ deformation	16
3.3 Nanoscale characterisation of damage mechanisms	17
4. Research publications.....	18
5. Conclusions	20
6. Outlook	21
Large-area, high-resolution characterisation and classification of damage mechanisms in dual-phase steel using deep learning.....	22
On the effect of strain and triaxiality on void evolution in a heterogeneous microstructure – A statistical and single void study of damage in DP800	45
Global and High-Resolution Damage Quantification in Dual-Phase Steel Bending Samples with Varying Stress States	58
On the mechanical properties and deformation mechanisms of manganese sulphide inclusions.....	76
Bibliography	84
Curriculum Vitae	89
List of publications	91

List of figures

Figure 1: Structure of this dissertation, consisting of four peer-reviewed research publications	2
Figure 2: Observed fundamental mechanisms of void formation in dual-phase steels (a-f), reproduced from [3] and patterns due to microstructural morphology, reproduced from [39]. (a) Martensite cracking, (b,c) Martensite-Ferrite interface decohesion (c from in-situ experiment), (d) damage to ferrite grain boundary, (e) void in grain interior, (f) void around inclusion. (g) “necklace”-type void pattern along narrow band of martensite, (h) large martensite cracks in a wide martensite band.	6
Figure 3: Effects of microstructural morphology on damage formation behaviour. (a) void patterns in two DP600 grades, the first image shows large voids in a martensite band in the middle of the sheet, while the other shows more homogeneous distribution of voids, reproduced from [41], (b) two dual-phase steels different ferrite grain sizes, coarse-grained (CG) and ultra-fine-grained (UFG), showing a tendency for large martensite cracks (CG) compared to nucleation and growth of smaller voids in and adjacent to martensite islands (UFG), reproduced from [29] .	7
Figure 4: Examples of nanomechanical testing for quantifying mechanical properties for damage initiation. a) Microcantilever-bending, determining the quantity of fracture toughness, reproduced from [65], b) micro-tensile testing of lath martensite, coupled to EBSD investigations, reproduced from [66], c) Micropillar-compression to determine active slip systems and their CRSS in ferrite, reproduced from [22] 10	
Figure 5: a) Stress-Strain curves of both dual-phase steels applied in this work, reproduced from [22]. b) SE-images of the two microstructures, with visibly “sharper” martensite morphology in Microstructure #1. Both images depict the RDxTD plane.....	12
Figure 6: Structure of the framework with both neural networks [15 - Publ. #1]	14
Figure 7: Examples of the formation of surface artefacts created in in-situ experiments, following the phase boundaries to martensite, in ferrite regions. (a) reproduced from [2], (b) reproduced from [26].....	16

List of abbreviations

AHSS	Advanced-High-Strength-Steels
BCC	Body-Centred Cubic
CRSS	Critical Resolved Shear Stress
DIC	Digital Image Correlation
DP (-steel)	Dual Phase Steel
EBSD	Electron-Backscatter-Diffraction
EDM	Electric-Discharge-Machining
EDX	Energy-Dispersive X-Ray Spectroscopy
FIB	Focussed Ion Beam
FCC	Face-Centred Cubic
FEM	Finite-Elements Method
MnS / α -MnS	Manganese Sulphide
OPS	Oxidic Polishing Suspension
px	Pixel
RD	Rolling Direction
RSS-bending	Radial-Stress-Superposed Bending
SE	Secondary-Electron Detection Imaging
SEM	Scanning Electron Microscope
SN	Sheet Normal
SRS	Strain-Rate Sensitivity
TD	Transverse Direction
UTS	Ultimate Tensile Strength

1. Motivation

The formation of microstructural damage during forming processes has, in recent years, become a major factor in designing damage tolerant processes and materials. Dual-phase steels as a technologically relevant type of advanced high-strength steels (AHSS) are often studied, as they exhibit a mechanically heterogeneous microstructure [1] and are therefore prone to the partitioning of stresses and strains during deformation [2], resulting in the formation of microstructural voids. The formation of damage in these steels is of high technological interest, as they are widely applied in the automotive sector, due to their high, linear strain-hardening behaviour, strength and ductility. For this class of steels, the fundamental mechanisms of void initiation due to plastic deformation have previously been identified [3] – however, the thorough investigation of their dominance and effect on global damage behaviour under various loading conditions still remains to be carried out in a way representative for the design of damage-tolerant forming processes.

The field of materials physics, being classically concerned with micro- or even nano-scale mechanisms, has always been challenged to link its findings up to the scale where they become relevant for technological application. Therefore, the engineering of materials is always an approach to bridge the scales between small-scale mechanisms, taking place in a multitude of places and ways simultaneously when regarded on the scale that determines the properties of a technological workpiece in application. As an example for a successful methodical bridging between these two points of view, the research on recrystallisation and grain growth processes can be mentioned. Being highly relevant to the application in the field of engineering due to its large and quantifiable impact on bulk mechanical properties [4, 5], the processes contributing to this empirical relation take place on a much smaller scale. Separately from this context, the underlying mechanisms of grain boundary migration can be researched upon on their native length scale [6]. Separating the viewpoints of bulk properties, and mechanisms leading to the atomic scale of grain boundaries, are not only length scales but also methodical developments that are capable of both depicting the microscopic processes and their overall impact on the global microstructure. Concerning recrystallisation, such methods are nowadays widely-used in the scientific community, enabling a statistical approach to the occurring processes by the use of X-Ray diffraction measuring the evolution textures [7] and measurement of multiple grain orientations via electron backscatter diffraction (EBSD) [8]. Statistics of a multitude of grains, orientations and grain boundaries are therefore the key to understanding the macroscale properties via the changes in microstructure. Such a link in experimental methodology between the research on fundamental damage mechanisms with microscale methods [9, 10], and the ultimate effect of the entirety of occurrences of these mechanisms on properties and part performance [11] is still largely missing. While findings have been correlated to bulk properties [12, 13], and in the field of simulation [14], a true scale-bridging experimental approach would have to deliver both detailed information on the scale of the emerging voids, and statistical data on a plethora of simultaneously emerging and evolving sites.

On the one hand, local observations at the microscale do not necessarily yield a complete and applicable picture of global damage formation in a deformed region, which in turn are necessary to assess the quantity and severity of damage. On the other hand, a pure quantification of damage over large areas or volumes as an integral quantity is not capable of revealing any insights on the ongoing mechanisms of void evolution, or data about the morphology of voids and their adjacent microstructure, preventing a thorough characterisation

and understanding of void formation mechanisms. This discrepancy clarifies the need for a method that bridges the gap in scales between microscale observations and macroscale sheet metal forming processes. A globally applicable tool for both the quantification and characterisation of individual damage sites, and large-scale, statistically relevant observations, has been developed in [15 - Publ. #1]. This approach, shown schematically in Figure 1, is able to quantify the dominance of certain mechanisms of void formation on a statistically sound scale, yielding detailed insights on both microscale damage mechanisms and damage assessment on the scale of formed parts.

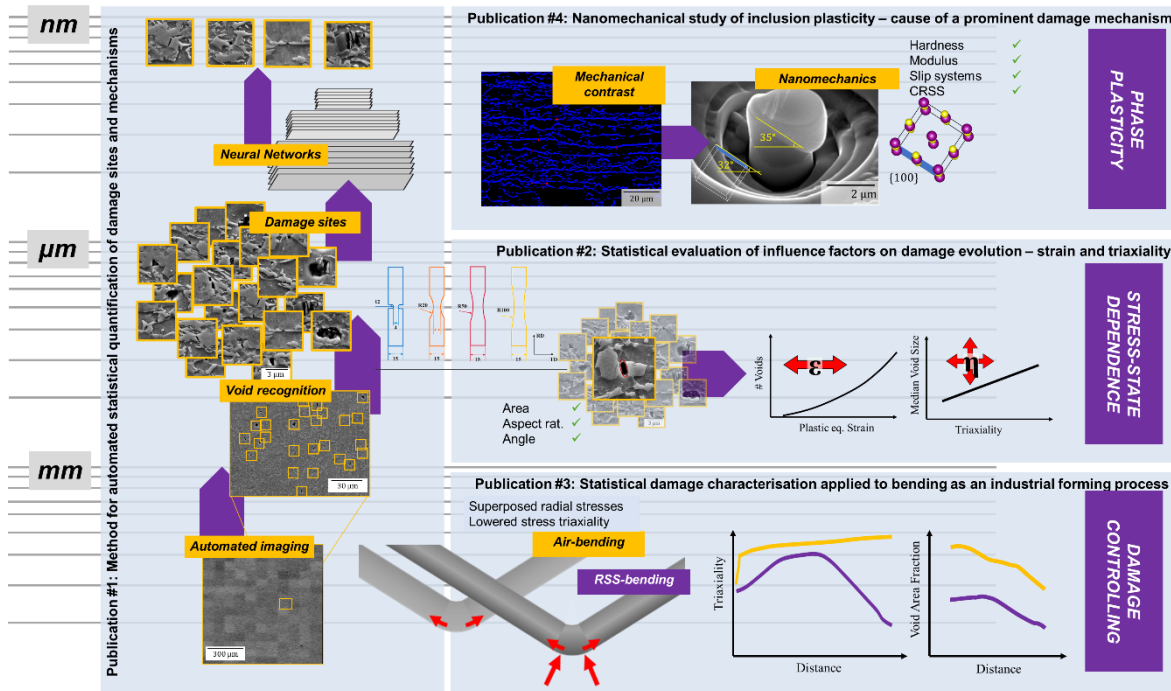


Figure 1: Structure of this dissertation, consisting of four peer-reviewed research publications

Being able to quantify not only the cumulative damage quantity with the applied method, but also gain statistical data on each individual void, however, enables a thorough and systematic statistical investigation of damage that was carried out in [16 - Publ. #2]. Regarding stress-state dependence, the question arises whether or not the classically assumed influences of stress and strain on the evolution of voids still are valid in a real microstructure. In a commercial dual-phase steel, the evolution of each void is largely governed not by a global continuum stress state, but by the local stress state, exerted through local microstructural constituents and their morphology. As proposed by several approaches to modelling damage, like by Rice & Tracey [17] or Gurson [18], the globally applied stress state has a major influence on the growth of voids, while the applied strain is the main influence factor on the nucleation of new damage sites. Prior to the failure of the material, shear bands are often claimed as a main influence on the coalescence of voids, leading to fracture [19]. However, these correlations have largely been proven for isotropic model materials [20], due to being unable to perform observations on a quantity of voids large enough to overcome the above-mentioned influence of the local microstructure and achieve a sound statistic on void sizes.

Applying the framework of automated imaging, detection and characterisation of voids in [15 - Publ. #1] to systematically chosen samples that differ in their global stress state, the proposed effect of triaxiality and strain on void evolution was demonstrated to be still valid when regarding not an isotropic model material, but the process of damage formation in a morphologically complex microstructure of a commercial dual-phase steel.

Due to the large-scale capabilities of the introduced method from [15 - Publ. #1], the result of altering the stress state during a real forming process, in order to suppress damage formation, can now be investigated by quantifying the damage incidents observed microscopically, but on a scale relevant for a technological workpiece [21 - Publ. #3]. This transfer to a technological process showcases the power of the introduced method to a relevant application, being capable of assessing damage on the scale of a formed part, with nothing but measurements taken on the microscopic scale of a single void. Exemplarily, this has been shown by regarding geometrically identical bending samples, that have been processed on different strain paths in [22], utilising the framework presented in [15 - Publ. #1]. The results obtained here clearly show that specifically engineering a forming process is capable of controlling the quantity of damage introduced to a workpiece in the application of sheet metal bending.

Complementary to the introduction and application of this novel, automated approach to characterising and quantifying microstructural damage, it is equally important to characterise the plasticity of the different phases of the mechanically heterogeneous microstructure, as a (simulative) prediction of damage is only feasible and reliable if the plasticity of all microstructure constituents is represented in a realistic way. For dual-phase steels, the plasticity of body-centred cubic (bcc) ferrite [23], as well as the structurally much more complex martensite [24], has been characterized previously using nanoscale experiments. Due to the mechanical contrast of these two phases, damage formation in dual phase steels is dominated by mechanisms intrinsic to the steel microstructure. However, many other steels used for bulk metal forming processes show a damage formation behaviour dominated by the initiation of voids at foreign phases like non-metallic inclusions. The main aspects of plastic behaviour at room-temperature, including hardness and active crystallographic slip systems and their critical resolved shear stresses (CRSS) are quantities valuable for the simulation of microstructural behaviour during forming of such steels. Out of this motivation, these were determined using the nanomechanical methods of nanoindentation and micropillar compression.

In summary, this work is motivated by the importance of explicit quantification for understanding the mechanisms and processes of damage formation on all scales from crystal plasticity to large-scale damage quantification relevant for a forming process. As the formation of damage begins with the plasticity of phases, nanomechanical methods deliver valuable, quantitative insights on the deformation behaviour on the nanoscale. The resulting mechanisms of void formation are observed and characterized on the microscale, using modern electron microscopy methods and taken to a level of statistical significance, generated by thousands of voids, with the aid of novel approaches in evaluating large-scale but high-resolution micrographs using deep-learning neural networks as a powerful tool for data evaluation. Ultimately, microscale observations of singular damage incidents are therefore taken to the level that makes it possible to systematically quantify the reached endeavours in controlling damage in forming processes, on the required scale of a formed workpiece. This approach spanning over the scales from nanoscale mechanisms of plasticity and damage initiation to the scale of a tensile sample or a forming process, is presented schematically in Figure 1.

2. Background on damage and deep learning

2.1 Definition of damage

The concept of damage, occurring during the deformation of metals, has for many years been addressed in various fields of materials engineering. Primarily, the research interest originates from the goal of a qualitative and quantitative understanding of damage introduced to a deformed microstructure, in order to both calculate necessary safety factors of parts and reliably assessing their expected service lifetime. To achieve this goal, damage has been described in a conceptual way that enables mathematical and simulative approaches [17, 18, 25], and researched upon experimentally to gain physical knowledge about damage mechanisms, and their relations with the applied deformation and individual material [26, 27]. As the research and conceptualisation of damage is carried out interdisciplinary over many fields, stretching from mechanics and mathematical modelling to materials science and the application in forming technology, it is equally challenging to find a common definition for the fundamental term “damage”, as to different applications and viewpoints, damaging behaviour to a part, material or microstructure is not necessarily a congruent concept.

As damage therefore has to be described and discussed in these various fields which are concerned with its formation, simulation, and impact on a final product, different approaches and definitions are utilized. From a technological point of view, the relevance of damage begins with the degradation of mechanical properties, which have an effect on the final, formed product – both in terms of mechanical strength [28] and fatigue behaviour [11]. As a materials scientist however, the focus in investigating the formation of damage lies in understanding the mechanisms that lead to the initiation of damage. As the causes for the formation of damage typically are to be found in the mechanical heterogeneity in the microstructure of a material [29], the partitioning of strains is responsible for the formation of voids [27] – this process is typically considered damage [30]. With modern methods like in-situ digital image correlation (DIC), this partitioning can be researched upon with respect to its impact on the formation of damage [9, 31]. Damage is therefore described as the formation of voids, or in a more general way, new surfaces [32].

“Ductile damage causes the degradation of physical properties, in particular of mechanical properties, due to microstructural defects. These defects are characterized by the formation of new surfaces. In structural materials voids and micro cracks initiate mostly by decohesion at interfaces such as grain boundaries and inclusions or due to brittle fracture of hard phases. The evolution of voids and micro cracks then causes damage under thermo-mechanical loading.” [32]

As the definition given by Hirt et al. in [32] additionally refers to specific mechanisms of void initiation, it becomes clear that the manifestations of these mechanisms leading to voids during deformation largely differ between regarded materials. While the formation of voids does occur with a variety of mechanisms, from brittle fracture observed at hard phases [33], semi-brittle mechanisms like the initiation of cracks in martensite [24, 34] to ductile decohesion processes of interfaces [10], the underlying cause is to be found in the contrast in mechanical behaviour between microstructure constituents. Before the onset of such processes of void initiation, which is regarded here as the onset of damage formation, the localisation in mechanisms of plasticity can be observed as in the movement and agglomeration of dislocations [35]. In contrary to the process of dislocation agglomeration in grains and at interfaces however, the

processes of decohesion and fracture that it might cause in a heterogeneous microstructure, are non-reversible. This approach has been considered in works in the fields of simulations and mathematical modelling [36] as well as applied in studies that set out to quantify the impact of damage on mechanical properties in order to separate the effects of (reversible) mechanisms like strain hardening and damage processes [28]. With these considerations about damage, it seems feasible to approach a definition of deformation-induced damage with three main characteristics: The degradation of mechanical properties, the formation of voids due to mechanical contrast between microstructure constituents, and the irreversibility of these processes. Therefore, a definition of deformation-induced damage is proposed:

Damage is the result of irreversible microstructural mechanisms, leading to a degradation of mechanical properties and performance of a material, typically through the formation of new internal surfaces due to intrinsic mechanical heterogeneity of a material.

2.2 Damage mechanisms in dual-phase steels

Consisting of hard martensitic and softer ferritic constituents, dual-phase steels show a pronounced microstructural heterogeneity intrinsic to their steel matrix. Processes of void nucleation occur due to partitioning of stresses and strains between these constituents [37, 38]. The classically identified causes of microstructural voids – deformation-induced or not – are the decohesion of martensite-ferrite interfaces, the cracking of martensitic regions and, more rarely observed, damage to ferrite-ferrite grain boundaries, as well as voids at non-metallic inclusions [39] (Figure 2).

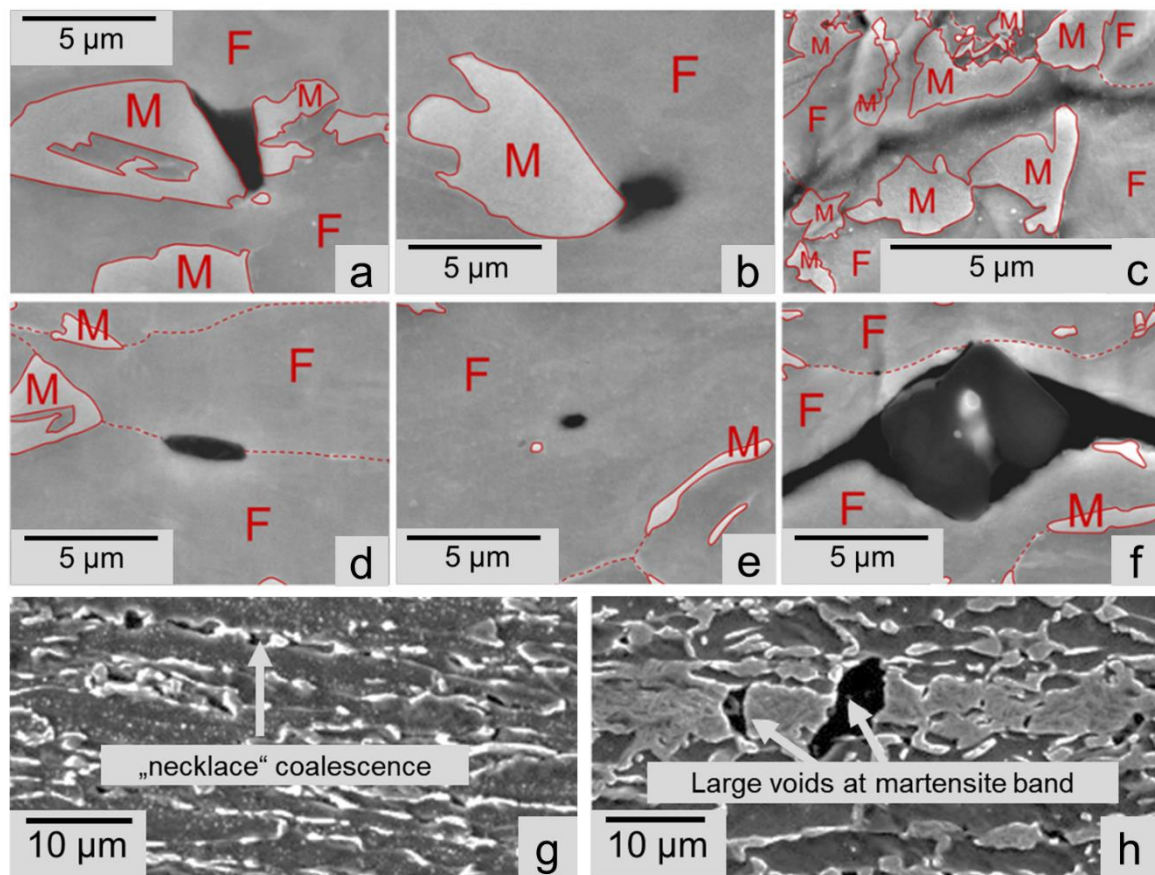


Figure 2: Observed fundamental mechanisms of void formation in dual-phase steels (a-f), reproduced from [3] and patterns due to microstructural morphology, reproduced from [40]. (a) Martensite cracking, (b,c) Martensite-Ferrite interface decohesion (c from in-situ experiment), (d) damage to ferrite grain boundary, (e) void in grain interior, (f) void around inclusion. (g) “necklace”-type void pattern along narrow band of martensite, (h) large martensite cracks in a wide martensite band.

While these causes for voids are largely undisputed in their existence [3, 41, 42], the identification of a dominant mechanism, with respect to the used microstructure and deformation path, is still subject of discussion. While martensite cracking is proposed as the main cause for deformation-induced damage by Mazinani et al. [43], Avramovic-Cingara et al. identify the decohesion of ferrite-martensite interfaces as the dominant mechanism [42].

However, differences due to the microstructural morphology of the investigated dual-phase steel grades are observed, a dependence also found by Hoefnagels et al. [3]. The reason for these differences is attributed to the wide variety of dual-phase steel microstructures. As the most widely-used nomenclature for dual phase steels, “DP600 / 800 / 1000” only specifies the ultimate tensile strength and the microstructure consisting of a ferritic / martensitic dual-phase structure, a plethora of parameters determining the microstructure and therefore the damage behaviour remain unspecified: thermomechanical Processing from austenite using various routes and annealing parameters [30, 44], martensite volume fraction [45], distribution and morphology [3, 42, 46, 47], mechanical contrast between the two phases [23], or ferrite grain size [30]. Such differences and the variation in the resulting shapes and patterns of voids are shown in Figure 3.

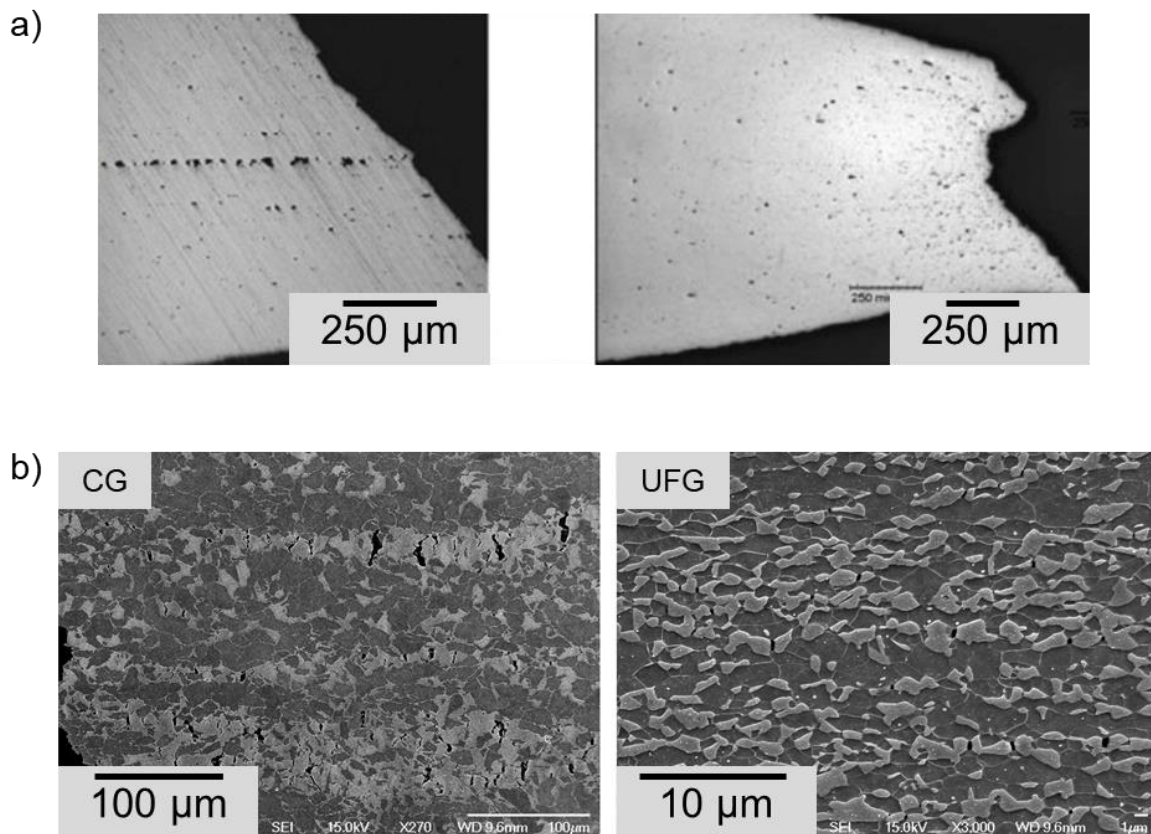


Figure 3: Effects of microstructural morphology on damage formation behaviour. (a) void patterns in two DP600 grades, the first image shows large voids in a martensite band in the middle of the sheet, while the other shows more homogeneous distribution of voids, reproduced from [42], (b) two dual-phase steels different ferrite grain sizes, coarse-grained (CG) and ultra-fine-grained (UFG), showing a tendency for large martensite cracks (CG) compared to nucleation and growth of smaller voids in and adjacent to martensite islands (UFG), reproduced from [30]

An agreement exists upon the fact that porosities due to inclusions are typically found in DP steels, however not considered deformation-induced, as in other materials [48], as in these dual-phase steels, the strain partitioning due to the martensite and ferrite constituents is causing the major part of void initiation. From the results reported in [15 - Publ. #1], it was proven that the quantity of observed voids at inclusions is not affected by strain, therefore not

being of related to deformation. This consideration is, however, proprietary to materials that show a high mechanical contrast due to their intrinsic structure of constituting phases, like dual-phase steels or intermetallic-reinforced alloys [33]. Especially in case-hardened steels, void nucleation and growth at non-metallic inclusions is the primarily observed damage mechanism [13]. While the identification of the relevant damage mechanisms in dual-phase steel grades can be considered complete [3, 39, 49], detailed characterisation and understanding of these fundamental mechanisms is still topic of ongoing research [24, 50] and method development. While modern scanning electron microscopes (SEM) are able to deliver high-resolution images of damage sites, classically applied SEM observations of microstructural damage suffer from two intrinsic shortfalls: Firstly, high-resolution characterisation always trades off resolution for the size of the field of view, meaning a simultaneously thorough characterisation of a large number of damage sites is classically compromised [2], while delivering deep insights on spatially defined proportions of the microstructure. Secondly, post-mortem observations of damage always lack not only the third spatial dimension, but also the temporal information of the damage mechanism, which both can be addressed by the application of modern in-situ deformation equipment and 3D-slicing technologies [3]. Due to the lack of temporal information without the application of in-situ methods, an equally challenging point is the exact attribution of a singular damage site to an individual damage mechanism. The fundamentally described mechanisms in dual-phase steels (Figure 2) develop in a highly complex microstructure, that makes the evolution of every single observed site dominated by local microstructure morphology. Furthermore, a simultaneous procedure or lapse of various of these mechanisms has been observed [39], and damage patterns been named in more phenomenological manners like “necklace-type coalescence” [40]. This lays an additional challenge on the objective of automating damage recognition and characterisation, in order to receive exact representations of the occurrence and dominance of damage mechanisms, as an observed damage site is not necessarily, in a post-mortem observation, clearly attributable to a single fundamental mechanism of damage initiation.

Also in-situ-experiments, while being able to unravel the cause of a damage site by comparing before- and after states, do suffer from limitations regarding their efficiency and also, accuracy that have to be critically discussed when performing such experiments. The major advantages of in-situ observations of damage initiation is clearly the ability to compare to an undamaged state [22]. Additionally, these types of experiments enable researchers to investigate local deformation around special points of interest, like emerging damage sites, using digital image correlation techniques [3, 37]. The obtained results can, furthermore, be applied in combination with microstructural and crystal plasticity models, to gain insights on the 3-dimensional behaviour of heterogeneous microstructures like dual-phase steels, leading to possible predictions of microstructural sites prone to damage formation [51-53]. However, due to their focus on individual damage sites and high resolutions, these experiments remain especially site-specific, which is an intrinsic shortfall due to the small number of experiments that can be performed with this methodically challenging and time-consuming experiments. To gain statistically relevant knowledge, while maintaining the temporal information of in-situ experiments remains the main challenge to not only investigate damage in specific microstructural places which are strictly dominated by their local stress state, but also find more global patterns of damage initiation, that can be used for damage-tolerant microstructural design parameters [14]. A second, intrinsic challenge of SEM-based in-situ experiments is found in the altered stress state at the observed sample surface compared to bulk, post-mortem observations [2, 9, 46]. In dual-phase steels, where the microstructural constituents are typically made distinguishable in the SEM by topological etching, the notch effect created

through the surface topography introduces an additional influence on the visible damage formation [54]. As these differences to bulk processes cannot be eradicated, all in-situ observations need to be carefully compared to bulk observations and, ideally, compared to simulation approaches incorporating and comparing between free surfaces and bulk deformation processes. Additionally, comparisons between SEM-based in-situ deformation experiments of microstructures [34], and nanoscale tensile samples that do not include large, 3-dimensional proportions of dual-phase microstructure [24] suggest, that in dual-phase steels, the depiction of the ongoing damage mechanisms made by in-situ observations still yields a close representation of the bulk mechanisms. Tomography-based in-situ experiments are a widely applied way of gaining temporal information about damage formation, without the effect of the free surface [55, 56], while in dual-phase steels, losing all microstructural information about phase distribution, thus making the identification of mechanisms impossible [57]. However, 3-dimensional resolution of voids and phases around damage sites is believed to be a powerful tool for unravelling the origin of sites of unclear origin like voids in the interior of a grain, as shown in Figure 2e), or the aforementioned “evolved” damage sites”.

In addition to the direct investigation, characterisation and quantification of microstructural damage events, the mechanisms of damage formation can be characterized by modern micro- and nanomechanical methods. This approach is totally complimentary to the aforementioned characterisation of damage events, since it enables an isolated view on the mechanisms contributing to the formation of these damage sites. To achieve such an isolation of a microstructural mechanism, it is important to establish the main contributing mechanisms leading to the formation of damage, and how to set up an experiment that is capable of observing these in a controlled environment. The process of - a what is classically called - a damage mechanism typically consists of several fundamental mechanisms on the nanoscale. Hence, a variety of nanoscale experiments comes into play when characterising such processes of damage formation. The most fundamental approach to the actual mechanism forming voids by fracture of microstructure constituents is a nanoscale experiment that replicates this process. Here, a widely-used method are micro-cantilever tests, that are capable of replicating fracture on the length-scale of microstructural damage in a controlled setup [58]. The quantitative result of these tests is typically the fracture toughness of a microstructure constituent. Micro-cantilever tests have the advantage of being able to quantify the initiation of fracture to a single phase, or even single-crystalline area, while altering the stress state from a bulk experiment. This does enable a singular quantification of the mechanism, while having to consider additional effects as size effects [59], dislocation pile-ups and Bauschinger effects [60, 61]. A critical quality of the experiment is the exact geometry of the, typically FIB-milled beam and its notch, the latter having a major impact on the crack propagation and therefore the quantitative outcome of the investigation [62, 63]. Performing such experiments therefore requires both a careful consideration of the chosen geometry and an exact manufacturing of the specimens. To determine the property of fracture toughness, other microscale experiments have been developed, in the form of double-sided cantilevers [64], which ensure a stable crack growth but require an even more complex sample preparation and indenter alignment. As these cantilever-based methods are typically used for brittle phases, the fracture toughness of interphases can be tested by vertical double cantilever bending [65].

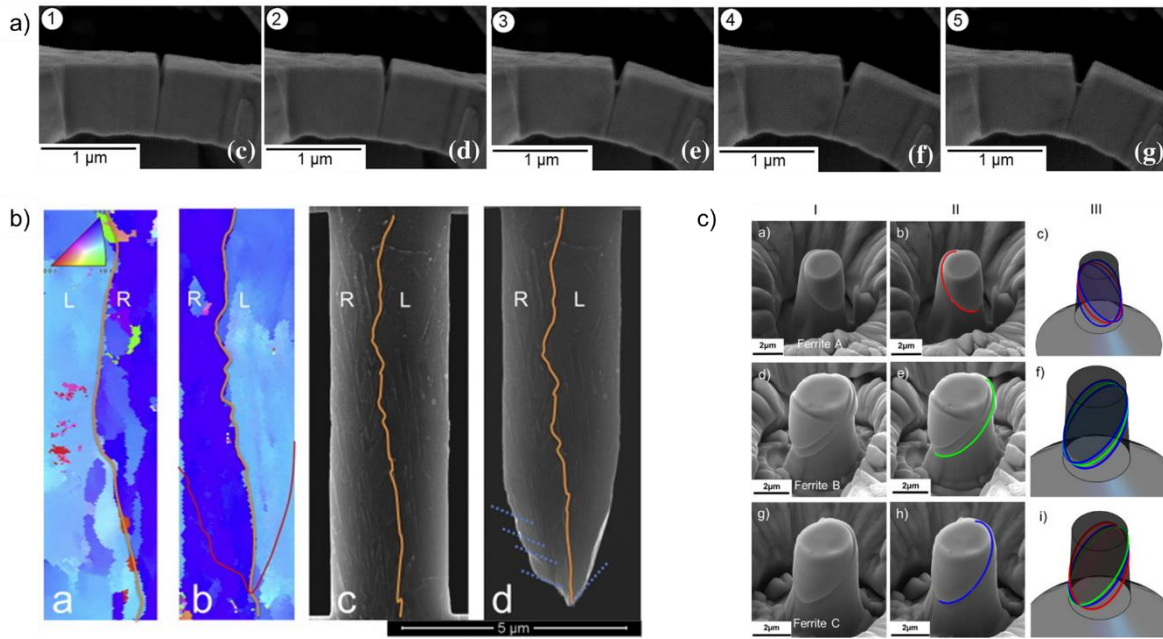


Figure 4: Examples of nanomechanical testing for quantifying mechanical properties for damage initiation. a) Microcantilever-bending, determining the quantity of fracture toughness, reproduced from [66], b) micro-tensile testing of lath martensite, coupled to EBSD investigations, reproduced from [67], c) Micropillar-compression to determine active slip systems and their CRSS in ferrite, reproduced from [23]

While the fracture toughness of microstructural constituents is a highly valuable quantity, especially for the modelling of damage formation, damage initiation is governed by the deformation behaviour on a microstructural level. Therefore, microscale experiments determining the plastic behaviour of the constituting phases are a key element of understanding, and ultimately, modelling the material behaviour leading to the initiation of damage sites. Such approaches have been carried out on the constituting phases of dual phase steels, ferrite and martensite, by both micropillar compression [23] and micro-tensile testing [24]. While distinct gradients in hardness can be resolved by using nanoindentation [68], the thorough investigation of the plastic behaviour and crystal plasticity through the application of micropillar compression yields complete, quantitative picture of the plasticity of the constituting phases [69, 70], while when utilising nano-scale methods, size-effects remain to be discussed [71, 72]. To determine the plastic properties of phases, micropillar compression tests can determine activated slip systems and quantify their critical resolved shear stresses (CRSS) [73].

2.3 Deep learning in materials science

Considering all these methods applied to investigate patterns and mechanisms of deformation-induced damage in such microstructures, it becomes clear that a thoroughly modern and high-throughput approach is vital when aiming to achieve both statistically relevant quantification and small-scale, physical information. Processing large amounts of data while simultaneously automating the characterisation of features is an aim that has, in recent years, been achieved using artificial intelligence in the form of neural networks, and has gained more and more applications in the field of materials science [74-76]. However, the application of deep learning algorithms in the field of materials science can go beyond the extraction and classification of microstructural features. In principle, deep learning methods have been applied in materials science in two significantly diverging ways: Firstly, for efficient characterisation of features, as mentioned above, greatly boosting the achievable throughput of data, and therefore, the statistical dependability of the obtained, quantitative results [75-79]. Similar approaches have also been made applicable by the integration in commercial or open-source software [80]. The second, widely-applied and discussed application for neural networks in the field is the “rational design” idea to utilize deep learning to predict material properties from input data like composition or molecular structure – or vice versa [81-83]. In materials science, this approach has been intensively carried out for the design of novel high-entropy alloys, as the prediction of properties from composition is a major goal in the development of such materials [81, 83, 84]. These approaches have been described by Butler et al. as three stages, the first predicting properties by using structure as input data, the second predicting both structure and properties by knowing composition only, and the third predicting all three of these using more abstract chemical and physical data, leading to a true “statistically driven design” of structures and materials [85]. A third application of deep learning methods to the design of materials can be found in the artificial design of microstructures from experimental data, such as parameters of microstructural morphology, creating artificial microstructures applied in computational approaches to simulate material behaviour. While such microstructures are classically created by means such as the Voronoi tessellation [86], deep-learning based approaches are able to render a more exact replication of the real material, by considering more parameters and their individual cross-correlations which are highly complex and not obtainable without using machine learning approaches as a tool for fitting [87, 88]. In the field of atomistic simulations of materials, neural networks are applied to reliably approximate potentials with a multitude of influence variables [89, 90].

3. Materials and methods

3.1 Materials used in this work

For the scientific publications part of this dissertation, two commercial dual-phase steels were used. The first, applied as “microstructure #1” in [15 - Publ. #1], was the same dual-phase steel sheet metal that was also used for the studies carried out in [21 - Publ. #3] as well as [16 - Publ. #2]. This material was supplied by ThyssenKrupp Steel Europe (Germany). For comparing the quantity of damage events between two different, commercial dual-phase steels that both fall into the DP800 norm, a second sheet metal was investigated in [15 - Publ. #1], which is also a commercial DP800 dual-phase steel, by ArcelorMittal SA (Luxembourg).

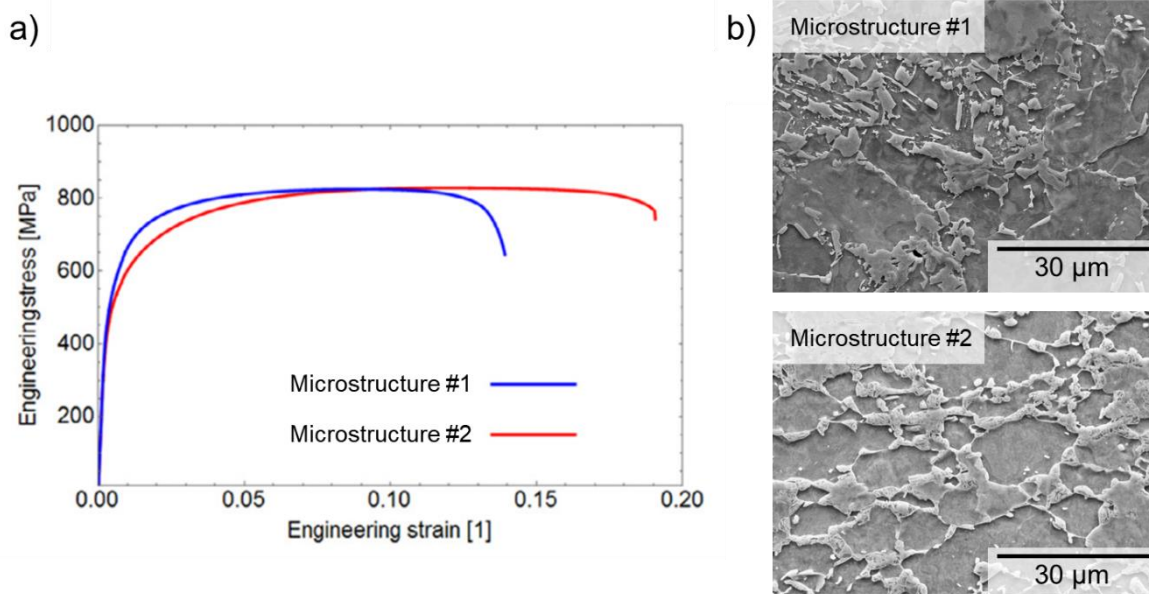


Figure 5: a) Stress-Strain curves of both dual-phase steels applied in this work, reproduced from [23]. b) SE-images of the two microstructures, with visibly “sharper” martensite morphology in Microstructure #1. Both images depict the RDxTD plane.

As visible from the data in Figure 5, both steels exhibit a martensitic-ferritic dual-phase microstructure, and an ultimate tensile strength (UTS) greater than 800 MPa. Differences are to be found, mechanically, in the ultimate elongation achievable (Figure 5a), and, concerning the microstructure, in the morphology of the martensitic constituents. While Microstructure #1 shows a more faceted morphology of the martensite islands, that are typically interconnected, Microstructure #2 contains more rounded, isolated islands. A strong banding of the martensite phase along the sheet thickness is visible in Microstructure #1, which is not the case in the second material used in this study.

All dual-phase steel samples used in the present research were cut from the initial material using electrical discharge machining (EDM). Metallographic sample preparation consisted of grinding (1200 to 4000 grit), mechanical polishing (6, 3 and 1 µm diamond suspension, on Struers DAC polishing cloths and OPS polishing on ATM Omega polishing discs), and

subsequent cleaning of the samples with a soap / water mixture. The samples were then etched in 1% nital (HNO_3 in ethanol) for 5 s to reveal the microstructure by topological etching.

For the study on MnS plasticity presented in [91 - Publ. #4], an X30MnAl17-1 steel grade in its as-cast state was used ensuring a plastic zone of the nanoindents completely inside the MnS inclusion. Due to the morphology of MnS inclusions in case-hardened steels like 16MnCrS5, which are typically forward extruded, this material was chosen instead. The material was kindly supplied by the steel institute (IEHK) at RWTH Aachen University. The inclusions found in this steel were verified by EDX measurements to be α -MnS inclusions.

3.2 Deep-learning-based characterisation of damage mechanisms

To achieve an efficient, small-scale but high-throughput classification and quantification of occurring damage sites in deformed samples, the process of detecting and characterising damage sites was automated. The method developed in a fundamental study [15 - Publ. #1] was applied on bending samples of varying stress states [21 - Publ. #3] to quantify deformation-induced damage sites in favour of all microstructural voids, which was enabled by the automated classification for the mechanisms of void formation. In [16 - Publ. #2], the same approach was used to quantify the occurrence, size and morphology of deformation-induced voids and correlate the findings to their dependence on the global stress state in the sample, exerted through a variation of tensile geometries.

The approach developed in [15 - Publ. #1] is a framework containing three steps of processing the SEM images (Figure 6), which are automatically acquired in a rectangular pattern by secondary electron imaging at 20 kV. Adjusting the SEM settings and therefore imaging conditions, is principally possible, but may require additional training of the subsequent neural networks or steps of augmentation of the training data as applied in [92]. As a first step, these panoramic SEM images are processed with a grayscale threshold separating black voids from the grey steel matrix (martensite and ferrite), which are then detected using a data clustering algorithm DBScan [93]. This way, not the grayscale threshold is utilised for measuring the voids, but for detecting the sites only, which is performed by the clustering algorithm. The coordinates (centroids) of the sites are then given over to an image processing, which crops the panoramic image around these sites, using windows of 250x250 px. Further processing is therefore not performed on the whole acquired SEM image, but on the individual images containing the detected damage sites in their centre.

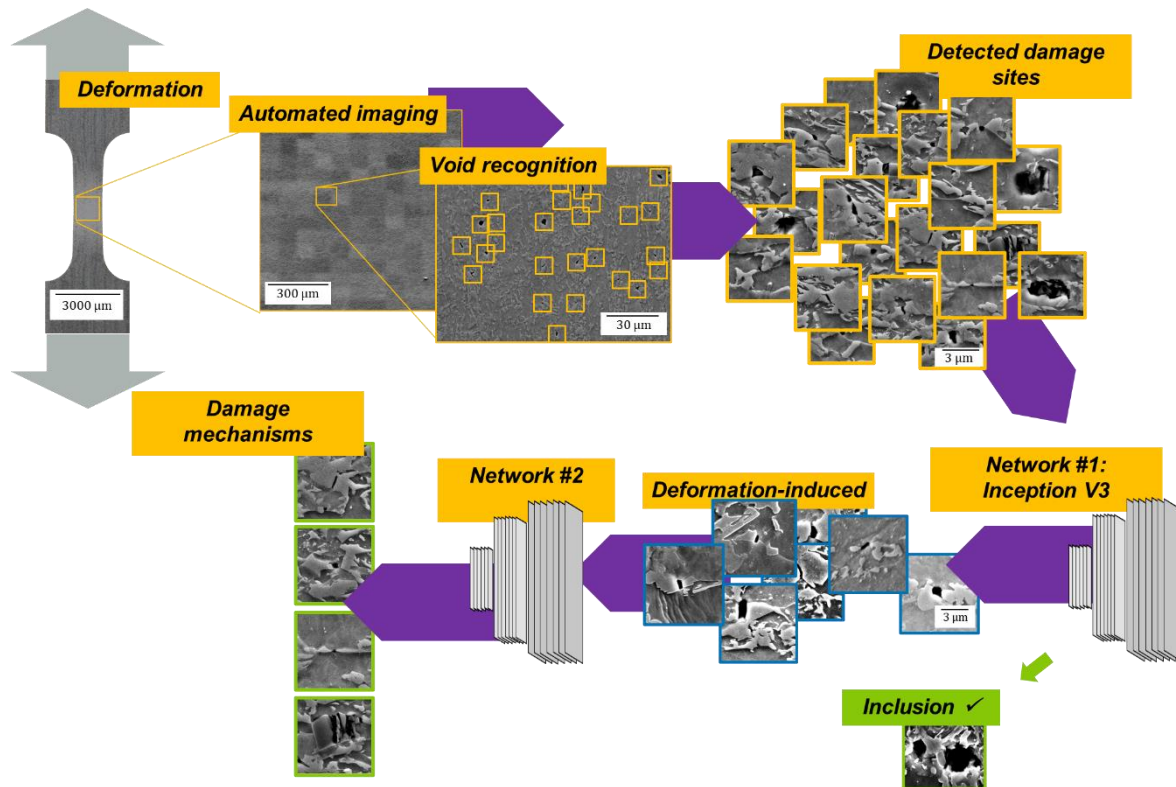


Figure 6: Structure of the framework with both neural networks [15 - Publ. #1]

After this first step of void detection / recognition, the cropped images are given over to the first neural network, which is trained to separate voids at inclusions or voids due to inclusions fallen out of the polished surface during metallographical preparation, from deformation-induced voids. For this purpose, the network InceptionV3 is used [94] and trained by the use of almost 5000 manually labelled voids, approximately 10% of which were inclusions [15 - Publ. #1]. The sites labelled as inclusions are then not processed any further by the framework. The sites that are recognised as deformation-induced damage need to be classified regarding their micromechanical mechanisms of origin, which is the purpose of a second, in-house conceived neural network that classifies the deformation-induced sites into further categories. As conceived originally in [15 - Publ. #1], the classes this network is trained to recognise are martensite cracks, interface decohesion sites, and a third category called “notch”. This category has been set up in order to contain those, typically very small damage sites, which are set in between two martensite islands, originally either at a very narrow segment of a martensite particle where a martensite crack has subsequently initiated, or between two sharp ends of originally separated particles. After void initiation at these sites, the original mechanism is not to be determined without a 3-dimensional view or a temporal information from an in-situ experiment [15 - Publ. #1]. As both mechanisms are initiated at these specific sites due to a local stress concentration (“Notch effect”), a separate category was introduced, as the main cause for damage here is not to be found in the mechanism, but in the local microstructure and the caused stress concentration by it. In further iterations of the setup, additional categories were introduced to improve the performance [92]: “Shadowing” is used to rule out any inadvertent detection of dark areas that are not caused by voids, but by the topology of the etched surface and the resulting shadows that are visible in SE images.

Also, the strategy of data augmentation was used to improve the classification accuracy in images from different imaging conditions, SEMs, and also a wider variety of stress states.

As the original network was trained on tensile samples, a variation of the stress state will alter the morphology of damage sites, like typically vertical martensite cracks that will change in orientation with a biaxial stress state [92]. The second network receives a cropped version of the original void images, of 100x100 px, as inclusions are typically much larger voids than deformation-induced voids. This way, the second network receives less data not related to the void in terms of surrounding microstructure. The final result of classification are labelled images of every detected damage, and a file containing a centroid and mechanism for all sites in the format .json. Both output types can be read by MATLAB scripts and undergo further processing in relation to the original panoramic image. For quantification of damage and statistics of void sizes and morphologies based on measurements of all individual voids contained on the acquired images, each individual void is measured using a watershed algorithm [21 - Publ. #3], also data about the shape of the void like aspect ratio and angle towards the horizontal axis are gathered for every individual detected void. A transfer of this approach to other material systems is equally possible, as the detection of voids is, in principle, possible in any SEM micrograph. Parts of the framework like the detection of voids have been applied to other material systems like Mg-Al-Ca alloys with an intermetallic skeleton [33].

3.3 In- and ex-situ deformation

For the investigations on deformation-induced damage carried out in this work on dual-phase steel, deformed samples of various origins, from tensile samples with varying geometries (in- and ex-situ deformed) to parts originating from forming processes, were investigated. Here, a separation has to be drawn between ex- and in-situ deformation. While all bending samples in [21 - Publ. #3] as well as all tensile samples in [16 - Publ. #2] have been metallographically prepared after deformation, and beforehand cut by the use of EDM machining so that the investigated specimens were cut out of the middle of the bending / tensile samples, the miniaturised tensile samples utilised in [15 - Publ. #1] were deformed partly ex- and partly in-situ. The ex-situ deformed samples were metallographically prepared as a complete specimen, thus not ground down or machined to their mid plane. However, due to metallographical preparation after the deformation, it is ensured, that enough material is removed by grinding and mechanical polishing that the state of deformation and damage formation is not to be considered at the surface of the sample, but in the bulk material. The in-situ samples from [15 - Publ. #1], however, mark a different methodical approach and, due to the investigations on a polished surface, possible alterations in stress state, and therefore damage behaviour, which is introduced due to the free surface on which the SEM investigations are carried out. This alteration is to be considered when performing this type of in-situ deformation experiments, especially when focusing on highly stress-state sensitive processes like damage void initiation and growth. As observed in [15 - Publ. #1], due to the hard and brittle nature of martensite, at least the mechanism of martensite cracking shows a strong resemblance to the observations on ex-situ bulk samples, so that conclusions drawn from in-situ investigations can securely be drawn concerning this mechanism. As ferrite shows significantly more plasticity than martensite when deformed as a dual-phase composite, artefacts of in-situ experiments are to be expected in this phase, as shown in Figure 7 as well as in Figure 2c).

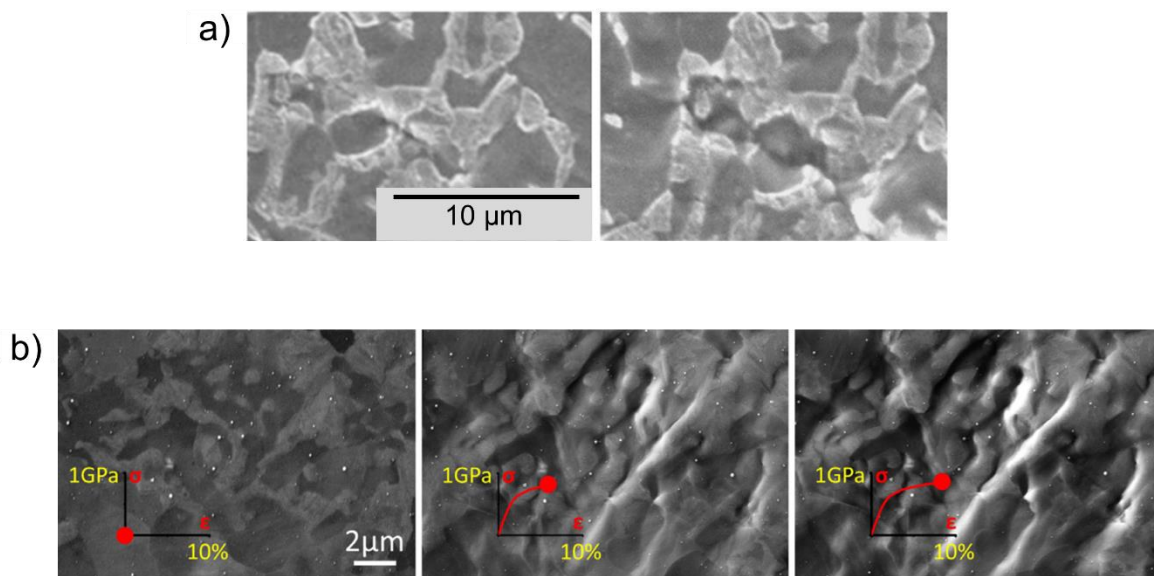


Figure 7: Examples of the formation of surface artefacts created in in-situ experiments, following the phase boundaries to martensite, in ferrite regions. (a) reproduced from [2], (b) reproduced from [27].

Here, we see severe plasticity in the ferritic phase, not only altering the stress state at the surface, but also subsequently altering the initiation process of voids by the decohesion of martensite/ferrite interfaces. In this work, we therefore focus on observations on martensite cracking from in-situ experiments and limit the deformation undergone in-situ to few percent of global plastic strain. This is achievable by pre-deforming the samples ex-situ to strains of around 11-14%, depending on the sample geometry and used grade of dual-phase steel, just before a significant amount of damage sites start to initiate. In this way, a much smaller amount of few % of global strain of in-situ deformation is necessary to visualise the initiation process of damage sites in the in-situ experiment, so that the formation of artefacts is largely suppressed. The inevitable formation of slip traces at the surface in such experiments is not regarded as unfavourable for the assessment of damage, in contrary to the formation of large surface artefacts as shown in Figure 2.

3.3 Nanoscale characterisation of damage mechanisms

To determine the plastic properties of a common inclusion phase in various case-hardened steels, α -Manganese sulphide, nanoindentation and micropillar compression were applied. These nanomechanical testing methods form a complimentary approach, being able to supply data on hardness of the inclusions as well as strain-rate sensitivity from standard nanoindentation using the Oliver & Pharr method [95] and strain-rate-jump testing [96]. To gain information on the crystal plasticity of MnS, which crystallises in a face-centred cubic structure with a two-atom basis, essentially forming a simple cubic ionic crystal, micropillar compression was carried out, yielding the active crystallographic slip systems and their critical resolved shear stresses (CRSS). The micropillars were milled using a focussed ion beam (FIB) on an FEI Helios 600i. Micropillar dimensions were 2 μm in diameter and 4 μm in height, with minimal tapering. The micropillars were compressed in an indenter by Nanomechanics .Inc., USA. The crystal orientations of all inclusions used for micropillar milling were determined by EBSD, equally in an FEI Helios 600i, using an EDAX EBSD detector. From the deformed micropillars, slip planes were identified by measuring the angle of the slip plane with a tilt correction according to equation 1 and confirmed for exemplary micropillars using lift-out EBSD.

$$\gamma_{90} = \arctan(\tan(\gamma_{45}) \cdot \sqrt{2}) \quad (1)$$

As the micropillars showed a continuous yielding, the yield stress was determined via an $R_{p0.2}$ criterion, taking the stress at 0.2% plastic deformation as the yield stress to determine the critical resolved shear stress (CRSS). After deformation, central slices were cut out from the micropillars using FIB, to perform further EBSD measurements of the whole vertical cross-section of the deformed pillars, confirming the observed slip planes and measuring the change in crystal orientation due to the activation of these slip systems [97].

4. Research publications

The main part of this dissertation consists of four peer-reviewed research publications in international journals.

After having exemplarily shown this method for the characterisation of phase plasticity to enhance the possibilities of simulating the onset of damage initiation, the further work carried out for this dissertation is concerned with the formation of microstructural damage in dual phase steels. To establish a scale-bridging approach that is able to investigate the damage events on the microscale with high resolution while simultaneously gaining the ability to view large areas of microstructure, automation via deep neural networks was introduced to the characterisation of voids. This approach was applied in the second research publication, ***“Large-area, high-resolution characterisation and classification of damage mechanisms in dual-phase steel using deep learning”*** [15 - Publ. #1] to the exemplary process of sheet metal bending. In this publication, an approach based on the automated detection and classification on large-scale, high-resolution SEM micrographs is presented and its benefits are shown by applying it to ex- and in-situ tensile testing of two dual-phase steel microstructures. In this way, a major gain in throughput and efficiency of the investigations on damage on the microscale is realised. By applying automation using the neural networks that have been set up in this work and trained to classify each of the thousands of voids emerging in a microstructure, the research on damage mechanisms that has previously mainly been carried out on a singular or a restricted number of damage sites [3], could be brought to a statistical level joining different length scales of microstructural investigations [2] and applications like forming processes [48].

The idea of not only obtaining statistics of individual voids but also examining the correlation to global stress and strain parameters has been undertaken in the fourth research publication, ***“On the effect of strain and triaxiality on void evolution in a heterogeneous microstructure – A statistical and single void study of damage in DP800”*** [16 - Publ. #2]. In this work, the large-area void characterisation is coupled to FEM simulations, in order to systematically investigate the dependence of void formation on the applied strain and stress state. To achieve this, differently notched tensile samples were deformed to fracture and subsequently analysed along the tensile axis in the middle of the sampled area with fields of view as large as 300 x 600 µm. This study allowed to validate concepts of void growth being governed by triaxiality as proposed by Rice and Tracey [17] and widely applied in the Gurson model [18]. The novelty in this work lies in the proof of such concepts for the complex microstructure of a commercial dual-phase steel. In such a highly heterogeneous microstructure, the local stress state effected on every single void makes it unfeasible to discuss the nucleation and growth of an individual void depending on the globally applied stress state. With the gained statistics of the magnitude of 10^3 - 10^4 voids in each sample however, this publication shows that the proposed dependencies are valid when regarding a statistically relevant amount of voids, which could not have been shown previously without a suitable method of automated and individual measurements of voids.

To show the possibilities of applying this approach to the engineering of damage controlled forming processes, in ***“Global and high-resolution damage quantification in dual-phase steel bending samples with varying stress states”*** [21 - Publ. #3], the framework presented in [15 - Publ. #1] has been applied to a technological forming process, proving the benefit of this automated characterisation method for the development and the validation of new forming processes able to reduce the magnitude of damage while maintaining the original final part

geometry. Here, the framework described and applied in [15 - Publ. #1] was applied for discriminating between voids caused by inclusions during metallographical preparation and deformation-induced damage, boosting the accuracy of damage measurements by the measurement of voids. The framework was therefore extended by the integration of the individual measurement of each void through the usage of a watershed algorithm. Ultimately, this publication shows a significant effect of the applied stress state during forming on the formation of damage during the forming process. While this tendency is expected and predicted by classically applied damage models [18], this work could prove its applicability on actual technological processes and its benefit to the development of novel, damage-controlled forming processes that maintain the part geometry while minimising the quantity of emerging damage. The thorough quantification of the deformation-induced damage was achieved by applying the developed framework.

Being the most fundamental approach to mechanisms of crystal plasticity leading to its understanding in the common inclusion phase of MnS and ultimately, benefits in the simulations of damage initiation, the first publication, ***“On the mechanical properties and deformation mechanisms of manganese sulphide inclusions”*** [91 - Publ. #4], is concerned with the mechanical properties of α -MnS. In this work, the plasticity of this phase is characterised using nanomechanical testing methods, namely nanoindentation and micropillar compression. The study yields quantitative data about the plasticity of MnS, ranging from hardness and Young's modulus to strain rate sensitivity from nanoindentation strain-rate-jump testing. Furthermore, the activated slip systems and their corresponding CRSS values were determined by micropillar compression experiments and subsequent EBSD measurements of lamellae from the micropillars. In this way, an approach to thoroughly characterise the crystal plasticity of an inclusion phase could be determined, which can in the future be utilised by CP-FEM simulations of a composite of MnS and a surrounding steel matrix, leading to a benefit in reliability of model predictions of damage initiation by realistically simulating the plasticity and strain partitioning in such a material. Damage initiation at inclusions, while being a dominant damage mechanism in many grades of steels used for bulk metal forming processes [98], does not occur dominantly in dual-phase steels. Therefore, the plasticity of inclusions with the aim to enabling accurate microstructural simulations has been chosen as an example for the characterisation of phase plasticity in a complementary way to the studies on damage in dual-phase steels carried out in the further publications part of this work.

5. Conclusions

- The characterisation of voids in a dual-phase steel microstructure, in terms of their mechanisms of initiation, can be reliably carried out by applying modern deep-learning approaches, with grayscale SEM images given as the only information. (Publ. #1)
- The dominance of micromechanical mechanisms of damage initiation and its dependence on outer factors like microstructure or applied stress state can reliably be assessed by introducing a statistical relevance of the gathered data on mechanisms. Such statistics are enabled by the introduction via a deep-learning approach. (Publ. #1, #2, #3)
- While damage mechanisms can be classified theoretically in the decohesion or the cracking of microstructural constituents, in a real case this separation is not necessarily possible post-mortem, as a microstructural void may have experienced several of these mechanisms during its formation. In-Situ tests are therefore a valuable, complimentary approach to post-mortem, statistical evaluations, which can equally be enhanced in their efficiency by automated detection and classification of sites. (Publ. #1)
- Technological processes like sheet metal bending can be tailored considering the formation of damage to minimise damage while maintaining the final product geometry. The introduced methods of automated void detection and individual quantification are capable of quantifying damage on the spatial scale relevant for the underlying macroscale forming process. (Publ. #3)
- Locally and globally, stress state is a major influence factor on damage formation. While in terms of the initiation and growth of an individual damage site, in-situ experiments showed a significant variety in forms of void evolution, a statistical viewpoint yields an agreement with simple models of void initiation and growth even in complex microstructures: Strain is the main driving force for the nucleation of voids, while stress triaxiality largely governs the growth of voids. (Publ. #1, #2)
- The ensemble of voids seen in large-scale micrographs of fractured tensile samples leads to the conclusion that the onset of material failure is not governed by a single, large damage site, but the initiation of such sites through void coalescence is effected largely by the local ensemble of voids. (Publ. #2)
- In order to control damage on the large scale of a technological process, statistical relevance is key to achieving a reliable assessment of magnitude, manifestation and morphology of damage. Characterising a large number of voids in a significantly large part of the microstructure is therefore required and has been achieved. (Publ. #3)
- The influence of the microstructure on damage formation is significant, as seen by the comparison of two different DP800-grade steels. Therefore, a careful characterisation of mechanical phase contrast and microstructural morphology is required to produce new, damage-tolerant microstructures in addition to damage-controlled forming processes. (Publ. #1)
- Microstructural heterogeneity, as the main cause of void formation through the partitioning of stresses and strains in a microstructure, can be investigated by nanoscale experiments like nanoindentation and micropillar compression, yielding quantitative insights on the individual phase plasticity. (Publ. #4)

6. Outlook

Having shown the advantages and limitations of applying neural networks for the automated characterisation and quantification of microstructural damage sites, the foundations made in this work can be built upon in the way of extending in several directions. Firstly, improvements in accuracy of the automated characterisation are possible to be made, especially in terms of classifying voids that are largely evolved from their state of nucleation, as discussed in [15 - Publ. #1]. As the classifying performance of a neural network will always be relying on its training data, further enhancements to the method can be made by making it more robust to influences like imaging conditions, altered stress states, or different dual-phase steel microstructures that exhibit altered morphologies. A powerful approach to achieve such an improved robustness is the application of data augmentation, where the time-consuming process of gathering new training data for every desired alteration of input data is avoided by simulating these conditions with the appliance filters or rotations to the existing dataset. Such approach has been carried out for the showcased framework in [92], being able to apply the framework to a heavily altered stress state. While all stress states applied in the studies part of this dissertation are dominated by tensile stresses, here, the altered morphology of voids due to a biaxial stress state is accounted for using not new training data, but augmenting the existing dataset.

Secondly, expanding the benefit yielded by applying the approach of automated imaging, detection and classification is possible by adapting the method to a wider variety of materials. In various stages, this can be done for different dual-phase steel grades as in [15 - Publ. #1], or completely different material systems that equally show an initiation of voids or cracks due to microstructural heterogeneity. Initially, this possibility has been proven in [33] for the example of Mg-Al-Ca alloys exhibiting a magnesium matrix reinforced by a hard and brittle intermetallic skeleton.

A third way of thinking forward these approaches would be further a boost in experimental efficiency by integrating such frameworks directly into the step of imaging. As on the large panoramic images taken, only a small amount of space is occupied by voids, a large proportion of the microstructure is imaged in high resolution, which is, depending on the purpose, not necessary for studies on these voids. Integrating the step of detection into the software of a microscope therefore could show a major benefit to processing times in the SEM, and therefore further enhance experimental efficiency. Equally, in-situ experiments can be carried out in a more efficient way, as a microscope could be capable of tracking a multitude of sites of interest automatically, without the need to acquire large-scale panoramic images in every single deformation step.

This dissertation therefore shows a leap forward into an automated way of gathering microscale insights on damage formation, joining the viewpoints of materials physics and engineering – future work can improve on this basis and make it possible to apply these new methods to thoroughly enable researchers to gain insights on this scale while maintaining the ability to efficiently characterise damage on a scale relevant to their regarded process.

Publication #1

Large-area, high-resolution characterisation and classification of damage mechanisms in dual-phase steel using deep learning

Carl F. Kusche, Tom Reclik, Martina Freund, Ulrich Kerzel, Sandra Korte-Kerzel

PloS one, 14(5), May 2019

<https://doi.org/10.1371/journal.pone.0216493>

For this publication, the candidate performed (in cooperation with Martina Freund as part of her bachelor's thesis that the candidate supervised) all experiments, evaluated and analysed the results. In cooperation with the co-authors, the candidate wrote the original manuscript as well as the final reviewed version.

RESEARCH ARTICLE

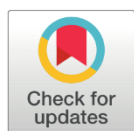
Large-area, high-resolution characterisation and classification of damage mechanisms in dual-phase steel using deep learning

Carl Kusche¹✉, Tom Reclik¹✉, Martina Freund¹, Talal Al-Samman¹, Ulrich Kerzel^{1,2}, Sandra Korte-Kerzel¹*

1 Institute of Physical Metallurgy and Metal Physics, RWTH Aachen University, Aachen, Germany, **2** IUBH University of Applied Sciences, Bad Honnef, Germany

✉ These authors contributed equally to this work.

* korte-kerzel@imm.rwth-aachen.de



OPEN ACCESS

Citation: Kusche C, Reclik T, Freund M, Al-Samman T, Kerzel U, Korte-Kerzel S (2019) Large-area, high-resolution characterisation and classification of damage mechanisms in dual-phase steel using deep learning. PLoS ONE 14(5): e0216493. <https://doi.org/10.1371/journal.pone.0216493>

Editor: Paweł Pławiak, Politechnika Krakowska im Tadeusza Kościuszki, POLAND

Received: January 14, 2019

Accepted: April 22, 2019

Published: May 8, 2019

Copyright: © 2019 Kusche et al. This is an open access article distributed under the terms of the [Creative Commons Attribution License](https://creativecommons.org/licenses/by/4.0/), which permits unrestricted use, distribution, and reproduction in any medium, provided the original author and source are credited.

Data Availability Statement: The data is available publicly at <https://git.rwth-aachen.de/Sandra.Korte.Kerzel/DeepDamage.git>.

Funding: This work was supported by: SKK and TA, TRR188 - project B02, Deutsche Forschungsgemeinschaft, www.dfg.de. The funders had no role in study design, data collection and analysis, decision to publish, or preparation of the manuscript.

Abstract

High performance materials, from natural bone over ancient damascene steel to modern superalloys, typically possess a complex structure at the microscale. Their properties exceed those of the individual components and their knowledge-based improvement therefore requires understanding beyond that of the components' individual behaviour. Electron microscopy has been instrumental in unravelling the most important mechanisms of co-deformation and in-situ deformation experiments have emerged as a popular and accessible technique. However, a challenge remains: to achieve high spatial resolution and statistical relevance in combination. Here, we overcome this limitation by using panoramic imaging and machine learning to study damage in a dual-phase steel. This high-throughput approach now gives us strain and microstructure dependent insights into the prevalent damage mechanisms and allows the separation of inclusions and deformation-induced damage across a large area of this heterogeneous material. Aiming for the first time at automated classification of the majority of damage sites rather than only the most distinct, the new method also encourages us to expand current research past interpretation of exemplary cases of distinct damage sites towards the less clear-cut reality.

Introduction

The damage encountered in forming of metallic components poses both a great challenge in manufacturing, as well as enormous potential for improved lightweight design. Current efforts to lighten load-bearing structures, e.g. car bodies, focus on an increased use of low density materials, such as aluminium and magnesium alloys, enhancement of the (cold) formability of high strength steels and minimisation of the material used in structural elements.

In the context of increasing formability and improving the (remaining) local strength after processing, the key challenge is to comprehend the microstructural damage induced during deformation in metal forming. This would allow engineers to minimise damage by adapting the forming processes and accurately assess the remaining material performance in service

Competing interests: The authors have declared that no competing interests exist.

after processing to save excess material. However, the physical mechanisms underlying damage in the most prominent high performance materials, such as dual-phase steels, are incompletely understood in spite of an ever-increasing research effort over the last decade [1].

The reason why the fundamental mechanisms of damage formation remain elusive lies in the complex microstructure of dual-phase steels. They are categorized and marketed based only on attained yield strength and the presence of a dual phase (ferrite and martensite) microstructure, but their properties are determined by a zoo of often interdependent parameters. These include volume fraction, morphology and carbon content of the hard martensite phase, mechanical contrast between the phases, homogeneity of texture, grain size and phase distribution as well as local and mesoscopic segregation of alloying elements [2–4].

As in any other multiphase material that combines two components with different mechanical properties, the mechanical contrast between the constituents can induce high local strains in the microstructure. These typically exceed the macroscopic strain because the soft phase (ferrite in a dual phase steel) has to compensate for the harder phase (martensite) to maintain strain compatibility [5]. Hence, any serious endeavour to understand the damage tolerance of these materials has to account for the complex interaction of the microstructural constituents and particularly their co-deformation behaviour. In a general sense, the principal stages of damage formation include the nucleation of microscopic voids in the microstructure, and their subsequent growth and coalescence with increasing strain until failure [6]. This process is conventionally studied post-mortem and largely manually, by analysis of samples obtained at different strains. Damage formation is, however, a dynamic phenomenon since the aforementioned stages occur and evolve depending on the microstructural environment, as well as the induced stress state. This is why in-situ techniques have become instrumental in unravelling dynamic processes as they allow researchers to observe the material deform directly and at the resolution of the chosen microscope [7–10]. In most cases, however, statistical relevance is sacrificed over spatial resolution by focussing only on a small area of the material to gain time- or strain-resolved information at high resolution. A further limitation is that data analysis of in-situ experiments is commonly done by hand so that larger datasets, including ones obtained post-mortem, remain difficult to analyse. To overcome these shortcomings of being limited by the field of view of a micrograph and the size of collected datasets at sufficient resolution, one has to adopt a much more powerful and efficient approach enabling ‘high-throughput’ ex- and in-situ analysis.

In the case of dual-phase steels, the pressure to achieve this, is clearly evident from the challenges still faced in unravelling damage. A vast number of studies exists from the macro- to the microscale, including a multitude of variations of the critical parameters, which have been identified [11–14]. However, so far it has proved difficult to reconcile all observations into comprehensive descriptions and models of damage in this important engineering material. We believe that the main reason lies in the heterogeneity of the microstructure, not only between samples, batches and alloys but also within each given volume of material [4, 15]. Where the high resolution studies of deformation mechanisms are intrinsically limited by their ability to study representative areas or volumes of the investigated material [5, 16, 17], the transfer and comparison of results between researchers become even more difficult. A new approach is therefore essential to propel our understanding of damage in complex advanced high strength steels. Such an approach will have to combine several essential aspects: (i) imaging of deformation-induced damage mechanisms at high resolution, (ii) efficient analysis to facilitate comprehensive comparisons of material state (e.g. strain level), (iii) integration of in-situ straining to observe damage evolution and (iv) quantitative analysis to the scale of a fully processed part (i.e. approaching mm² in sheet metal) to incorporate the inhomogeneous distribution of microstructural features [18] and variable stress/strain paths encountered during forming [1].

Here, we propose a promising new framework (Fig 1) to achieve just this, the analysis of large micrographs of the order of a mm^2 at high resolution, and therefore without the usual sacrifice of statistical relevance in the study of deformation-induced damage in highly heterogeneous microstructures. We employ panoramic imaging by scanning electron microscopy (SEM) at high resolution, both after deformation (ex-situ) and during straining (in-situ) inside the SEM. For this, we use a DP 800 dual phase steel as an example material that combines a high commercial popularity as a sheet metal in the automotive industry with great challenges in its characterisation and knowledge-driven improvement due to its intrinsic and scale-bridging heterogeneity from the micron to the millimetre scale. To enable automated detection and efficient

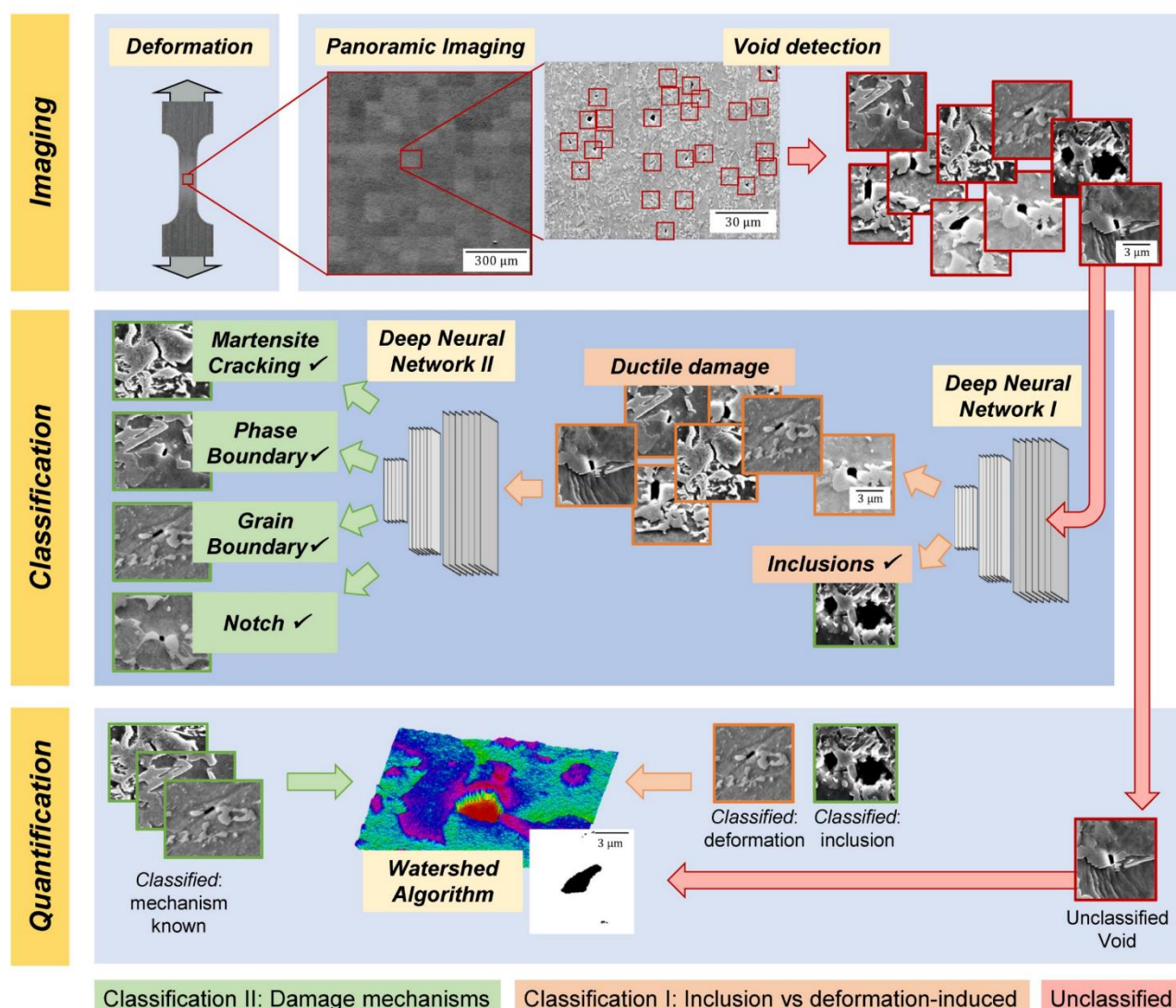


Fig 1. New approach for high resolution statistical damage classification by artificial intelligence. Based on panoramic imaging inside the SEM, the observed damage is identified, quantified and classified by artificial intelligence into four pre-selected categories (shown schematically).

<https://doi.org/10.1371/journal.pone.0216493.g001>

quantitative and qualitative analysis of damage within the images recorded before, after and also during deformation, we use trained convolutional neural networks, known to be particularly apt at image recognition and analysis [19]. For almost a decade, the “ImageNet Challenge” [20] has been focussing on the optimisation of algorithms and techniques for image recognition and object detection and identification. In recent years, powerful architectures based on deep convolutional networks have started to dominate the field. The success of deep convolutional networks in image analysis has already found numerous applications, from the identification of cancerous anomalies in medicine [21, 22] to the detection of cracks in concrete [23].

In the following, we first describe the employed computational and experimental methods in detail before reporting our findings from bulk and in-situ deformation experiments. The results section is divided into the three main research questions concerning this topic, namely, the distinction between inclusions and deformation-induced damage, the definition of appropriate classes for deformation-induced damage, and, subsequently, the observed dependency of damage mechanisms on tensile strain in the dual-phase steel. The results are discussed and compared within both the fields of artificial intelligence and materials science and engineering.

Methods

Machine learning and neural networks

Machine learning is a broad term which originally encompasses the “programming of a digital computer to behave in a way which, if done by humans or animals, would be described as involving the process of learning” [24]. In practice, this means using various algorithmic approaches to extract relationships from data and apply this knowledge to new samples. Popular machine learning algorithms include decision trees, support vector machines and in particular neural networks. On a fundamental level, neural networks mimic the basic working principle of a (human) brain (Fig 2): The basic building block is a neuron which receives multiple inputs, either from the “outside world” or other neurons, compute the weighted sum, which is then modified according to a transfer function before the output computed this way is passed to either the outside world or other neurons:

$$o_j = \sigma(\sum_i w_{ij}x_i) \quad (1)$$

where o_j is the output of a specific neuron, σ a transfer function and w_{ij} a weight matrix describing the strength of the connection between input variables x_i and the output.

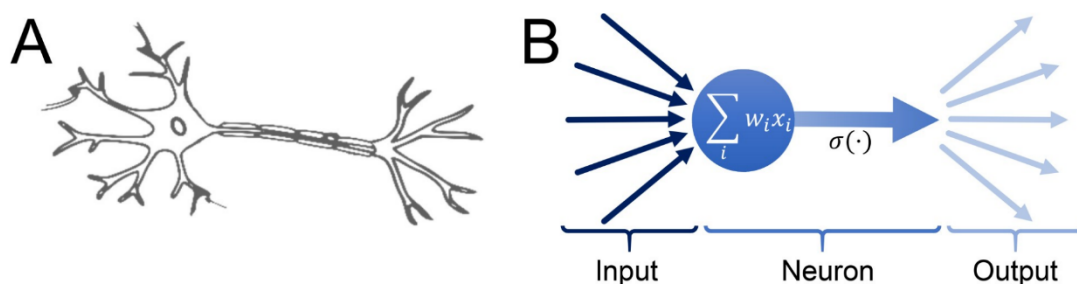


Fig 2. Models of biological and artificial neurons. (a) Simplified model of a biological neuron: The main body of the neuron receives input from many other neurons, transmits (or not) a signal which is then sent to many other neurons. Input is received from other neurons or the outside world in the input layer, the computed output is transmitted to other neurons or the outside world for the output layer. (Image in (a) published with a CC0 license at <https://pixabay.com/en/brain-neuron-nerve-cell-science-2022398/>).

<https://doi.org/10.1371/journal.pone.0216493.g002>

Using these neurons as building blocks, artificial neural networks are then built—in a simple picture—by combining many of these neurons as building blocks into layers. The first layer is called the “input layer” and receives the input from the outside world, in our case the micrograph images containing damage sites. The input is then passed through one or more intermediate or hidden layers to the output layer, which outputs the results to the outside world, in our case the researcher that receives the classification of the individual damage sites by the neural networks. As more and more powerful computer hardware has become available, neural networks can now consist of many such layers and are hence called “deep neural networks” (DNN). The exact shape of the weight-matrix allows to construct flexible and powerful DNN architectures which are ideally suited for different specialised tasks. In the case of images, so-called convolutional neural networks (CNN) have proven to be particularly apt in image recognition and analysis [19]. The name convolutional neural networks stems from the fact that the weights of the neurons are not free to take any value during network training but are constrained such that only few weights are available, which are shared across many neurons. These elements are arranged on diagonal bands in the weight matrix, e.g.

$$W = \begin{pmatrix} w_1 & \dots & 0 \\ w_2 & w_1 & \dots \\ 0 & w_2 & w_1 \end{pmatrix} \quad (2)$$

It can be shown mathematically that this is equivalent to the convolution of two distributions. Hence, CNNs can obtain the ability to act like filters in conventional image processing (e.g. edge detection, etc.). The main idea behind using CNNs is then that the various convolutional layers of the network can automatically learn the relevant features in the images associated with the content of the image, in our case a particular class of microstructural damage. The weight matrix of the final layer of the CNN network is fully populated and the individual weights are free to choose any value, i.e.

$$W = \begin{pmatrix} w_{11} & w_{12} & w_{13} \\ w_{21} & w_{22} & w_{23} \\ w_{31} & w_{32} & w_{33} \end{pmatrix} \quad (3)$$

This so-called “fully connected” layer is used to translate the output of the CNN analysis into a probability associated with the identified damage class via a softmax function. The fundamental setup of the neural networks used in this analysis is then: input layer, several convolutional layers, a fully connected layer followed by softmax function.

The neural networks are trained using supervised training. At each iteration of the training process, a set of images is presented to the network for which the “true” output (label of damage sites) is known. Using the current state of network weights, the network calculates an output based on each image. Using an appropriate cost function, the difference between the calculated output and the desired (true) output is transformed into a penalty. The network weights are then iteratively adjusted via back-propagation, such that the discrepancy between the computed and desired output is minimal. One of the principal difficulties in training neural networks in general, and for this study in particular is access to sufficient high quality training data. Since no prior labelled training data was available, a dataset of—in total 4944 labelled damage sites—was obtained in the following way (Table 1): Potential damage sites were identified in panoramic electron microscope images using the same clustering approach as used in the later stages of the network training and application. The resulting candidate images were analysed and labelled manually by experts (material scientists). It is important to note that any

Table 1. Labelled training data over 4944 damage sites.

Damage class	Occurrence (number of sites)
Inclusion	572
Grain boundary decohesion	166
Martensite cracking	1582
Notch	874
Phase boundary decohesion	1750

<https://doi.org/10.1371/journal.pone.0216493.t001>

bias the expert may have (e.g. showing a tendency to label images according to a given class or preferring one damage class to another) will translate into a bias of the final neural networks since the neural networks use these manually labelled images as ground truth. In order to remove such a potential bias, a blind study was performed among 19 experts including experienced researchers and students at undergraduate to post-graduate levels. Each expert was shown a set of 20 damage sites and the responses from the individual experts were cross-checked to ensure consistent assignment of labels to the damage classes. 80% of the dataset was used to train the neural networks, 20% was retained as an independent test sample to evaluate the performance.

The analysis setup is illustrated in Fig 1. As a first step, the grayscale high-resolution electron microscope panoramic image is analysed with respect to the grayscale values. As all damage sites considered in this analysis are characterised by a dark area in the micrograph, a suitable cut-off is chosen to identify the potential damage sites. Then a clustering algorithm (DBSCAN [25, 26], implemented in scikit-learn) is used to distinguish actual voids from artefacts like singular pixels below the cut-off value. The DBSCAN (Density-Based Spatial Clustering of Applications with Noise) algorithm takes a set of points as input, in our case the micrograph images. Fundamentally, algorithm group points that are close to each other (typically estimated by the Euclidean distance) are integrated into clusters. The algorithm is controlled by two parameters, the distance ϵ , which effectively describes how far the algorithm should consider points to be part of the current cluster, and the minimum number of points within a distance ϵ that are needed to form a cluster. Points, which are not associated to clusters are considered as noise. A sample image of 250-by-250 pixels is then taken at each potential damage site from the panoramic micrograph. These candidate pictures are presented to a first deep convolutional neural network, which aims to identify whether the damage site in question is due to an inclusion. If the probability calculated by the neural network exceeds a pre-defined threshold ($p_1 > 0.7$), this damage site is classified as inclusion, otherwise, the image is cropped to 100-by-100 pixels and presented to a second deep convolutional neural network which is specifically trained to classify a damage site into martensite cracking (MC), notch (N), grain boundary decohesion (B) or phase boundary decohesion (PB). Again, if the calculated probability exceeds a given threshold ($p_2 > 0.7$), the damage site is classified accordingly, otherwise the picture is flagged for later manual analysis. Finally, the original panoramic microscope image is amended such that all identified damage sites are highlighted and labelled.

It was decided to split the total classification into two separate networks, for the sake of its use in application. As for many purposes like measurements of void area fractions of deformation-induced damage, only a separation into inclusion voids and deformation-induced voids is required, a first step should include this distinction exclusively. Then, in a second step, only the voids classified as deformation-induced should be processed further into classifying individual damage mechanisms. For the first network, a standard network (InceptionV3 [27]) was found to give best results (cf. Table A in S1 Supporting Information), the architecture of the second CNN is given in Table 2, following Xu et al.[28]. In each case, ELU[29] was used as a

Table 2. Architecture of the second deep neural network (CNN). Descriptions of each layer type may be found in the S1 Supporting Information.

Layer type	# channels	Window Size	Stride
Convolution (input)	192	(5,5)	1
Convolution	160	(1,1)	1
Convolution	96	(1,1)	1
Max Pooling		(3,3)	2
Dropout (p = 0.5)			
Convolution	192	(5,5)	1
Convolution	192	(1,1)	1
Convolution	192	(1,1)	1
Max Pooling		(3,3)	2
Dropout (p = 0.5)			
Convolution	192	(3,3)	1
Convolution	192	(1,1)	1
Convolution	10	(1,1)	1
Average Pooling		(8,8)	1
Dense + Softmax			

<https://doi.org/10.1371/journal.pone.0216493.t002>

transfer function. The input image is passed to the first convolutional layer as an appropriately sized input tensor of size (50,50,1). The much more complex architecture of the InceptionV3 network is described in detail in [27]. This difference in complexity can also be understood by regarding the used trainable parameters, 21,771,306 for InceptionV3, and 961,305 for the second network classifying the various damage mechanisms.

Both networks were implemented in TensorFlow (v1.2.1) [30] using the Keras [31] API (v 2.1.5) with cuDNN (v 6.0.21) as backend. The clustering algorithms were implemented using scikit-learn [25].

The performance accuracy of the network was evaluated on 20% of the available data, which were retained as an independent test sample and not used in the training process. The accuracy is defined as the ratio of correctly identified images vs all available images in the sample:

$$a = \frac{\sum_{m=0}^{k-1} c_{m,m}}{\sum_{m=0}^{k-1} \sum_{n=0}^{k-1} c_{m,n}} \quad (4)$$

where $c_{m,n}$ are the elements of the confusion matrix. The uncertainty of the accuracy was determined in the following way: The CNNs are initialised using pseudo-random numbers with variable seeds. This implies that in each training round the final network weights will be slightly different due to the numerical optimisations during the training. In this regard, the true positive rate (TPR, also: recall or sensitivity) was taken as the ratio of samples correctly identified as belonging to class m and the number of all samples belonging to this class, i.e.

$$TPR = \frac{c_{m,m}}{\sum_{n=0}^{k-1} c_{n,m}} \quad (5)$$

and the positive predictive value (PPV, also: precision) as:

$$PPV = \frac{c_{m,m}}{\sum_{n=0}^{k-1} c_{m,n}} \quad (6)$$

The CNNs were run on a Linux-based system, equipped with AMD FX-8340 CPU and 32 GB RAM. For the training a GeForce GTX 1070 GPU was employed. Since GPUs are non-deterministic in the implementation of their algorithms, slight variations are expected even if all other parameters are initialised to the same values. To estimate the size of the effect, each network was trained 10 times and the mean of the resulting spread in accuracy was taken as the point estimator, and the standard deviation as the uncertainty measure.

The training of a network took typically a few hours depending on the network architecture and more importantly on the number of training samples. Training on CPU would be possible in principle but training times are expected to be significantly higher by some orders of magnitude and have thus not been attempted. Training was executed for 50 epochs for the first network and 90 epochs for the second network. Both networks were trained using the Adam optimizer with a learning rate of 0.001 for the first network and a learning rate of 0.0005 for the second network, the remaining parameters were left at their default values, i.e. $\beta_1 = 0.9$, $\beta_2 = 0.999$, $\epsilon = 10^{-8}$, and a learning rate decay of 0.0. See Figures A and B in the [S1 Supporting Information](#) for accuracy and loss as a function of epoch as well as the respective confusion matrices for the test data set.

Experimental methods

The two dual phase steels used in this work are of commercial origin (ThyssenKrupp Steel Europe AG and ArcelorMittal SA, Luxembourg) and are marketed under the label “DP800”, which warrants both a microstructure consisting of ferrite and martensite (dual-phase steel) and a tensile strength of at least 800 MPa. The microstructures differ in grain size and martensite morphology due to changes in processing and heat treatment. All tensile samples were cut out of the 1.5mm thick sheet metal by wire erosion, with the tensile axis being parallel to the rolling direction.

Metallographic preparation of all samples included mechanical grinding up to 4000 grit paper and mechanical polishing in diamond suspension in three polishing steps down to 1µm, followed by an additional final polishing step in a 0.25µm oxide suspension. All samples were lightly etched to ensure clear visibility of the ferrite and martensite constituents, while avoiding the build-up of a strong topography creating shadowing on the SEM images that might be detected as black areas by the void recognition system. For etching, a 1% Nital solution was used and the etching time was chosen to be 5 s to maintain the above-mentioned conditions.

The tensile samples were deformed by an electromechanical testing machine (DZM, in-house built) with an accuracy of ± 0.17 MPa in the stress measurement. Strains in post-mortem experiments were measured as global strains over the deformed sample area based on the elongation between two markers in the undeformed parts of the sample. For in-situ tensile tests, a smaller deformation stage (Proxima 100, MicroMecha SAS, France [32]) was used. In-situ deformation strains, in addition to the initially applied pre-strain of the samples, were extracted from the deformation of the microstructure in the observed panoramic images by digital image correlation (DIC) and averaged over the observed area of 500 x 500 µm. All tensile specimens had a gauge length of 3.6 mm, width of 1.5 mm and thickness of 1.5mm (initial sheet thickness) to ensure comparability of strains and damage behaviour after necking between in-situ and ex-situ testing.

The panoramic images were acquired using scanning electron microscopes (LEO 1530 FEG-SEM, Carl Zeiss Microscopy GmbH, Germany & FEI Helios 600i, FEI Company, USA).

All images were obtained using secondary electrons with a resolution of 32.5 nm/px (100 px horizontal field width in one image of 3072 px width). Image stitching for panoramic imaging was realised using MATLAB based on the VLFeat Matlab toolbox [33]. Damage recognition was realised by thresholding SEM grayscale images and usage of the DBSCAN algorithm before processing by the neural networks.

In the performed in-situ experiments, all samples were pre-strained to 14% global strain with reference to the initial gauge length of 3.6 mm. Additional strains were measured by averaging over a field of view in the panoramic imaging using a correlation between the individual panoramic images. The strains were averaged from the DIC measurements performed with GOM Correlate image correlation software (GOM GmbH, Germany). The so-obtained values therefore have to be regarded as average values, not over the complete sample, but rather limited to the investigated area by panoramic imaging.

Results

Separation of inclusions from deformation-induced damage

In understanding damage and deriving mechanism-based models of deformation in the dual phase microstructure of DP800 steel, one has to first distinguish between voids induced by the co-deformation of the ferrite and martensite phases and those induced around inclusions of foreign phases. Although the latter do not commonly cause a large amount of damage [34], they can introduce significant errors in the quantification of damage if they are not distinguished from the deformation-induced damage. Conventionally, damage quantification by imaging techniques is achieved by a threshold analysis of greyscale image [35] to quantify the (darkest) areas within micrographs. Particularly where inclusions fall out of the surface during preparation, this may count them incorrectly towards deformation-induced damage. We therefore implemented a first neural network (CNN1 in Fig 1) to identify inclusions, both with and without a remaining foreign phase. Thereby, we enable a separate analysis of inclusion damage, which may strongly depend on manufacturer and batch quality, and deformation-induced damage, which is governed by the phase fractions and characteristics of the microstructure. Typically, these also depend on the manufacturer and can vary between batches depending on the alloy composition and the applied heat treatment.

The first step of our damage analysis is an automated acquisition of secondary electron micrographs with a resolution of 33 nm/px and a total field width after stitching to a single panoramic image of the order of 1 mm. In order to avoid a significant contribution of shadowing to the images yet be able to distinguish between ferrite and martensite phases, the commercial-grade DP 800 steel was subjected to light chemical etching beforehand. All voids within the panoramic micrograph were recognized via a thresholded image followed by a clustering algorithm (see [Methods](#) section for more detail on material, deformation experiments and algorithms employed in this work). Discrimination between those voids originating from inclusions in the steel matrix and others stemming from deformation-induced damage was then achieved by the first convolutional neural network presented with all clustered voids obtained from the previous step of void recognition. This initial step of damage analysis achieved an accuracy of $95 \pm 1\%$, PPV of 0.92 ± 0.04 and TPR of 0.85 ± 0.07 after training on a data set containing 572 manually labelled inclusions (out of a total of 4944 manually labelled damage and artefact sites).

The relevance of this approach is illustrated in Fig 3, where the number fraction of inclusion-induced voids is presented for a series of tensile samples deformed in small strain increments from a pre-strain of 12% to a total strain of 24%. Particularly in the first one percent strain increment, the contribution of inclusions to the measured damage from a simple

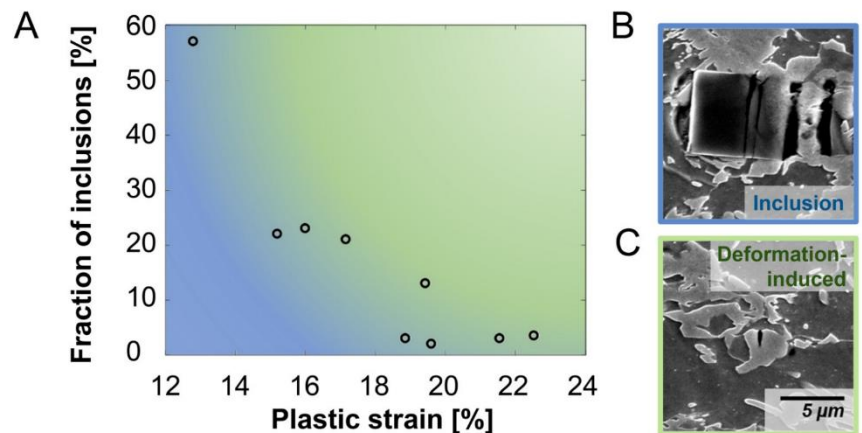


Fig 3. Separation of inclusions and deformation-induced damage. (a) Contribution of voids from inclusions to the total number of voids as a function of plastic strain in a tensile test (over an area of 0.63 mm²). Particularly at low strain levels the separation of inclusions and deformation-induced damage is essential. Micrographs illustrate the difference in size between (b) a typical inclusion and (c) a typical martensite crack induced as a result of deformation.

<https://doi.org/10.1371/journal.pone.0216493.g003>

thresholding approach is considerable with over half of the measured damage sites pertaining to inclusion damage. With respect to area fraction, there is an even greater contribution of inclusion-related voids due to their average size of $\sim 0.93 \mu\text{m}^2$ compared with an average size of deformation-induced damage sites of $\sim 0.43 \mu\text{m}^2$. We believe that the ability to quickly and automatically remove inclusions from any further analysis of damage quantity or damage mechanisms is therefore of great value not only to achieve more accurate data but also to avoid superfluous experiments or valuable characterization time spent to quantify the density of inclusions before investigation of any new batch of material. This boosts not only the accuracy of studies regarding microscale damage mechanisms but is also important for quantifications of void area fractions in deformed samples without a focus on the underlying mechanisms, such as in the analysis of damage parameters for mesoscopic process simulations.

Definition of classes of deformation-induced damage for statistical analysis

To generate a deeper understanding of the damage initiation during deformation, we started with the identification of fundamental damage mechanisms that are active in DP steel. According to a wide variety of investigations [36–38], those damage mechanisms can be narrowed down to ductile decohesion processes and fracture of brittle microstructure constituents. This results in the identification of the main mechanisms of void initiation as brittle martensite cracking and a ductile decohesion, dominated by ferrite plasticity, at either the martensite-ferrite interfaces or ferrite-ferrite grain boundaries. Note that the latter were very scarce in the present case due to their small number in the DP800 steel microstructure studied. Evolution of all types of voids, including those of martensite cracks once they have travelled across the affected martensite islands, was governed by plasticity of the surrounding ferrite grain(s).

However, our proposed approach in classifying damage sites in a statistically significant way is performed with a concept different from most previous studies—the most significant difference being the quantitative and qualitative analysis of large-area, high-resolution panoramic images. With, to our knowledge, only one notable exception [36], the studies on damage in DP steels currently available in the literature focus on relatively small areas or larger images

recorded at low to medium resolution. They therefore deal with a limited number of evaluated damage sites and often these may be selected to correspond to particularly clear examples of the individual damage mechanisms considered. In contrast, our analysis aims to provide a statistical investigation of damage evolution and mechanisms and is therefore obligated to classify all occurring voids in a large field of view. Having approached our data with the above-mentioned set of damage categories, a large percentage (40–60% depending on the level of deformation) remains outside a reliable attribution to a certain damage mechanism.

We therefore propose to employ damage categories that not only capture the dominant deformation mechanism visible at the imaged stage but also reflect (i) any transition from brittle to ductile damage and (ii) the attainable resolution to resolve this transition. Furthermore, the categories need to be simple enough to allow reliable attribution to the individual categories independent of user experience or knowledge. This is important as deep learning involves training on labelled images and the success of the approach is therefore based on our ability to reproducibly assign distinct damage classification labels. A small study on 19 materials scientists ranging from undergraduate students to experienced researchers revealed that the application of the plethora of common damage classifications including cracking and decohesion of different boundaries is not an exact science. It is prone to great deviations between individuals where voids are regularly attached to both phases in a fine microstructure or damage has evolved significantly at advanced strain levels (note that the strain levels investigated here are actually at the low end between 12–24% plastic strain compared with most other studies covering strains exceeding 50% in intervals of ~10% [10, 36]).

We therefore propose the following damage classes for a statistical and automated analysis of damage across high-resolution micrographs: (i) brittle martensite cracking, (ii) martensite-ferrite interface decohesion, and, (iii) a category labelled “notch” for short in which we collect those damage sites, which are too small to be reliably assigned to a distinct damage initiation mechanism. Mostly, these include round voids at thin martensite bridges, where one suspects the rupture of the martensite bridge due to the stress concentration to be the source of damage without the typical fracture faces that are usually clearly visible. Examples of each class are shown in Fig 1. We also explicitly labelled “evolved” damage sites that showed considerable evolution past the nucleation stage, particularly martensite cracks that had led to plastic flow in the adjoining ferrite grain(s) and therefore transitioned from pre-dominantly brittle to ductile deformation. We consciously included the category “notch” in addition to the classification of “evolved” damage in order to distinguish between those cases where it is the ductile evolution of damage that dominates the growth of the observed damage sites and those cases in which it is the lack of resolution at the sub-micron scale or strain increments that may prevent us from correctly distinguishing damage mechanisms in a freshly nucleated but diminutive void.

This leaves us with 4 clear-cut categories of damage (including the inclusion-induced voids discussed above) and the less distinct category of “evolved” damage. In order to achieve a clean training dataset for the neural networks, we therefore used only the former four categories for training of the neural networks. Clearly, the choice of training data and categories is therefore a critical point in which the main aim of the analysis is set for all following analyses using the same network. We chose to focus on the stage of nucleation of damage to achieve a clearer picture of the dominant damage nucleation mechanisms at different strain levels, leaving the analysis of evolving damage to the more appropriate method of in-situ experiments.

Strain-dependence of deformation-induced damage

In order to identify the dominant damage mechanism(s) associated with a certain strain path, in this case uniaxial tension, the relevance of both the quality and quantity of results has to be

ensured. In most DP steels, the martensite fraction is distributed heterogeneously across the material[1], mainly due to the formation of martensite bands in the rolled sheet metal. This directly necessitates the analysis of damage events across a large sample area to obtain a representative picture of the material's microstructure. This aspect is independent of the experimental method, whether it involves post-mortem or in-situ damage analysis.

Each of these methods has its strengths and weaknesses and we therefore employed both ex-situ and in-situ experiments in this study using damage quantification and classification via artificial intelligence to enable the analysis of suitably large areas. The results showed that the in-situ experiment yields significantly different damage characteristics due to evolution of damage at the free surface, as opposed to ex-situ experiments, where deformation occurs in the bulk and is revealed post-mortem. A direct application of damage classes defined using the morphologies observed after deformation in the bulk to in-situ experiments is therefore fraught with peril. In the following, we first present the ex-situ statistical analysis of damage at different strain levels followed by the results of the use of automated identification, classification and tracking of individual damage sites during their evolution in in-situ experiments.

To achieve the required size of analysed area capturing the variability in the microstructure we imaged an area of $900.000 \mu\text{m}^2$ at a resolution of $32\text{nm}/\text{px}$ for each strain step reported below. Note that these areas were recorded in the sheet plane, but the dimensions would be equally applicable to cross-sections in rolling or transverse direction to capture the gradients in grain elongation, phase morphology and banding across a typical sheet thickness of 1 mm.

We present here the gathered data on detected damage sites from tensile tests to different strains with two purposes in mind: first, to present a statistical meaningful dataset, which covers strains from 12–24% with smaller strain increments analysed to much greater statistical relevance than available elsewhere and, second, to illustrate the success of automating this laborious analysis by artificial intelligence. The latter step is crucial to make this kind of analysis possible on a regular basis in laboratories around the world. We can thereby finally overcome the challenge of comparison and transfer of data and derived models in this (and other) technologically important, yet immensely complex, class(es) of alloy(s).

The statistics reveal an exponential increase in the total number of damage sites with increasing tensile strain in the sample (Fig 4). This is commonly observed at larger strains but the expansion of this trend is confirmed here for smaller strains, which are at or below the

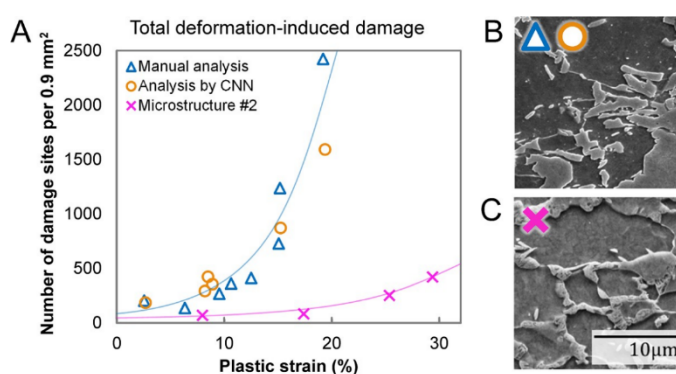


Fig 4. Evolution of total damage as a function of uniaxial strain. (a) Different panoramic micrographs were analysed manually (blue triangles) and by the CNNs (orange circles) both showing the same exponential increase in damage with strain. The drastic difference between microstructures of different DP800 grade steels is also shown for comparison (pink crosses). Micrographs of either microstructure are shown in (b) and (c).

<https://doi.org/10.1371/journal.pone.0216493.g004>

detection level in studies with larger strain increments and reduced image size or resolution. The evolution of the total number of deformation-induced damage sites, i.e. excluding inclusions, as determined by human investigator and the neural networks is virtually the same within the scatter that remains even for the large areas analysed here (Fig 4).

The damage mechanisms classified as outlined above paint an interesting picture. The relative contribution of each damage class to the overall damage (Fig 5) shows a clear trend: the fraction of undeformed, newly nucleated martensite cracks decreases significantly with the strain level. This can be rationalised on the basis that martensite cracking at lower strains occurs predominantly in distinct regions of the microstructure, namely prior austenite grain boundaries [39]. These weak and therefore brittle locations tend to fracture at relatively low stresses, which causes martensite cracks to emerge predominantly in the early stages of deformation and cease afterwards. At larger strains, the ductile mechanisms of void nucleation (phase boundary decohesion) and void plasticity (evolving voids) play an increasingly dominant role in both the nucleation and evolution of damage voids. As a result, it may be essential to guide microstructure design concepts towards damage tolerance and even distribution rather than minimisation of damage, as suggested also by Tasan et al. [1].

At this point, it is important to distinguish between the classification by a human investigator and the neural networks. As outlined above, the neural networks were trained using the categories inclusion, martensite cracking, phase boundary decohesion and notch. Strongly evolved damage sites, e.g. martensite cracks, which have already induced flow in the surrounding ferrite, were excluded in order to remove the bias of the training data, where different human investigators might not be confident that they can identify the underlying nucleation mechanism. As this distinction results in a training dataset with clearer dominance of each mechanism but cannot be based on distinct thresholds, the category of evolved damage cannot be implemented in a straightforward manner into an automated analysis by artificial intelligence. The classifications by a human investigator and the analytical algorithm consequently differ in some respects: first of all, not all sites are attributed to a mechanism by the human investigator, as a significant percentage is labelled as evolved damage sites. Most of these sites are, however, classified by the neural network as phase boundary decohesion sites due to their curved outline resulting from ductile flow, rather than brittle fracture across a straight path. While this might be a wrong classification in respect to the nucleating mechanism, it is consistent with ductile processes dominating evolution of voids at intermediate strains (Fig 5B)

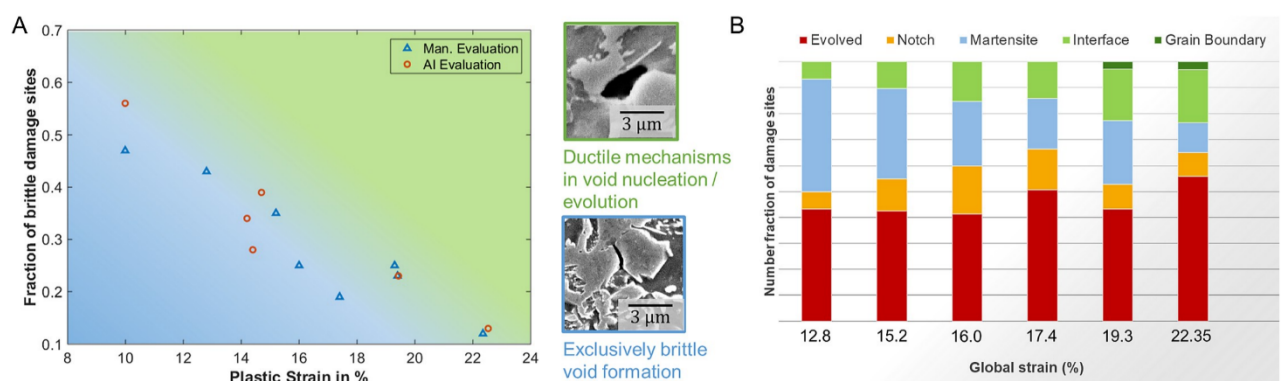


Fig 5. Change of dominant damage mechanisms with strain. The distinction between brittle and ductile damage (a) highlights the change in dominant mechanism with an only slowly increasing fraction of significantly evolved damage sites to the overall damage at increasing strains (b).

<https://doi.org/10.1371/journal.pone.0216493.g005>

regardless of nucleation mechanism, which is the original definition of those evolved damage sites. The classification accuracy of the brittle martensite cracks is higher with $85 \pm 6\%$ compared with the accuracy of identifying all classes ($80 \pm 6\%$). The division into voids that have an exclusively brittle origin and those that have nucleated or grown under the influence of ductile plastic flow in the nearest vicinity of the void is shown in Fig 4A.

To quantify the considerable differences in damage behaviour in different grades of commercial DP800 steel, a second microstructure containing a different martensite morphology was investigated. This material showed not only a higher ductility, but interestingly also a significantly lower number of nucleating damage sites during tensile deformation (Fig 4A). The observed behaviour underlines the need for large-area studies of each grade of investigated dual phase steel to achieve reliable predictions about their individual damage characteristics and exploit the full potential of the flexible processing conditions of these steels to achieve the most favourable, damage tolerant microstructures. These vital investigations can only be performed in a suitable timescale with the help of automation.

Discussion

In dual phase steels, investigation of a large area at high resolution is essential to provide comparability and transferability of results within this class of materials due to the scale of the microstructure and damage initiation at the sub- μm scale coupled with material heterogeneity up to the mm-scale. The results from our comparison of damage evolution in two different DP800 microstructures underlines this. The stark difference in damage densities with strain will make it necessary to statistically quantify and classify the damage mechanisms and their occurrence in every grade of DP-steel commercially available by combining high-resolution imaging at the scale of the damage mechanisms and large-scale observations to obtain sufficient statistics. To achieve an accurate and transferable results in characterising and, ultimately, predicting damage nucleation and evolution in any specific dual-phase microstructure, these time-consuming statistical analyses need to be conducted for each distinct material grade. Such an endeavour is in fact feasible via our automated approach as it is able to handle a high volume of damage sites in a drastically reduced amount of time compared to a human investigator.

Using a neural network to classify images into different damage categories leads us beyond the common threshold analysis of greyscale images. It allows us to distinguish not only the constituent ferrite and martensite phases and related pores from the surrounding matrix, but also distinguish other types of pores. In particular, image classification allows us to treat inclusions and the pores they cause where they may have fallen out during metallographic surface preparation separately from deformation-induced damage. This is of particular importance at small strains and where damage is quantified by means of an area fraction.

Owing to the large number of damage sites observed at high resolution, we could show for example that martensite cracking precedes what is often classified as phase boundary decohesion in later stages of damage evolution. Over a strain interval of 12–24% plastic strain, we further demonstrated a pronounced change in governing damage mechanisms from brittle martensite fracture at the onset of damage to ductile damage initiation and evolution at higher strains. This is consistent with the observations from the literature, where martensite cracking is frequently reported as the dominant mechanism of damage initiation (e.g. Asik et al [40]) and interface decohesion as the dominant mechanism at larger plastic strains (e.g. Hoefnagels et al. [36]). As described by Azuma [41], the main cause for this transition from brittle to ductile damage can be found in the morphological evolution of voids. This is because such evolution often results in a convolution of different damage mechanisms; those which govern the stages of damage initiation, and those governing damage evolution. Naturally, this results in unclassified

damage in the context of automated damage analysis focused on distinct nucleation mechanisms. This was also shown by Hoefnagels et al. [36] for the ductile growth of a brittle martensite fracture into the ferrite matrix. Although their large dataset recorded at medium resolution allowed only an indirect proof, it highlighted the need for high resolution images to support their hypothesis with more direct but, again, statistically less representative data. A comparison of the two datasets recorded at medium and high resolution [36] further highlights the importance of acknowledging the limit of resolution to which damage sites can be detected or categorized. In their quantification of damage in a biaxial tension experiment, the measured damage density increased by a factor of nearly 15 between the data measured at medium resolution over an area of $450,000 \mu\text{m}^2$ and that identified over an area of $38,200 \mu\text{m}^2$ at high resolution.

While statistical evaluation of deformed samples provides the important quantification of the number or area of damage sites and the dominance of each mechanism for a given strain level, it cannot deliver local information about the specific evolution of individual damage sites. To achieve this, additional in-situ tensile tests within an SEM were performed, completing the picture of damage statistics with time-resolved information at high resolution. The experiments were performed in such a way that a pre-strain of 14% was imposed prior to surface preparation for the in-situ observation, providing a pre-damaged state at the start of the in-situ test. This was necessary because the overall strain increment is usually limited by the formation of artefacts due to surface roughening from plastic flow at the open surface. The induced damage sites were then identified from the previously acquired panoramic image and classified in this state, which is equivalent to the post-mortem analysis presented above. Each site of interest can then be automatically tracked over subsequent in-situ deformation steps and pre-processed to achieve efficient analysis and interpretation as shown in Fig 6.

Our in-situ tests show that the prevalence of nucleation of different types of damage sites is affected by the chosen method of investigation. For example, phase boundary decohesion, seen frequently in the post-mortem analysis of bulk samples, was barely encountered in the in-situ tests. Instead, plastic flow at the free surface caused “sink-in” of the ferrite matrix that led to the formation of deformation artefacts in the form of trenches (Fig 7). These artefacts, which are attributed to the altered stress state at the free surface of the deformed sample, were typically found to follow the martensite/ferrite interphase boundaries. The formation of surface artefacts during in-situ testing and damage analysis therefore poses a major difficulty in assessing the nucleation and evolution of phase boundary decohesion processes during plastic deformation as the dominant flow patterns in the bulk (see also Fig 7) and at the free surface clearly differ. Transfer of insights from in-situ experiments to bulk deformation, the dominant situation in metal forming due to the large volume to surface ratio, is therefore not possible with respect to ductile damage nucleation and evolution of brittle damage by flow. In this respect, in-situ experiments should be treated with great caution and used only to couple the plastic flow in the ductile phase observed in simulation and experiment where micromechanical crystal plasticity models are used to re-create the in-situ situation.

In contrast, the brittle mechanisms of martensite fracture appeared largely unaffected by the free surface in terms of their morphology. Further analysis of the nucleated martensite cracks during in-situ testing is therefore much more likely to shed a reliable light on the evolution of these damage sites with increasing strain level. This allowed us to not only track pre-existing damage site caused by martensite cracking in their evolution during the in-situ experiment, but also identify newly nucleated sites in subsequent deformation steps. These were then back-tracked to the pristine site (Fig 6A), giving us the opportunity to observe the onset of martensite cracking at numerous locations.

Across all sites of martensite cracking, we found that while some sites exhibited rapid growth as a result of plasticity in the ductile ferrite phase (Fig 5B), other sites showed virtually no

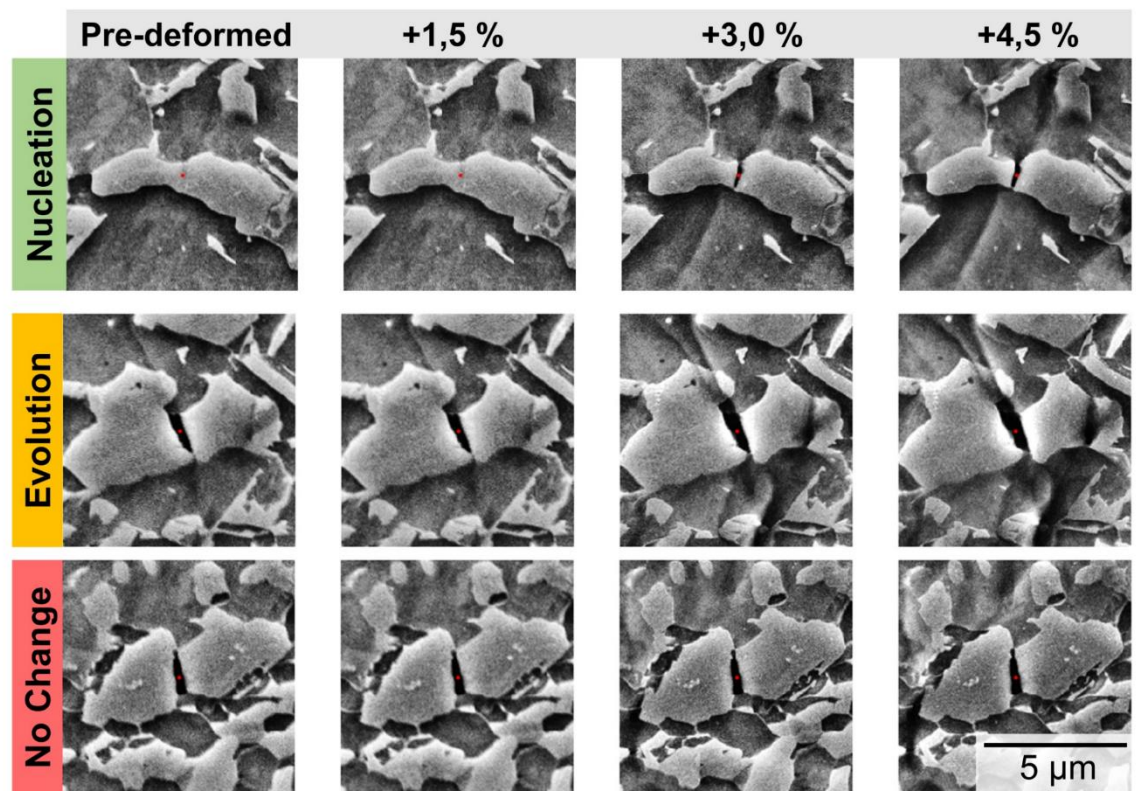


Fig 6. Automatically detected and classified martensite cracks. Crack development during in-situ experiments, showing (a) the nucleation stage and following crack propagation stage, (b) crack opening and evolution dominated by ductile behaviour in adjacent ferrite grains and (c) a similar martensite morphology as in (b) revealing no appreciable change over time at the same strain increments. The three-dimensional flow of the ferrite phase at the free surface in in-situ experiments leads to the formation of surface artefacts around the martensite islands in the form of trenches (indicated by white arrows in (b) and (c)), see also Fig 7.

<https://doi.org/10.1371/journal.pone.0216493.g006>

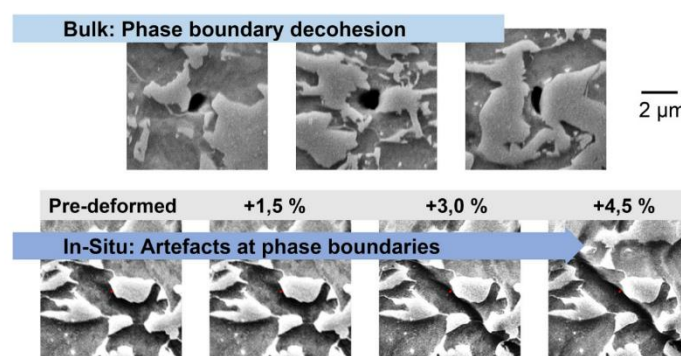


Fig 7. Differences between bulk and in-situ experiments. Plastic flow near phase boundaries between ferrite and martensite manifests very differently during deformation in the bulk and at the free surface in in-situ tests. In the bulk, it is dominated by phase boundary decohesion, while the surface is governed by artefacts due to flow normal to the free surface.

<https://doi.org/10.1371/journal.pone.0216493.g007>

change in comparison to the pre-strained state (Fig 5C). Intuitively, a first expectation about the evolution of an existing martensite crack would be that further growth occurs, assisted by plasticity in the ductile ferrite phase. However, this behaviour was not observed across all cracks identified in the pre-damaged state. For cracks that do not show any clear difference in morphology or surrounding microstructure, like those shown in Fig 5B and 5C, the evolution process differs significantly from virtually no change in c) to a pronounced plasticity around the void and crack opening in b). Presumably, this is due to a change in the stress-state as the surface is cut free and half the surrounding martensite or ferrite structures are removed. The prevalence of this phenomenon is, however, important as it highlights how easily our view on damage evolution in in-situ experiments can be distorted, where only selected sites are reported, normally those that do show the evolution phenomena at the heart of most investigations.

The comparison of the results obtained in an in-situ test with our results on statistical damage analysis of material deformed in bulk (ex-situ) highlights the importance of large-area datasets and the observation of bulk deformation as the essential reference case, even where the experimental facilities for elegant in-situ tests are readily available. An ex-situ evaluation is unable to reveal the evolution of individual voids, however, it is essential to consider that the in-situ observation of void nucleation and evolution at the surface causes a substantial variation in void nucleation and evolution. This is widely acknowledged, but without the possibility of statistical analyses to reveal which damage mechanisms constitute the typical bulk case, crucial differences, like the altered void growth behaviour of martensite cracks at the free surface, are hard to quantify rigorously as an in-situ artefact caused by the free surface. Of course, the out-of-plane component of flow in in-situ experiments may still be considered in conjunction with crystal plasticity modelling, but so far, a truly quantitative evaluation is impeded by the experimental difficulties again encountered when combining high resolution and investigation of large areas [42, 43].

Our comparison of the statistical analysis of damage in bulk and that at the free surface reveals that in-situ tests are, however, representative in the context of brittle fracture in martensite. In this case, each individual martensite island present in the bulk or being part of the free surface may of course experience an altered stress state, leading to the absence of further growth of damage induced in the bulk during subsequent in-situ deformation. Still, the general morphology of martensite cracks remains the same and in-situ tests are therefore ideally suited to reveal the mechanisms of brittle damage nucleation. In-situ tracking of martensite cracks also included the ductile growth of a fraction of these originally brittle martensite cracks. This process portrays the transition to ductile mechanisms after brittle cracking. It was, in a similar way, observed in the material after bulk deformation as an increasing dominance of ductile mechanisms in void evolution (Fig 5B). While the nucleation and evolution of damage by plastic deformation at the surface is difficult to interpret directly, it does reveal the assumed link between the nucleation and evolution stage: not only do ductile nucleation mechanisms become more dominant at larger global strains, but site-specific ductile mechanisms of void evolution take over at previously brittle nucleation sites of martensite cracking.

The neural networks developed in this study reduced the time required for micrograph analysis in terms of damage classification from days to minutes. While identifying and classifying a single damage site takes a human investigator about 20 s, leading to 5.5 hours per panoramic image with ~ 1000 damage sites, the use of trained artificial intelligence for this purpose reduces the time required to less than 1 minute (Fig 8). Depending on the required accuracy, the human investigator can instead focus on interpretation of the data and, where applicable, the few remaining unclassified cases, resulting in a total duration of a few minutes. In this context, we have also shown that a good performance can be attained based on a limited number of damage sites that can be acquired within a few hours. This was by no means pre-evident, as the underlying algorithms are commonly applied where millions of labelled, yet more variable and complex,

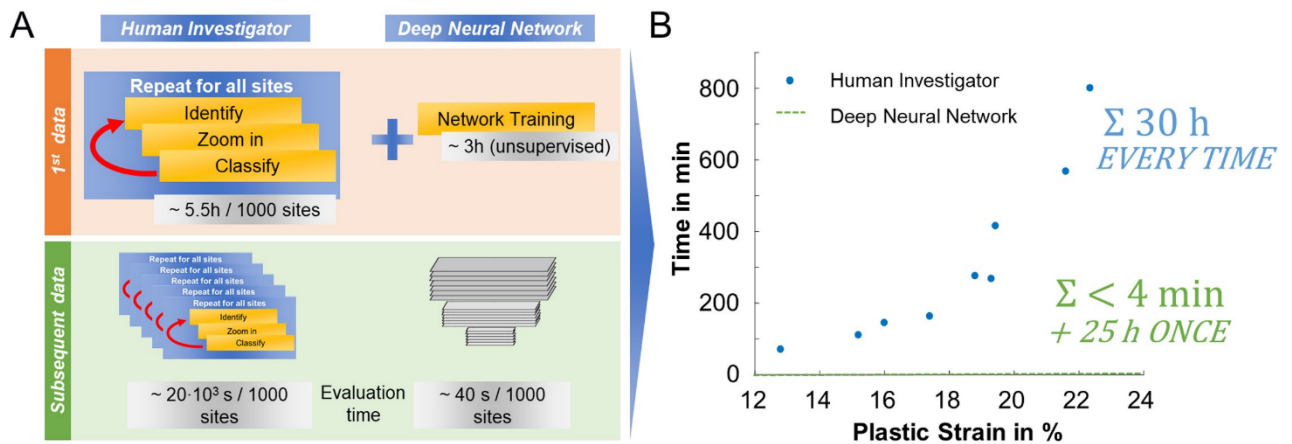


Fig 8. Time advantage of the proposed approach. (a) A direct comparison of the time invested (human investigator vs. artificial intelligence) in acquiring and processing initial and subsequent datasets of damage sites and (b) how the required time scales when evaluating strain dependent damage.

<https://doi.org/10.1371/journal.pone.0216493.g008>

images are available [44], e.g. from social media. Where mechanisms are of interest that occur rarely, i.e. a few times across an area of the order of 1 mm^2 , but may be critical for material performance, the analysis by artificial intelligence is of particular help as it supports the researcher in the identification of atypical cases across large areas prohibitive to manual investigation. Such sites may then be represented in a new class of damage and fed back into the training dataset.

The use of automated recognition and analysis of damage sites by artificial intelligence in combination with in-situ testing is not an end in itself. Beyond the ability to evaluate representative datasets and save human supervision time on repeated analyses of similar microstructures, the approach enables studies that were previously inaccessible due to the constraints on human time; for example, the quantification of damage sequences in a statistical manner and coupling with high-throughput simulation to overcome the challenge of the missing 3D microstructure information where no suitable experimental methods [36, 45] are available. The method made available here brings together efforts in materials science and civil engineering. While the former community has used similar methods to those presented here in order to classify entire microstructures or their components [18, 46–48], the detection of damage has mostly been restricted to structural materials at the scale of buildings or bridges [49–51] and therefore investigated based on much lower resolution (photographic) images. This work links both worlds by considering damage, but, using electron microscopy, down to the microstructural level considered essential to the understanding, modelling and design of materials in high performance applications. We foresee many more applications of this approach in the future and hope that open availability of the developed neural networks and algorithms will encourage and enable others to apply these methods easily to their own investigations.

Conclusions

In this study, we successfully implemented a high-resolution large-scale analysis with high throughput to provide damage quantification and classification in ex-situ and in-situ experiments. The following conclusions can be drawn:

- For complex, heterogeneous microstructures, such the ones encountered in dual-phase steels, the use of trained convolutional neural networks to classify a large number of damage

sites at high resolution has proven extremely useful in gathering statistical information of representative damage mechanisms.

- For engineering purposes concerned with quantification of damage by means of an area fraction, it is prudent to split the automated classification work into two separate networks. The first network is to discriminate voids formed due to foreign inclusions from those induced by plastic deformation, and the second is to classify deformation-induced damage in conjunction with responsible damage mechanisms.
- A separate treatment of inclusion-induced and deformation-induced damage (as previously mentioned) provides a valuable improvement in accuracy for quantitative evaluation of damage statistics, especially at low deformation strains, where in the present case over half of the measured damage sites were affiliated with inclusion damage.
- The statistical viewpoint made possible by our approach unravels a more complete picture of the dominant deformation-induced damage mechanisms depending on the strain level. At incipient stages of deformation and damage initiation, brittle martensite cracking seemed to be the prevailing mechanism. An increasing amount of plastic deformation dominates at larger strains and led to rapid growth of voids and expansions of martensite cracks into the adjacent plastic ferrite phase.
- The damage behaviour of martensite cracking was reproduced in in-situ experiments since it was not affected by the surface artefacts generated upon straining. However, the morphology of the ductile damage sites were found to differ considerably from the bulk case. This highlights the need not to rely too heavily on in-situ experiments and interpret respective findings and their implications for bulk damage behaviour with great care.
- The present approach can, in principle, be transferred to similar image-based challenges in other complex microstructures at all scales. In the context of dual phase steels, a meaningful comparison of the manifold of microstructures subsumed under each industrial grade would be an exceedingly fruitful next step that now appears within reach. If successful, it would truly bring together the insights into the materials physics of deformation-induced damage, currently scattered across laboratories worldwide to enable more powerful knowledge-driven microstructure and process design for this important material class.
- Finally, any image recognition algorithm would have its limitation in real microstructures due to the complex interplay of individual damage formation mechanisms, rendering a major proportion of damage sites not clearly attributable to a single mechanism. Although we chose to focus on the mechanisms initiating damage in this work, we do note that in future work it should be feasible to further sub-categorize evolved damage based on sequential evolution stages associated with the onset of additional mechanisms.

Supporting information

S1 Supporting information. Network details and performance. This supporting information contains a more detailed description of the network and relevant terms in Table 2 of the main document, the accuracy and loss for the first and second classifier as a function of epoch with the confusion matrices for the test data, a comparison of different networks tested for this work and a comment on validation and hyperparameters.
(PDF)

Author Contributions

Conceptualization: Ulrich Kerzel, Sandra Korte-Kerzel.

Data curation: Tom Reclik, Martina Freund.

Formal analysis: Carl Kusche, Martina Freund, Sandra Korte-Kerzel.

Funding acquisition: Talal Al-Samman, Sandra Korte-Kerzel.

Investigation: Carl Kusche, Tom Reclik, Ulrich Kerzel.

Methodology: Carl Kusche, Tom Reclik, Talal Al-Samman, Ulrich Kerzel, Sandra Korte-Kerzel.

Software: Tom Reclik, Ulrich Kerzel.

Supervision: Talal Al-Samman, Ulrich Kerzel, Sandra Korte-Kerzel.

Writing – original draft: Carl Kusche, Talal Al-Samman, Ulrich Kerzel, Sandra Korte-Kerzel.

Writing – review & editing: Carl Kusche, Tom Reclik, Martina Freund, Talal Al-Samman, Ulrich Kerzel, Sandra Korte-Kerzel.

References

1. Tasan CC, Diehl M, Yan D, Bechtold M, Roters F, Schemmann L, et al. An overview of dual-phase steels: advances in microstructure-oriented processing and micromechanically guided design. *Annual Review of Materials Research*. 2015; 45:391–431.
2. Calcagnotto M, Adachi Y, Ponge D, Raabe D. Deformation and fracture mechanisms in fine- and ultra-fine-grained ferrite/martensite dual-phase steels and the effect of aging. *Acta Materialia*. 2011; 59:658–70.
3. Avramovic-Cingara G, Ososkov Y, Jain MK, Wilkinson DS. Effect of martensite distribution on damage behaviour in DP600 dual phase steels. *Materials Science and Engineering*. 2009; 516:7–16.
4. Zhang J, Di H, Deng Y, Misra RDK. Effect of martensite morphology and volume fraction on strain hardening and fracture behavior of martensite–ferrite dual phase steel. *Materials Science and Engineering A*. 2015; 627:230–40.
5. Kang J, Ososkov Y, Embury JD, Wilkinson DS. Digital image correlation studies for microscopic strain distribution and damage in dual phase steels. *Scripta Materialia*. 2007; 56:999–1002.
6. Landron C, Maire E, Bouaziz O, Adrien J, Lecarme L, Bareggi A. Validation of void growth models using X-ray microtomography characterization of damage in dual phase steels. *Acta Materialia*. 2011; 59(20):7564–73.
7. Maire E, Bouaziz O, Di Michiel M, Verdu C. Initiation and growth of damage in a dual-phase steel observed by X-ray microtomography. *Acta Materialia*. 2008; 56(18):4954–64.
8. Wu Z, Sandlöbes S, Wu L, Hu W, Gottstein G, Korte-Kerzel S. Mechanical behaviour of Zn–Al–Cu–Mg alloys: Deformation mechanisms of as-cast microstructures. *Materials Science and Engineering: A*. 2016; 651:675–87.
9. Tasan CC, Hoefnagels JPM, Dekkers ECA, Geers MGD. Multi-Axial Deformation Setup for Microscopic Testing of Sheet Metal to Fracture. *Experimental Mechanics*. 2012; 52:669–78.
10. Ghadbeigi H, Pinna C, Celotto S, Yates JR. Local plastic strain evolution in a high strength dual-phase steel. *Materials Science and Engineering*. 2010; 527:5023–32.
11. Besson J. Continuum models of ductile fracture: a review. *International Journal of Damage Mechanics*. 2010; 19(1):3–52.
12. McClintock FA. A criterion for ductile fracture by the growth of holes. *Journal of applied mechanics*. 1968; 35(2):363–71.
13. Gurson AL. Continuum theory of ductile rupture by void nucleation and growth: Part I—Yield criteria and flow rules for porous ductile media. *Journal of engineering materials and technology*. 1977; 99(1):2–15.
14. Lemaitre J, Dufailly J. Damage measurements. *Engineering Fracture Mechanics*. 1987; 28(5–6):643–61.

15. Kim D, Kim W, Han J, Woo W, Choi S. Effect of microstructural factors on void formation by ferrite/ martensite interface decohesion in DP980 steel under uniaxial tension. *International Journal of Plasticity*. 2017; 94:3–23.
16. Calcagnotto M, Ponge D, Demir E, Raabe D. Orientation gradients and geometrically necessary dislocations in ultrafine grained dual-phase steels studied by 2D and 3D EBSD. *Materials Science and Engineering A*. 2010; 527:2738–46.
17. Kadkhodapour J, Butz A, Ziaei-Rad S, Schmauder S. A micro mechanical study on failure initiation of dual phase steels under tension using single crystal plasticity model. *International Journal of Plasticity*. 2011; 27:1103–25.
18. Azimi SM, Britz D, Engstler M, Fritz M, Mücklich F. Advanced Steel Microstructural Classification by Deep Learning Methods. *Scientific Reports*. 2018; 8(2128).
19. LeCun Y, Bottou L, Bengio Y, Haffner P. Gradient-based learning applied to document recognition. *Proceedings of the IEEE*. 1998; 86(11):2278–324.
20. Russakovsky O, Deng J, Su H, Krause J, Satheesh S, Ma S, et al. Imagenet large scale visual recognition challenge. *International journal of computer vision*. 2015; 115(3):211–52.
21. Litjens G, Sánchez CI, Timofeeva N, Hermesen M, Nagtegaal I, Kovacs I, et al. Deep learning as a tool for increased accuracy and efficiency of histopathological diagnosis. *Scientific Reports*. 2016; 6:26286. <https://doi.org/10.1038/srep26286> <https://www.nature.com/articles/srep26286#supplementary-information>. PMID: 27212078
22. Esteva A, Kuprel B, Novoa RA, Ko J, Swetter SM, Blau HM, et al. Dermatologist-level classification of skin cancer with deep neural networks. *Nature*. 2017; 542:115. <https://doi.org/10.1038/nature21056> PMID: 28117445
23. Cha Y-J, Choi W, Büyükoztürk O. Deep Learning-Based Crack Damage Detection Using Convolutional Neural Networks. *Computer-Aided Civil and Infrastructure Engineering*. 2017; 32(5):361–78. <https://doi.org/10.1111/mice.12263>
24. Samuel AL. Some Studies in Machine Learning Using the Game of Checkers. *IBM Journal of Research and Development*. 1959; 3(3):210–29. <https://doi.org/10.1147/rd.33.0210>
25. Pedregosa F, Varoquaux G, Gramfort A, Michel V, Thirion B, Grisel O, et al. Scikit-learn: Machine learning in Python. *Journal of machine learning research*. 2011; 12(Oct):2825–30.
26. Ester M, Kriegel H-P, Sander J, Xu X, editors. A density-based algorithm for discovering clusters in large spatial databases with noise. *Kdd*; 1996.
27. Szegedy C, Vanhoucke V, Ioffe S, Shlens J, Wojna Z, editors. Rethinking the inception architecture for computer vision. *Proceedings of the IEEE conference on computer vision and pattern recognition*; 2016.
28. Xu B, Wang N, Chen T, Li M. Empirical evaluation of rectified activations in convolutional network. *arXiv preprint arXiv:150500853*. 2015.
29. Clevert D-A, Unterthiner T, Hochreiter S. Fast and accurate deep network learning by exponential linear units (elus). *arXiv preprint arXiv:151107289*. 2015.
30. Abadi M, Agarwal A, Barham P, Brevdo E, Chen Z, Citro C, et al. TensorFlow: large-scale machine learning on heterogeneous systems. Software available from tensorflow. org. 2015. URL <https://www.tensorflow.org>. 2015.
31. Chollet F, et al. Keras. GitHub. 2015.
32. Caer C, Pesci R. Local behavior of an AISI 304 stainless steel submitted to in situ biaxial loading in SEM. *Materials Science and Engineering: A*. 2017; 690:44–51.
33. Vedaldi A, Fulkerson B. VLFeat: An Open and Portable Library of Computer Vision Algorithms. <http://www.vlfeat.org/>. 2008.
34. Tasan CC, Hoefnagels JPM, Diehl M, Yan D, Roters F, Raabe D. Strain localization and damage in dual phase steels investigated by coupled in-situ deformation experiments and crystal plasticity simulations. *International Journal of Plasticity*. 2014; 63:198–210.
35. Tasan C, Hoefnagels J, Geers M. Identification of the continuum damage parameter: An experimental challenge in modeling damage evolution. *Acta Materialia*. 2012; 60(8):3581–9.
36. Hoefnagels JPM, Tasan CC, Maresca F, Peters FJ, Kouznetsova VG. Retardation of plastic instability via damage-enabled microstrain delocalization. *Journal of Materials Science*. 2015; 50:6882–97.
37. Kadkhodapour J, Butz A, Rad SZ. Mechanisms of void formation during tensile testing in a commercial, dual-phase steel. *Acta Materialia*. 2011; 59:2575–88.
38. Lai Q, Bouaziz O, Gouné M, Brassart L, Verdier M, Parry G, et al. Damage and fracture of dual-phase steels: Influence of martensite volume fraction. *Materials Science and Engineering*. 2015; A 646:322–31.

39. Archie F, Li X, Zaefferer S. Micro-damage initiation in ferrite-martensite DP microstructures: A statistical characterization of crystallographic and chemical parameters. *Materials Science and Engineering*. 2017;A 701:302–13.
40. Aşık EE, Perdahcioğlu ES, van den Boogaard AH. Microscopic investigation of damage mechanisms and anisotropic evolution of damage in DP600. *Materials Science and Engineering: A*. 2019; 739:348–56. <https://doi.org/10.1016/j.msea.2018.10.018>
41. Azuma M. Structural control of void formation in dual phase steels2007.
42. Yan D, Tasan CC, Raabe D. High resolution in situ mapping of microstrain and microstructure evolution reveals damage resistance criteria in dual phase steels. *Acta Materialia*. 2015; 96:399–409.
43. Zhu T, Sutton MA, Li N, Orteu J-J, Cornille N, Li X, et al. Quantitative stereovision in a scanning electron microscope. *Experimental Mechanics*. 2011; 51(1):97–109.
44. Deng J, Dong W, Socher R, Li L-J, Li K, Fei-Fei L, editors. Imagenet: A large-scale hierarchical image database. *IEEE Conference on Computer Vision and Pattern Recognition* 2009; 2009: IEEE.
45. Korte S, Ritter M, Jiao C, Midgley P, Clegg W. Three-dimensional electron backscattered diffraction analysis of deformation in MgO micropillars. *Acta Materialia*. 2011; 59(19):7241–54.
46. DeCost BL, Lei B, Francis T, Holm EA. High Throughput Quantitative Metallography for Complex Microstructures Using Deep Learning: A Case Study in Ultrahigh Carbon Steel. *Microscopy and Microanalysis*. 2019; 25(1):21–9. Epub 03/14. <https://doi.org/10.1017/S1431927618015635> PMID: 30869574
47. DeCost BL, Francis T, Holm EA. Exploring the microstructure manifold: Image texture representations applied to ultrahigh carbon steel microstructures. *Acta Materialia*. 2017; 133:30–40. <https://doi.org/10.1016/j.actamat.2017.05.014>
48. Dimiduk DM, Holm EA, Niezgoda SR. Perspectives on the Impact of Machine Learning, Deep Learning, and Artificial Intelligence on Materials, Processes, and Structures Engineering. *Integrating Materials and Manufacturing Innovation*. 2018; 7(3):157–72. <https://doi.org/10.1007/s40192-018-0117-8>
49. Xu Y, Bao Y, Chen J, Zuo W, Li H. Surface fatigue crack identification in steel box girder of bridges by a deep fusion convolutional neural network based on consumer-grade camera images. *Structural Health Monitoring*. 2018; 0(0):1475921718764873. <https://doi.org/10.1177/1475921718764873>
50. Cha Y-J, Choi W, Suh G, Mahmoudkhani S, Büyüköztürk O. Autonomous Structural Visual Inspection Using Region-Based Deep Learning for Detecting Multiple Damage Types. *Computer-Aided Civil and Infrastructure Engineering*. 2018; 33(9):731–47. <https://doi.org/10.1111/mice.12334>
51. Wang N, Zhao X, Zhao P, Zhang Y, Zou Z, Ou J. Automatic damage detection of historic masonry buildings based on mobile deep learning. *Automation in Construction*. 2019; 103:53–66. <https://doi.org/10.1016/j.autcon.2019.03.003>

Publication #2

On the effect of strain and triaxiality on void evolution in a heterogeneous microstructure – A statistical and single void study of damage in DP800

Carl F. Kusche, Felix Pütz, Sebastian Münstermann, Talal Al-Samman, Sandra Korte-Kerzel

Materials Science and Engineering: A, 799, 2 January 2021, 140332

<https://doi.org/10.1016/j.msea.2020.140332>

For this publication, the candidate performed all SEM observations, and computational analysis of the various tensile samples. The statistical evaluation and interpretation of the obtained data on voids was carried out by the candidate, as well as the writing of the original manuscript and finally published version, in cooperation with the co-authors.



On the effect of strain and triaxiality on void evolution in a heterogeneous microstructure – A statistical and single void study of damage in DP800 steel

Carl F. Kusche^{a,*}, Felix Pütz^b, Sebastian Münstermann^b, Talal Al-Samman^a, Sandra Korte-Kerzel^a

^a Institute for Physical Metallurgy and Materials Physics, RWTH Aachen University, 52062 Aachen, Germany

^b Steel Institute, RWTH Aachen University, Intzestrasse 1, 52074 Aachen, Germany

ARTICLE INFO

Keywords:

Dual-phase steel
Damage
FE-Simulations
Stress state
Deep learning
Triaxiality

ABSTRACT

In order to improve the understanding of damage evolution in mechanically heterogeneous microstructures, like the ones of dual-phase steels, the influence of the applied stress state is a key element. In this work, we studied the influence of the globally applied stress state on the evolution of damage in such a microstructure. Classical damage models allow predictions of damage during deformation based on considerations of the material as an isotropic continuum. Here, we investigate their validity in a dual phase microstructure that is locally dominated by its microstructural morphological complexity based on a statistical ensemble of thousands of individual voids formed under different stress states. For this purpose, we combined a calibrated material model incorporating damage formation to assess the local stress state in samples with different notch geometries and high-resolution electron microscopy of large areas using a deep learning-based automated micrograph analysis to detect and classify microstructural voids according to their source of origin. This allowed us to obtain both the continuum stress state during deformation and statistically relevant data of individual void formation. We found that the applied plastic strain is the major influence on the overall number, and therefore the nucleation of new voids, while triaxiality correlates with the median void size, supporting its proposed influence on void growth. In contrast, coalescence of voids leading to failure appears related to local instabilities in the form of shear band formation and is therefore only indirectly determined by the global stress state in that it determines the global distribution, density and size of voids.

1. Introduction

Dual-phase steels, as a widely applied variety of advanced high-strength steels (AHSS), have yielded a high research interest for many years, especially focusing on their deformation behaviour [1–4] and formation of microstructural damage [5–7] in the form of deformation-induced voids. Due to the contrast in mechanical behaviour between their constituting phases, ferrite and martensite, a complex partitioning of stresses and strains takes place. This behaviour has been analysed by both simulative and experimental approaches [8–10].

The micromechanical mechanisms of void initiation are commonly identified as a brittle cleavage fracture of martensite islands (martensite cracking), in contrast to plastic decohesion processes of martensite-ferrite interfaces and ferrite-ferrite grain boundaries [6,11]. However,

which of these mechanisms contributes more to damage and eventually material failure, will depend mainly on the type of considered dual-phase microstructure, stress conditions and applied strain [8,11,12].

Modern in-situ deformation devices operated inside high-resolution scanning electron microscopes (SEM) are able to visualize these micro-mechanical mechanisms of void initiation as well as the development of voids during deformation [13], but under an altered stress state due to the free surface in an in-situ experiment. Additionally, the intrinsic microstructural heterogeneity of commercial dual-phase steels in terms of phase morphology, distribution and density at both the μm and mm (sheet) scale leads to a dominance of the local, microscopic stress state, caused by the individual morphology of the local microstructure on the initiation and growth of voids at each site.

* Corresponding author.

E-mail address: kusche@imm.rwth-aachen.de (C.F. Kusche).

<https://doi.org/10.1016/j.msea.2020.140332>

Received 8 June 2020; Received in revised form 6 August 2020; Accepted 25 September 2020

Available online 30 September 2020

0921-5093/© 2020 Elsevier B.V. All rights reserved.

Consequently, experiments proving the dependence of damage in the bulk material on stress triaxiality in the intrinsically heterogeneous dual-phase microstructures are more challenging. Although the effect of triaxiality on damage evolution is believed to result predominantly in the growth of voids, experimental studies largely relied on model materials with simple microstructures to ensure a homogeneous stress distribution along the samples [14,15]. However, due to the individual conditions of the local microstructure, and therefore stress, strain and deformation conditions [4,16,17], as well as the typically very heterogeneous distribution of phases in commercially applied dual phase steel sheets, statistical information gained through high resolution inspection of large deformed areas is vital to accurately assess the magnitude of introduced damage [11,18].

Recently, automation based on neural networks has been applied to enhance segmentation of microstructural features in these types of steels [19] as well as to classify different types of damage events in order to obtain significantly larger amounts of statistical data on operative damage mechanisms [12]. Applying such automated recognition and analysis tools for deformation-induced voids is advantageous in two ways:

- (i) It enables a simple, statistical approach on large areas to reveal global quantities, such as a damage variable in the sense of e.g. a void area fraction.
- (ii) It regards every emerging microstructural void individually, so that individual measurements of damage parameters like void size, morphology and mechanism of initiation are obtainable.

In this way, we employ statistics of individual voids and correlate these to stress and strain parameters in order to gain information about the fundamental mechanisms of void formation stages, classically identified as void initiation, growth and coalescence [20].

In theoretical approaches [21], stress-state dependent factors have been proposed, in particular a direct influence of stress triaxiality on the intensity of damage. Experimentally, this dependence could be verified using both SEM-based [22] and 3D-microtomography methods [15]. However, these connections are much more challenging to identify when dealing with real microstructures that typically show a significantly altered and locally heterogeneous stress and strain due to their microstructure [13]. This microstructural heterogeneity has been proven to lead to a significant inhomogeneity in spatial damage distribution [18] and development of apparently similar individual damage site in an in-situ experiment observing the material surface [12]. Therefore, expected correlations between damage and the continuum stress state would only be expected to match experimental data in a statistical way.

In this work, we employ large-area void statistics to reveal the convergence of the damage statistics in a heterogeneous and complex dual-phase microstructure against the theoretical expectations for the stress state influence expected for isotropic, homogeneous materials in a statistical ensemble of thousands of voids. In this way, the widely-applied models of damage evolution [23] are appraised with respect to the postulated causes for void initiation and growth that can now be tracked and attributed to specific parameters of stress and strain through the application of statistical evaluation in a real microstructure. For the third fundamental mechanism of damage formation in dual-phase steels, void coalescence, preceding stages of void nucleation and growth have been observed prior to failure of the sample [24], and attributed to the existence of shear bands [7].

In order to understand the failure behaviour of the deformed material, it is crucial to understand the complex interplay between the aforementioned mechanisms. De Geus et al. [25] reported that loading conditions, as well as microstructural factors like mechanical contrast between the constituting phases, volume fraction and morphology exert a strong influence on the failure behaviour. Considerable theoretical and experimental efforts to model the failure process were made by

Ramanzani et al. [20], who however did not take the formation of deformation-induced voids into account. While an interaction between the introduced voids and the process of sample failure has been described earlier [7], the global patterns and dependencies of these interactions have yet to be unravelled. This is particularly important due to the necessary large-scale, high-resolution observations. Equally, extensive advances have been made in modelling deformation and damage initiation processes on the microscale [9,24]. Typically, simulative approaches to these processes rely on local microstructural data around the considered individual sites of damage initiation or evolution, leading to insights about microstructurally favoured sites for void initiation [26] or plastic deformation [4].

To deliver reliable data about the local stress state during deformation, a calibrated FEM material model is usually applied, in this case with the additional incorporation of a damage criterion. In the field of damage mechanics, two different types of models exist: Coupled and uncoupled models [27]. For coupled models, a damage variable is applied to reduce the yield potential in accordance with the material's softening, induced by ductile damage. A typical example of this kind of model is the Gurson-Tvergaard-Needleman (GTN) model [28–30], which is an example of micromechanical models that can account for physical behaviour of damage evolution by their sets of parameters. Since these parameters are independent, an extensive iteration process is required for their calibration [31]. As a complementary approach, uncoupled models are widely used and describe the material's behaviour without considering softening by ductile damage, like the Bai-Wierzbicki (BW) model [32].

The current study considers all three stages of damage, nucleation-growth-coalescence, and their dependence on stress state at the point of failure. We examine these by high resolution panoramic scanning electron microscopy of tensile specimens which were all deformed to the point of failure but each designed with a different notch geometry as a means to vary equivalent plastic strain and triaxiality. After presenting our data of thousands of damage sites imaged at high resolution in terms of the commonly and therefore easily compared measures, such as void area fraction, we are guided by the following questions:

- Is the quantitative dependence of damage accumulation with strain and triaxiality reproduced at high resolution for a locally strongly heterogeneous material like dual phase steel?
- Is the commonly employed approach of defining a cut-off size to distinguish void nucleation from void growth physical based on the high resolution images of many damage sites?
- Which correlations can be drawn in terms of the closely interlinked effects of plastic strain and stress triaxiality for the initial damage stages of void nucleation and growth?
- And where do developed voids coalesce and might heterogeneity of the material (at the much larger sheet scale) again play a role in this?

2. Experiments and methods

2.1. Tensile testing

In this study, a commercial dual-phase steel of DP800 grade, manufactured by thyssenkrupp AG, was used in the form of sheet metal with a thickness of 1.5 mm. Various geometries of tensile samples, leading to altered stress states in the gauge part, were developed and manufactured using electric discharge machining (EDM). These geometries were used to calibrate the material model to the obtained force-displacement data in order to have good agreement between experiment and FEM-simulations. The geometries of the notched samples are depicted in Fig. 1. They can be divided into two groups: (a) Notched geometry over the sheet thickness (Fig. 1a), used to realise stress states close to plane strain condition and (b) other notched geometries with lateral notches (Fig. 1b). All samples were deformed with the tensile axis parallel to the rolling direction. Additionally, a simple tensile geometry (without a

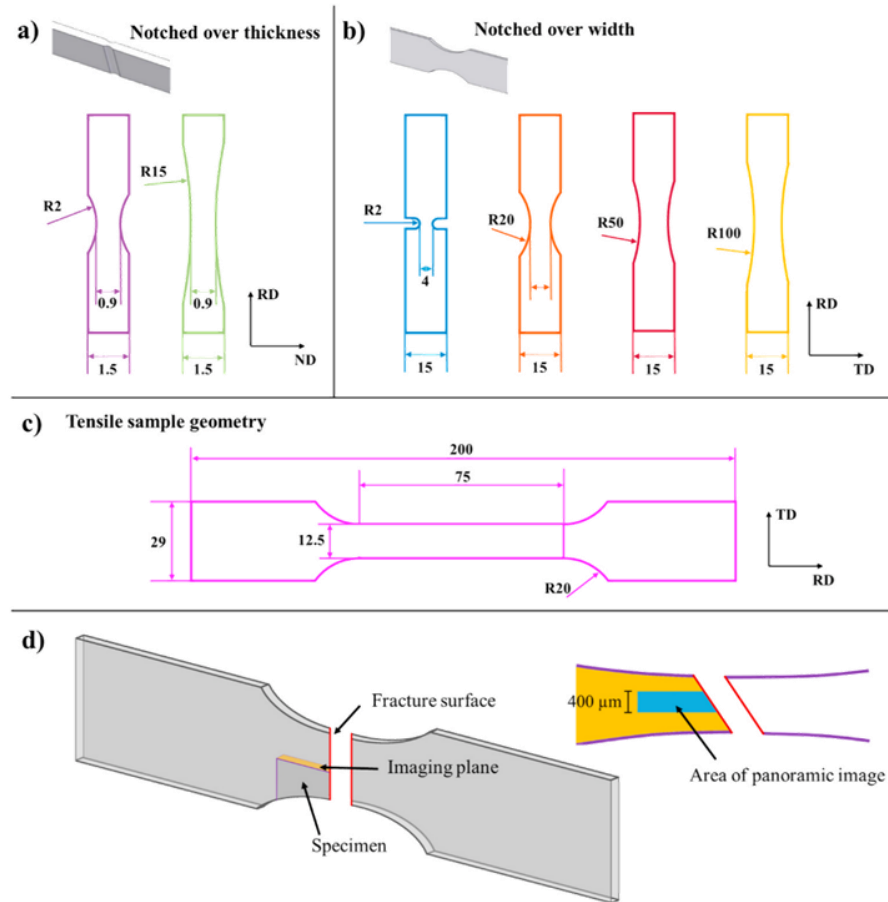


Fig. 1. Tensile geometries used in this study. a) plane-strain geometries notched over the sheet thickness (width 20 mm), b) notched tensile geometries notched over sample width (width 12.5 mm), c) simple tensile geometry without notch. The color-coding for sample geometries is consistent with all following figures. All measurements are given in mm. d) Illustration of specimens cut from tensile samples and area of the evaluated panoramic image. (For interpretation of the references to colour in this figure legend, the reader is referred to the Web version of this article.)

notch) was tested to fit the flow curve of the material (Fig. 1c).

After deformation to fracture at a rate of 0.005 min^{-1} , specimens were cut from the tensile samples as shown in Fig. 1d. The plane marked in yellow was evaluated via SEM panoramic imaging within an area of $400 \mu\text{m}$ width (Fig. 1d). Samples were ground up to 4000 grit, mechanically polished (6, 3, $1 \mu\text{m}$ & colloidal silica suspension (OPS)) and subsequently etched in 1% Nital solution for 5 s. The images were acquired from samples deformed to fracture on a plane perpendicular to the transverse direction. As commercial DP steels often exhibit a banded microstructure, an imaging plane perpendicular to the transverse direction was chosen. In this way, the obtained panoramic images contain multiple bands in favour of several large regions of varying martensite content.

2.2. FE-simulations

This study utilizes the modified BW (MBW) model, specifically the np-MBW-19 version [33]. This version features damage initiation, as well as ductile fracture loci, that specify the material's damage and fracture behaviour for different stress states. Additionally, an indicator is applied to account for non-proportional loading during the deformation of the material. For further information about the applied material model, we refer to previously published studies [31,33,34]. To use the material model in this context, it is important to perform a thorough calibration. Therefore, tensile tests of different geometries were conducted to account for different stress states. Afterwards, simulations were carried out using a VUMAT subroutine, which implemented the

np-MBW-19 model into ABAQUS. The conventional tensile test was used to fit the flow curve of the material, whereas the other tensile tests, described in Fig. 1, were employed to account for the damage initiation and ductile fracture loci. The determined material parameters for the steel used in these investigations were published in an earlier study on damage in dual phase steels [33]. After the calibration process, the FE simulations were able to provide an accurate representation of the local stress state in the sample. Thus, all experimentally tested samples were simulated and their stress triaxiality, as well as plastic equivalent strain were evaluated in the last step before simulated sample fracture. Subsequently, stress triaxiality and plastic strain were extracted at the nodes of the mesh according to the areas, where images were acquired, as described in the previous chapter.

2.3. Void recognition and analysis

The automated void detection and classification approach discussed in Ref. [12] was applied on panoramic SEM images acquired using secondary electron detection (Zeiss LEO 1530 FEG-SEM and FEI Helios NanoLab 600i). All images were taken as individual frames of $100 \mu\text{m}$ horizontal width, corresponding to 3072 pixel (px) with 20% overlap to the next frame. The single images were stitched into panoramic images using a MATLAB-based site recognition and stitching algorithm based on VLFeat toolbox [35].

Voids emerging in micrographs of deformed dual-phase steel samples can have various origins. In particular, they may be distinguished as deformation-induced or not, such as inclusions. In a polished cross-

section, the latter can either be due to particles leaving the surface during metallographic preparation or remaining inclusions appearing black in the SEM micrographs. To detect these sites and exclude them from the obtained statistics of deformation-induced damage, a neural network further described in Ref. [12] was applied. It is noted that the method is able to detect and filter out both types of inclusion-related voids, i.e. those that are still present in the microstructure and others that have fallen out during sample preparation. The accuracy of this procedure is usually larger than 95% [12]. In this method, detection of voids was carried out by a grayscale thresholding and clustering via a DBScan algorithm [36]. Each individual void was then passed over to a convolutional neural network (Inception V3 [37]), that had been trained on manually labelled voids to distinguish deformation-induced voids from voids introduced to the micrographs by inclusions or other artefacts. Deformation-induced voids were processed further via a watershed algorithm, in order to obtain statistical information on individual void area and void shape that can be used for further analysis. The approach is shown schematically in Fig. 2 for an exemplary void in an SEM-panorama.

Void area fractions were obtained using vertical binning along the tensile axis, with every data point representing the area fraction of damage voids in a sample area as wide as the complete panoramic image (400 μm) and 3000 px (97.66 μm) in height. The spacing between the bins was 600 px (19.53 μm).

3. Results

3.1. Morphology of voids

The detected voids on the panoramic micrographs showed voids that can, in analogy to classifications found in the literature, be classified into three main categories:

- (a) Freshly nucleated voids that clearly reveal the underlying mechanism of initiation.
- (b) Voids that have grown with further plastic deformation.

- (c) Significantly larger voids close to the fracture surface, which seem to have originated from the coalescence of several pre-existing, deformation-induced voids.

In addition, inclusions were equally detected as voids, but separated from the deformation-induced voids by the use of the aforementioned neural network.

As seen in Fig. 3, the two main damage mechanisms found in the DP steel used in this study were martensite cracking and the decohesion of martensite/ferrite interfaces. Fig. 3 shows the fundamental stages of damage formation detected in the deformed microstructure, namely initiation (a + b), void growth (c + d) and coalescence (e). All voids are expected to undergo these three stages of void evolution irrespective of initiation mechanism, i.e. martensite cracking (a + c) or martensite/ferrite interface decohesion (b + d). In addition to the deformation induced voids, typical inclusions are depicted in Fig. 3 (f + g), which were detected by the neural network and not processed further.

3.2. Influence of stress state on void area fraction

The samples utilized for this study were designed to cover a wide range of stress states from uniaxial tensile stress to plane strain conditions. For the FE simulations of the uniaxial loading the samples were exposed to, the measured displacement was used to simulate the local stress and strain conditions during deformation up to the point of sample fracture in the experiment. Stress triaxiality and strain were found to monotonically increase over the process of deformation, so that the highest value for these quantities and the value at the point of sample failure coincided. Therefore, the last timestep at sample fracture was used for evaluating the stress and strain state in order to correlate with the microstructural damage measurements. All considered points per sample are spatially distributed along the tensile axis in the middle of the sampled area, as shown in Fig. 4.

As visible in Fig. 4, the covered window in stress triaxiality and plastic equivalent strain ranges from 0.37 to 0.71 in triaxiality and 0.05 to 0.55 in plastic strain. Only positive values for triaxiality were considered, as the most common models of void growth only apply to these values. For higher stress triaxiality values, the plastic strain at

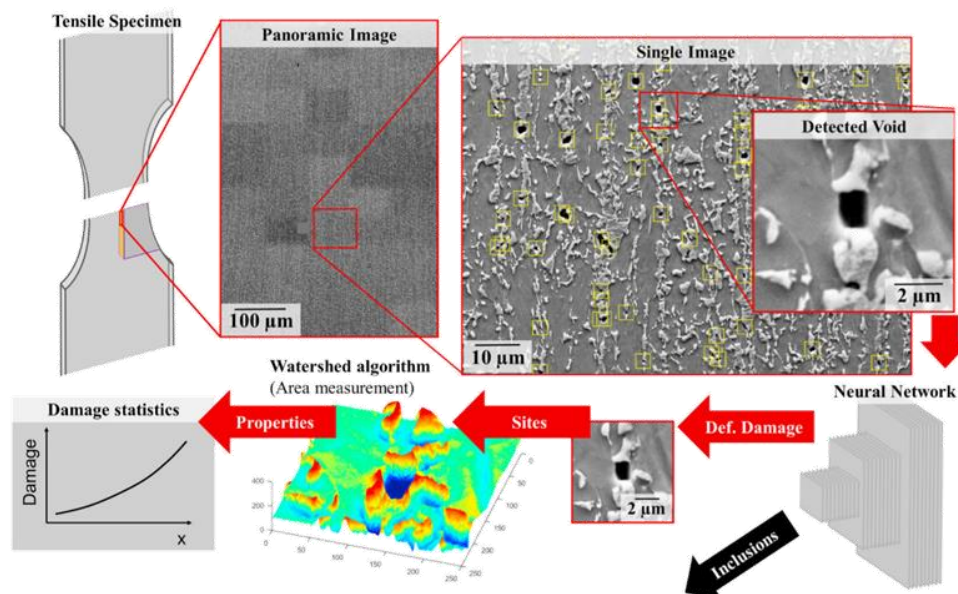


Fig. 2. Experimental concept of automated void detection and classification in panoramic SEM images using a neural network to distinguish deformation-induced voids from inclusions.

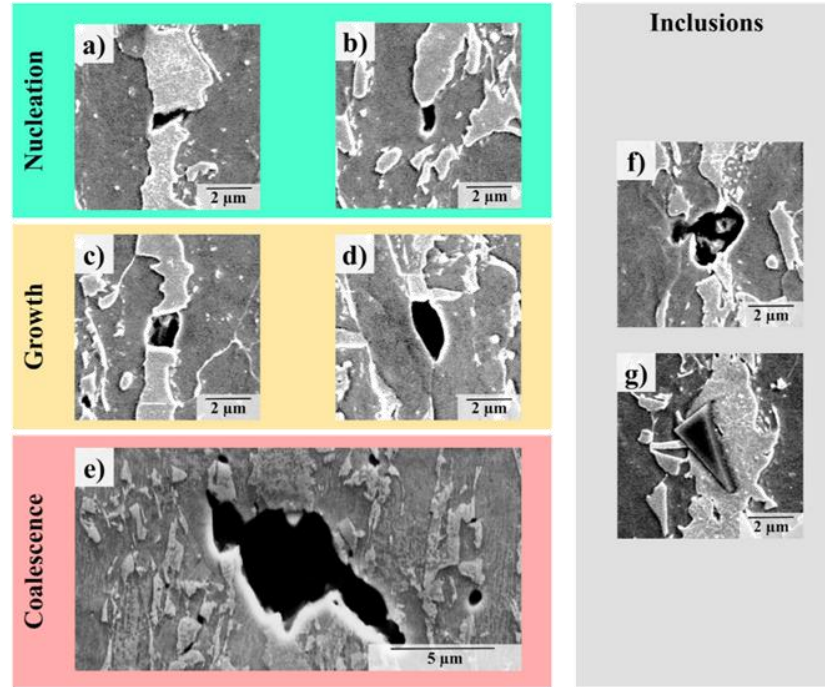


Fig. 3. Classification of observed microstructural voids in deformed samples. a) martensite cracking, b) decohesion of M/F interface, c) grown martensite crack, d) grown interface decohesion site, e) coalescence of voids close to fracture surface, f) site of inclusion fallen out of the sample surface during preparation classified by neural network, g) inclusion (likely TiN) in a martensite island classified by neural network.

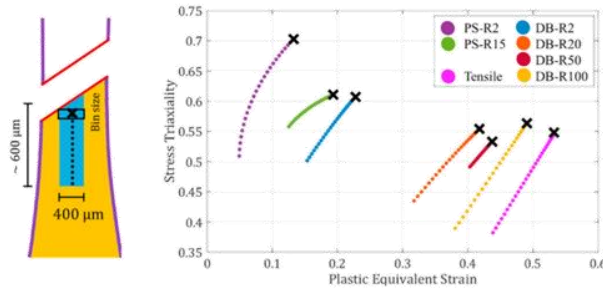


Fig. 4. FE simulations of triaxiality-strain data for the investigated tensile samples at a timestep coinciding with sample fracture. Each data point represents one measured and evaluated rectangular bin from the area segment in the SEM (blue sample area, bin indicated by thin black line). The cross points in the diagram corresponds to the cross point position marked on the sample directly below the fracture surface. (For interpretation of the references to colour in this figure legend, the reader is referred to the Web version of this article.)

fracture was lower. The standard deviation of absolute von Mises equivalent stresses calculated by FEM over the region of the evaluated panoramic images range from 0.3% to 4.9% of the maximum stress value, so that along the whole evaluated areas consistently high stress levels are reached, making a correlation of triaxiality to damage feasible in all these regions.

Area fractions of detected deformation-induced voids along the tensile axis of the samples were calculated for up to 600 μm from the centre of the fracture surface with respect to the tensile axis as illustrated in Fig. 4. As the spatial evaluation points in the FE simulation and the panoramic image were not the same, a polynomial interpolation was used on the FE data to approximate values for the exact locations of the evaluated bins in the panoramic image and obtain an identical spatial

grid for evaluation. The values obtained this way for the global damage variable of void area fraction were compared with the plastic equivalent strain for the same point in the sample. The results are shown in Fig. 5.

The data reveals a global trend of increasing void area fraction with increasing strain. However, further examination of the data reveals additional insights: (i) Damage formation is found to increase at different rates for the different stress and strain states investigated. (ii) The overall range of strains varies strongly with the different sample geometries investigated. (iii) Even though all samples were measured at the point of maximum deformation at fracture, the values of final void area fraction are different.

The imposed stress and strain state through the altered sample geometry was investigated further to elucidate the influence of stress triaxiality on the measured void area fraction (Fig. 6). A comparison

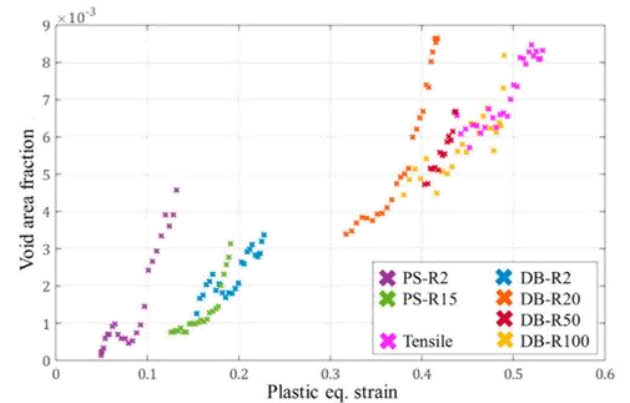


Fig. 5. Measured area fraction of voids vs. estimated plastic equivalent strain from FE simulation.

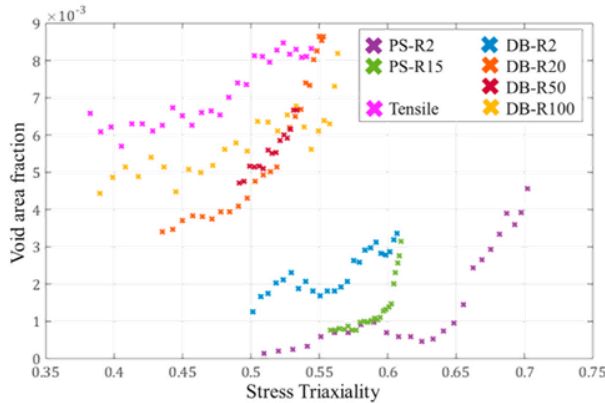


Fig. 6. Measured area fraction of voids vs. estimated stress triaxiality from FE simulations.

across all the cases reveals that large void area fractions populate the upper-left corner of the plot associated with lower triaxiality and lower void area fractions are associated with the higher values of stress triaxiality. However, when considering each tensile geometry individually, an increasing void area fraction with increasing triaxiality is apparent.

3.3. Influence of plastic strain and stress triaxiality on void size distribution

While the statistics gathered from the large-scale observations yield a clear and distinct picture regarding the influence of stress triaxiality and plastic strain, all presented data to this point refers to the cumulative property of void area fraction. To gain more insights into the stages and mechanisms of void formation, information about every single of the ten thousands of detected and measured damage sites was evaluated. This enables us to also consider void size distributions in addition to area fractions or number of sites as shown in Fig. 7, while noting that again

stress triaxiality and plastic equivalent strain are of course interdependent as shown in Fig. 4.

However, trends are visible in this data: While the number of voids emerging in the microstructure increases with the calculated plastic strain, the opposite trend is seen in Fig. 7c for the median void size. For the first, an exponential fit is also shown as this is the distribution found in previous work on the same material for the number of voids per area as a function of uniaxial strain [12]. A relationship more adequately described as a linear increase can be found between stress triaxiality and the median void size (Fig. 7d), whereas in Fig. 7b the number of damage sites dropped with increasing triaxiality.

Note that the values of correlations made in Fig. 7 b and c are not to be considered physical, but the purpose of these plots is to clarify that while the increases visible in Fig. 7a and d are seen in the presence of the convolution of strain and triaxiality, these are not repeated for the inverted correlations.

For these data points shown in Fig. 7, all values from the FE simulations were obtained as an average of the evaluated area, thus the area of the panoramic image was evaluated as a single bin to obtain one integral value of stress triaxiality and equivalent plastic strain per sample geometry. The deviation from this mean across the evaluated area is given explicitly in Fig. 4 and indicated for the reader in terms of the standard deviation around the mean in Fig. 7.

Even though different strains lead to rupture of the sample, as seen in Fig. 4, and growth of voids is more pronounced in sample geometries with lower fracture elongations and therefore high triaxialities, it is noted that the levels of damage at the point of sample failure are by no means equal, as seen in Fig. 6. This material failure, however, is caused by the third stage in the process of void evolution, the coalescence of voids. This has been investigated using the large-scale images of the deformed microstructure close to the fracture surface.

3.4. Influence of localised shear on the coalescence of damage

Void coalescence is the final stage of damage formation before failure occurs. From the obtained panoramic SEM images, statistical information regarding the location, size and morphology of voids have been collected in order to study the spatial patterns of void coalescence.

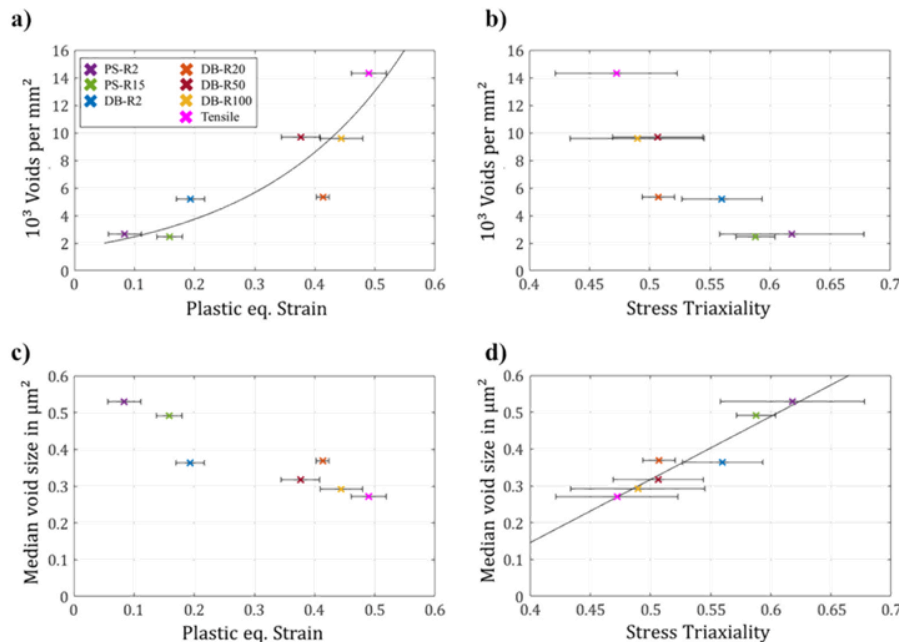


Fig. 7. Number and size of voids as a function of strain and triaxiality. a) Plastic equivalent strain and number of deformation-induced damage sites per area, b) stress triaxiality and number of detected damage-induced voids per area. c) plastic equivalent strain and median void size, d) stress triaxiality and median void size. The correlations in a) and d) have been fitted with the commonly assumed for using an exponential (a) and a linear (d) fit. The plastic equivalent strain and stress triaxiality are shown as the mean over the evaluated area. The deviation for each sample from the plotted mean value and their interdependency is shown in Fig. 4 and indicated here by horizontal bars that measure two standard deviations in width.

This was done to elucidate whether they depend on the interaction of local deformation with existing voids. By focusing on the shape of the voids, especially their angle towards the tensile axis, it was found that large voids, having originated from multiple initiated voids by coalescence, are often oriented just under 45° to the tensile axis as shown in Fig. 8.

Whether these voids have entered the stage of void coalescence was determined by regarding the adjacent martensite islands: a grown void is thought to typically still lie in between or at the interface of a single martensite island, while void coalescence is understood as the joining of voids originating from more than one interface/martensite island. For these voids, orientation angles just below 45° to the tensile axis could predominantly be observed. Furthermore, the large area observations have yielded additional information about the patterns of voids: The detected, angled voids tend to form along straight lines with the inclination of the voids along “coalescence bands”. Fig. 8b shows an example of primary coalescence, initially joining voids together. This is typically found in the widest martensite bands. Adjacent to these sites, along the slope of the inclination angle of the resulting coalescence site, the microstructure appeared to be sheared by slip bands, which promotes additional coalescence of pre-existing voids, leading to multiple coalescence sites along the shear bands as shown in Fig. 8c) and finally, secondary coalescence of those, as depicted in Fig. 8d.

4. Discussion

The three stages of void formation in a highly heterogeneous dual phase steel microstructure were investigated in a statistical way using automated imaging, void recognition and deep-learning based analysis. In this way, this study enabled us to gather a large amount of data from >10,000 voids in order to investigate the void formation behaviour in these complex microstructures and correlate the findings to simulations of the stress and strain state in the deformed samples. We will discuss these here starting with the global picture of median void size and area fraction before considering their distribution in more detail.

4.1. Quantitative dependence of global damage accumulation on strain and triaxiality

The data in Fig. 5 shows a consistent influence of the applied strain on damage evolution with the void area fraction increasing with strain. In contrast, the impact of stress state (triaxiality) is less obvious from the data in Fig. 6. Here, we observe (i) for each sample an increase in void area fraction with stress triaxiality, however, globally we find (ii) lower void area fractions with increasing triaxiality. The first case, considering each sample individually, is in agreement with the analyses by Lemaitre, Gurson and McClintock [21,38,39]. The observed inconsistency

between the findings for each single specimen and the global trend then needs to be considered in more detail.

As the correlations in Figs. 5 and 6 implicitly contain the relationship between strain and triaxiality values for the examined specimens (Fig. 4), the dependences of void area fraction on the plastic strain and stress triaxiality are better considered simultaneously (Fig. 9) to avoid overlooking correlations intrinsic to the chosen samples between these values. For each sample geometry and therefore curve, different levels of plastic equivalent strain are present, but an increase in void area fraction is nevertheless visible for both parameters, strain and triaxiality. For an easier observation of the trends depicted in Fig. 9, the graph shows a surface fit based on the data points.

We do note, however, that triaxiality is calculated as the ratio of the hydrostatic stress and the von Mises equivalent stress and is therefore in itself only a measure of how dominant the hydrostatic stresses are in the applied stress state. The triaxiality does not, however, take the overall magnitude of the applied stress into account. The comparability of the evaluated samples is given in terms of the point of failure to which each was tested. Therefore, all samples have covered their whole range of ductility for their respective geometry. In the FEM-simulations, this was ensured by applying a criterion for fracture in terms of a ductile fracture locus [33][], which all samples reached at the timestep of evaluation. While a locally altered stress state due to necking is taken into account in the simulations through the use of a Hollomon-Voce-approach of calibration [33][], the end geometries achieved by experiments and simulations have been visually compared and considered equivalent, so that the obtained values for stress and strain are plausible, even in the regions very close to the fracture surface, while over the whole area of the images, the absolute stress levels show only minor variations. If void area fractions were additionally to be considered for samples before fracture or far away from the fracture surfaces, the results might therefore differ if only strain and triaxiality were to be compared. In such a case, the use of the hydrostatic stress magnitude may be more accurate when comparing samples of varying states of deformation.

In principle, our observations therefore confirm the expected evolution of void density and area with respect to plastic equivalent strain and stress triaxiality in a material that shows a high internal mechanical contrast between the two constituent phases and also inhomogeneity (martensite bands) across its thickness. Previously, this trend had also been confirmed by others [7,14,40] using large area or volume measurements, but normally at a lower spatial resolution.

The classical expectation [21] is to not only find an increase in cumulative damage quantity with triaxiality, but in particular growth of voids. To achieve this correlation, the influences of strain and stress triaxiality have to be separated and discussed concerning other measured quantities of the void ensembles, rather than discussing area fraction as a cumulative property.

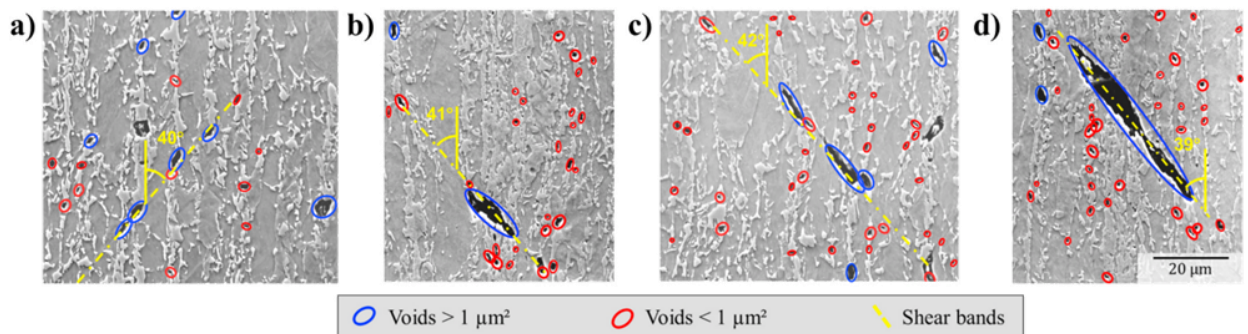


Fig. 8. Extracted regions of interest from panoramic images showing various stages of void coalescence. a) the initial formation of elongated voids along a shear band, b) the coalescence of voids, forming one large void in a largely martensitic region and c) regions of average phase distribution. d) the formation of an even larger void near the sample surface through further void coalescence.

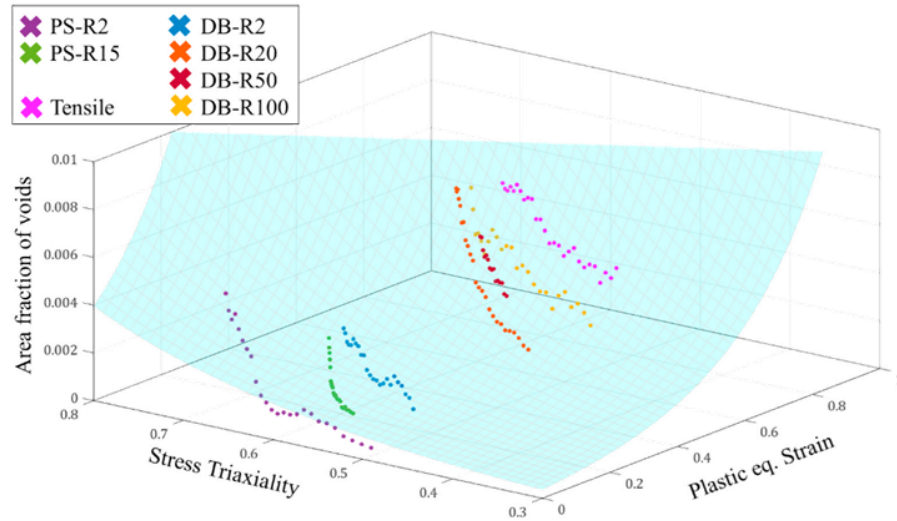


Fig. 9. Evolution of void area fraction as a function of stress triaxiality and plastic equivalent strains from FE-simulations. The blue area represents a double exponential surface fit of the data points. (For interpretation of the references to colour in this figure legend, the reader is referred to the Web version of this article.)

4.2. Separation of the stages of void evolution for individual voids

It is perhaps not surprising that, once voids have reached a size that encompasses several instances of each of the phases of the dual phase steel, the behaviour of homogeneous model materials is reproduced. Here, we therefore set out to investigate whether this behaviour is in fact observed at the smallest observable scale as well, where voids contained entirely inside a martensite island or ferrite grain can be resolved. This implies that we need to follow previous attempts to distinguish between those damage sites which have been freshly nucleated at a single interface, grain boundary or as a crack across a martensite island and those which have already grown significantly.

For this, a threshold-based criterion using a fixed threshold has been proposed for SEM-based methods and for the purpose of parameter fitting in a GTN-type model by Ref. [7,23]. Establishing a lower bound threshold for grown voids then requires a statistical approach to damage, which is possible based on SEM data or X-ray microtomography [41]. A main difference between methods then lies in the expected resolution and therefore also the length scale of possible thresholds. For 3D-synchrotron observations, Landron et al. [42] determine that with a voxel size of as low as 100 nm, a significant effect of voids with a diameter smaller than 4 μm is observed. In contrast, the 2-dimensional pixel size using SEM is much smaller, e.g. 32 nm in this study, and voids as small as 0.02 μm^2 can therefore be detected and considered. Avramovic-Cingara et al. [40] used a threshold of 1 μm in diameter to distinguish between nucleated and grown damage sites.

However, a comparison of our measurements of detected voids with respect to their size in different stages of their development show that these threshold-based criteria prove challenging to set up in a physically meaningful way.

The size distribution of voids imaged and analysed across all samples in this study is shown in Fig. 10 along with several micrographs showing all three stages of damage color-coded as (close to) nucleation (green), individual void growth (yellow) and coalescence (red). A direct comparison may be drawn with the threshold of 1 μm suggested by Avramovic-Cingara et al. [40] for micrographs of similar resolution on DP600. In their work, the authors found an average aspect ratio of 2, giving an equivalent area threshold of the order of 0.5 μm^2 . A comparison with the void size distribution in Fig. 10 shows that in our material, the majority of damage sites is in fact smaller and therefore below this threshold.

Fig. 10 a and b include voids close to nucleation that are associated with the smallest measured areas for martensite cracking (a) and interface decohesion (b). As interface decohesion may be more easily pictured as a rather continuous process once a void has nucleated, the remaining voids selected for Fig. 10 are martensite cracks, starting and ending at the surfaces of a martensite island. Owing to this geometry, it is possible to determine both the initial crack length, given by the length of the visible crack surface for a through-thickness crack of the martensite island, and the displacement during void growth, given by the distance between the crack surfaces. The displayed voids highlight the independence of the state of void evolution on a void's area: A similar void area can be formed in a crack with a large crack length but small crack opening or a short crack showing extensive growth. For example, in comparison of Fig. 10e and h a crack opening larger by a factor of nearly 7 in (h) compared with (e) still results in a smaller void area. This can easily be understood by comparing the width of the cracked martensite islands that measure 3320 nm (e) compared with 800 nm (h). Similar examples are given in Fig. 10 with two voids of 0.30 μm^2 (c and f) and around 0.50 μm^2 (d and g). Each pair possesses very similar areas but, when analysed individually with respect to their width, displacement and surrounding microstructure, show different stages of evolution. In the case of (a) the small area is due to both a small crack opening and the small lateral extension of the martensite island. The entered stage of void evolution therefore cannot be determined by comparatively simple measurements of void area or aspect ratio alone. For martensite cracks, further factors may help in a better discrimination, including crack opening distance, orientation to the main stress axis or relation to the size and shape of the original martensite island. In the case of interface decohesion, a more continuous process may be envisaged once a void has formed and a physical threshold for the first decohesion process may be underneath that resolved routinely by SEM.

In any case, a statistical evaluation of the different stages of damage formation with a clear separation of the stages will require correlation of damage mechanism, surrounding microstructure and geometric parameters for every given void and a clear working definition of where nucleation has completed and void growth begins. Once significant growth has taken place, detection and determination of geometric parameters of the void become easier, but conversely, the identification of a single underlying or damage mechanism or origin of the void in terms of a nucleation mechanism become much more difficult to achieve. This is true both for a manual analysis as mechanisms begin to interact and

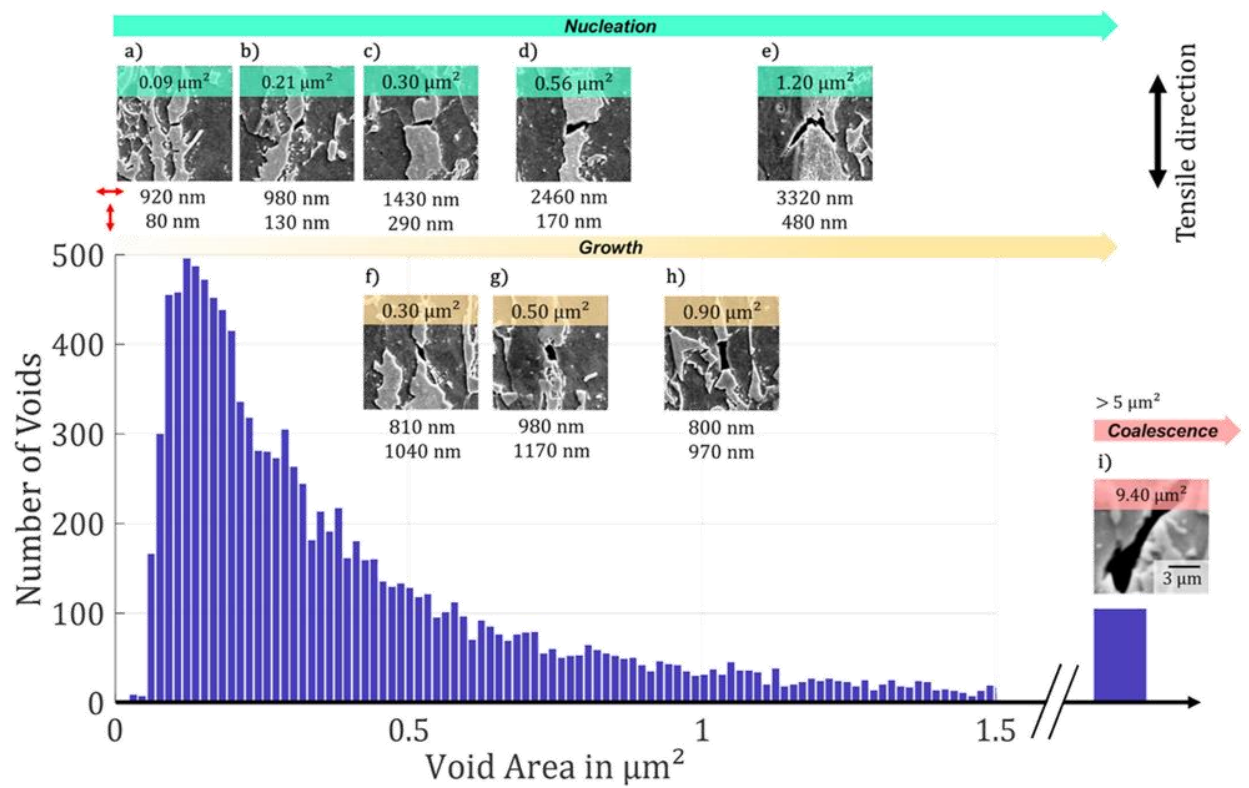


Fig. 10. Void size distribution of all detected voids (12,730 sites total), voids larger than 5 μm^2 marked with a single bar and corresponding example of a void coalescence site. a)-i) Examples of voids showing various stages of nucleation, growth and coalescence. Measured values are given as the void width and length of growth in tensile direction.

origins become obscured and as a result also for automated analyses based on artificial intelligence that rely on the first manual analysis for their training [12].

In summary of the above, nucleation of new voids in the sense of an increase in void number and growth in terms of an overall increase in void area correspond well with those expected based on classical models, even for the strongly heterogeneous dual phase microstructure. However, a clear identification and physical interpretation of nucleation and growth stages for a large number of individual voids will require further progress in high resolution damage characterisation and automated analysis of large image datasets.

4.3. Correlation of void size statistics with strain and triaxiality

While a separation of the stages of damage evolution may not yet be possible for individual voids, a more in-depth view into the quantitative values of global void area fraction, discussed above, is nevertheless available based on the single void data obtained here.

Strain partitioning is accepted to be the main cause of void nucleation in dual phase steels [26,43,44], and hence the overall number of detected voids is expected to increase with strain, as shown for samples tested in tension by various researchers [12,23,45]. Correspondingly, the automated void detection applied in this study found an increase in the void number density with strain that is consistent with an exponential increase (Fig. 7a). In terms of growth, the expectation of a pronounced increase in void size also manifests in the data shown in Fig. 7b: the median void size increases linearly to about twice the original value across a triaxiality range of 0.47–0.62. At the same time, this increase is associated with decreasing plastic strains at the point of area measurements due to the inverse relationship between triaxiality and plastic equivalent strain at failure (Fig. 4). This then results in the decreasing median void size with plastic equivalent strain displayed in Fig. 7c. The correlation between triaxiality and void number remains dominated by the decreasing strain with increasing triaxiality, and therefore suggests no measurable influence of triaxiality on void nucleation. As plastic deformation is dominated by shear and normal, rather than hydrostatic stress components, this corresponds to the expectations in a void-free material. However, micromechanical void initiation and growth processes in a complex, heterogeneous microstructure are governed by local stress and strain partitioning, and therefore microstructural processes, such as dislocation motion and accumulation [7,17]. For this reason, attempts to trace back the growth of voids to the overall applied stress

state have predominately focussed on homogeneous model materials [15]. Here, the obtained statistics from a multitude of automatically detected damage events enable us to come to similar conclusions in a real and strongly heterogeneous microstructure. While predicting the initiation and evolution of voids at a specific location requires detailed information about the microstructural stress state and constituents, our results show that, applied to a large area, the statistics about void numbers and sizes converge against the expectations based on the commonly used theoretical models for the local continuum stress state obtained by FEM.

The presented approach for quantifying microscale damage by means of automated void detection and classification [12] will therefore enable further development of damage models by making more detailed void size and damage mechanism data available for their calibration. This is particularly true for strongly heterogeneous microstructures, for which it is often simply assumed that the classical models formulated based on homogeneous model materials can be directly applied. For the case of DP800 steel, we have shown here that this is in fact the case, but in the same way, the presented approach could now also be easily transferred to many other materials to confirm assumptions about the effect, or its absence, of local strain partitioning on global damage evolution.

4.4. Void coalescence

In addition to the two stages discussed above, void nucleation and growth of individual voids, the last stage of damage evolution remains to be considered, in which a transition from single void growth to their coalescence takes place. It is this stage that is ultimately likely to govern failure of a sample or component by more localised mechanisms, for example by shear banding in ferrite which causes distortion and joining of voids that were originally oriented with an inclination towards the tensile direction. Using the large-scale micrographs acquired here, the occurrence of void coalescence events could also be studied. In the observed pattern of large voids, we find that the process of void coalescence is connected directly to shear instabilities. It is the panoramic views and large number of coalesced voids (100 voids larger than $5 \mu\text{m}^2$ over all samples) that allowed us here to trace the coalescence sites back to the existence of shear instabilities that are best visible at larger scales and show that multiple sites of void coalescence align along these bands of locally altered stress state.

Thus, having studied all three stages of void formation in the dual-

<i>Simulation</i>	<i>Experiment</i>		<i>Initiation</i> ■	<i>Growth</i> ■	<i>Coalescence</i> ■■
Deformation mechanisms	SEM, nanoCT	<i>Individual</i>	Local Microstructure 	Local Microstructure 	Local void ensemble
Models informed across scales	Perspective: Panoramic SEM + Automated single void analyses		Plastic Strain 	Stress Triaxiality 	Shear instabilities
Continuum / global statistics	Light micr., μCT	<i>Global</i>			

Fig. 11. Schematic representation of the identified main causes for the three stages of damage evolution, both for the local evolution of a single void and for the global evolution of damage as an ensemble of voids. Panoramic high resolution micrographs and progress in automated single void damage analysis will improve our understanding of damage evolution and allow formulation and calibration of advanced models for damage simulation from the single phase to the sheet or component scale.

phase steel microstructure globally on the obtained large-scale micrographs each stage of damage evolution can be connected with dominant parameters, many of which consistent with expectations from homogeneous model materials (Fig. 11). For a single void, the mechanisms that lead to void initiation and growth are strongly dominated by the local microstructure and morphology. However, when regarding all microstructural sites in a statistical way, including large areas and therefore whole ensembles of thousands of voids, the microstructure-independent continuum stress state alone proves sufficient to obtain numbers converging against the expectations for void initiation and foremost, growth in an isotropic material as proposed and shown in Ref. [15]. While every single void is locally dominated by its surroundings, the global connection between triaxiality and void growth remains intact. The subsequent stage of void coalescence, can again only occur where the local boundary conditions in the vicinity of a single void are fulfilled, i.e. a shear instability driving substantial deformation across a larger, if narrow, area and the proximity to several other voids within local void ensembles allowing direct coalescence.

We have shown here how the typical sequence of void nucleation, growth and coalescence can be imaged and interpreted at all relevant length scales above the individual site of damage nucleation that typically requires advanced imaging and local adjustment of imaging conditions, e.g. for electron channelling contrast imaging of the underlying martensite substructures and dislocations inside the ferrite [46,47]. Together with the mechanistic understanding of damage initiation from the atomic scale of alloying and single phase or interface plasticity or decohesion, the quantitative as well as mechanistic understanding of damage evolution is directly relevant to formulating new models and informing existing simulation approaches with reliable data for calibration and validation of critical assumptions in the underlying damage models. Ultimately, it is the physical understanding across all length-scales that will allow us to formulate reliable damage models to guide microstructure and process design towards better material and component performance in terms of (light) weight, safety and cost or environmental impact. Having the right experimental methods at hand that allow the development and confident use of models and simulations is therefore an essential step in achieving this goal and connecting the scales of physical mechanisms and engineering design or industrial materials processing.

5. Conclusions

We studied the influence of strain and triaxiality on the fundamental stages of deformation-induced void evolution (damage) by automated void detection and measurements on large-scale, high-resolution SEM images of differently notched tensile samples deformed to failure. While this approach globally confirmed the expected dependencies of void nucleation, growth and coalescence on strain and stress triaxiality, the multitude of observed and measured voids in our statistical approach highlighted the fact that an individual division of microstructural voids into clear, separate categories of the stages of damage evolution are not yet feasible. In detail, we conclude:

- The measured level of damage varies along with the critical amount of damage at the point of sample fracture: Higher values for triaxiality lead to a lower tolerance for damage at similar strains.
- While the evolution in terms of nucleation and initial growth of a single void is determined by the local stress state in the surrounding heterogeneous microstructure of DP800 steel, damage evolution across all voids converges against the expectations for the applied macroscopic stress state
- Globally, the applied plastic strain exerts a major influence on the overall number, and therefore the nucleation of new voids, while triaxiality correlates with the median void size and is then in turn related to the extent of void growth.

- Void coalescence in the large-scale images was detected predominantly along shear bands that introduce severe, local plasticity and allow voids to merge in areas of high void density, in particular martensite bands.
- In spite of the acquisition of high resolution data across a large area and use of recently developed first deep learning tools for automated mechanism analysis, a physical distinction of nucleation and growth remains elusive.
- No basis for the use of threshold void dimensions could be found to distinguish void nucleation and growth.

For a separation of these stages, a clear and physical definition of the onset of growth as well as a concurrent and automated analysis of mechanisms and geometry at all stages of void evolution will have to be achieved.

Data availability statement

The raw/processed data required to reproduce these findings cannot be shared at this time as the data also forms part of an ongoing study.

CRediT authorship contribution statement

Carl F. Kusche: Investigation, Data curation, Writing - original draft, Writing - review & editing. **Felix Pütz:** Investigation, Data curation, Writing - original draft, Writing - review & editing. **Sebastian Münstermann:** Conceptualization, Supervision, Project administration, Funding acquisition, Writing - review & editing. **Talal Al-Samman:** Conceptualization, Supervision, Project administration, Funding acquisition, Writing - review & editing. **Sandra Korte-Kerzel:** Conceptualization, Supervision, Project administration, Funding acquisition, Writing - review & editing.

Declaration of competing interest

The authors declare that they have no known competing financial interests or personal relationships that could have appeared to influence the work reported in this paper.

Acknowledgments

The investigations are kindly supported by the German Research Foundation in context of the Collaborative Research Centre CRC/Transregio 188 “Damage-Controlled forming processes”, projects B02 and B05, project number 278868966.

References

- [1] W. Bleck, S. Papaefthymiou, A. Frehn, Microstructure and tensile properties in dual phase and trip steels, *Steel Res. Int.* 75 (11) (2004) 704–710.
- [2] J. Zhang, H. Di, Y. Deng, R.D.K. Misra, Effect of martensite morphology and volume fraction on strain hardening and fracture behavior of martensite–ferrite dual phase steel, *Mater. Sci. Eng.* 627 (2015) 230–240.
- [3] J.K.L.S. Joo, J. Koo, S. Lee, D. Suh, H.S. Kim, Method for measuring nanoscale local strain in a dual phase steel using digital image correlation with nanodot patterns, *Scripta Mater.* 68 (2013) 245–248.
- [4] H. Ghadbeigi, C. Pinna, S. Celotto, J.R. Yates, Local plastic strain evolution in a high strength dual-phase steel, *Mater. Sci. Eng.* 527 (2010) 5023–5032.
- [5] O.B.E. Maire, M. Di Michiel, C. Verdu, Initiation and growth of damage in a dual-phase steel observed by X-ray microtomography, *Acta Mater.* 56 (2008) 4954–4964.
- [6] M. Calcagnotto, Y. Adachi, D. Ponge, D. Raabe, Deformation and fracture mechanisms in fine- and ultrafine-grained ferrite/martensite dual-phase steels and the effect of aging, *Acta Mater.* 59 (2011) 658–670.
- [7] G. Avramovic-Cingara, Y. Ososkov, M.K. Jain, D.S. Wilkinson, Effect of martensite distribution on damage behaviour in DP600 dual phase steels, *Mater. Sci. Eng.* 516 (2009) 7–16.
- [8] D. Kim, W. Kim, J. Han, W. Woo, S. Choi, Effect of microstructural factors on void formation by ferrite/martensite interface decohesion in DP980 steel under uniaxial tension, *Int. J. Plast.* 94 (2017) 3–23.

Publication #2: On the effect of strain and triaxiality on void evolution in a heterogeneous microstructure – A statistical and single void study of damage in DP800

C.F. Kusche et al.

Materials Science & Engineering A 799 (2021) 140332

- [9] T.W.J. de Geus, F. Maresca, R.H.J. Peerlings, M.G.D. Geers, Microscopic plasticity and damage in two-phase steels: on the competing role of crystallography and phase contrast, *Mech. Mater.* 101 (2016) 147–159.
- [10] O.B.C. Landron, E. Maire, J. Adrien, Characterization and modeling of void nucleation by interface decohesion in dual phase steels, *Scripta Mater.* 63 (2010), 973–976.
- [11] J.P.M. Hoefnagels, C.C. Tasan, F. Maresca, F.J. Peters, V.G. Kouznetsova, Retardation of plastic instability via damage-enabled microstrain delocalization, *J. Mater. Sci.* 50 (2015) 6882–6897.
- [12] C. Kusche, T. Reclik, M. Freund, T. Al-Samman, U. Kerzel, S. Korte-Kerzel, Large-area, high-resolution characterisation and classification of damage mechanisms in dual-phase steel using deep learning, *PloS One* 14 (5) (2019), e0216493.
- [13] C.C. Tasan, J.P.M. Hoefnagels, E.C.A. Dekkers, M.G.D. Geers, Multi-axial deformation setup for microscopic testing of sheet metal to fracture, *Exp. Mech.* 52 (2012) 669–678.
- [14] B. Revil-Baudard, O. Cazacu, S. Thuillier, E. Maire, Effect of stress triaxiality on porosity evolution in notched bars: quantitative agreement between a recent dilatational model and X-ray tomography data, *Mech. Res. Commun.* 50 (2013) 77–82.
- [15] A. Hosokawa, D.S. Wilkinson, J. Kang, E. Maire, Effect of triaxiality on void growth and coalescence in model materials investigated by X-ray tomography, *Acta Mater.* 60 (6–7) (2012) 2829–2839.
- [16] C.C. Tasan, M. Diehl, D. Yan, C. Zambaldi, P. Shanthraj, F. Roters, D. Raabe, Integrated experimental-simulation analysis of stress and strain partitioning in multiphase alloys, *Acta Mater.* 81 (2014) 386–400.
- [17] M. Calcagnotto, D. Ponge, E. Demir, D. Raabe, Orientation gradients and geometrically necessary dislocations in ultrafine grained dual-phase steels studied by 2D and 3D EBSD, *Mater. Sci. Eng.* 527 (2010) 2738–2746.
- [18] T.W.J. de Geus, J.E.P. van Duuren, R.H.J. Peerlings, M.G.D. Geers, Fracture initiation in multi-phase materials: a statistical characterization of microstructural damage sites, *Mater. Sci. Eng.* 673 (2016) 551–556.
- [19] S.M. Azimi, D. Britz, M. Engstler, M. Fritz, F. Mücklich, Advanced steel microstructural classification by deep learning methods, *Sci. Rep.* 8 (2128) (2018).
- [20] A.S.A. Ramanani, A. Aretz, U. Prah, W. Bleck, Characterization and modelling of failure initiation in DP Steel, *Comput. Mater. Sci.* 75 (2013) 35–44.
- [21] A.L. Gurson, Continuum theory of ductile rupture by void nucleation and growth: part I—yield criteria and flow rules for porous ductile media, *J. Eng. Mater. Technol.* 99 (1) (1977) 2–15.
- [22] R. Meys, C.F. Kusche, C. Löhbe, T. Al-Samman, S. Korte-Kerzel, A.E. Tekkaya, Global and high-resolution damage quantification in dual-phase steel bending samples with varying stress states, *Metals* 9 (3) (2019) 319.
- [23] G.G.K. Isik, T. Clausmeyer, F. Nürnberger, A.E. Tekkaya, H.J. Maier, Evaluation of void nucleation and development during plastic deformation of dual-phase steel DP600, *Steel Res. Int.* 87 (9) (2016) 1–9.
- [24] J. Kadkhodapour, A. Butz, S. Ziaei-Rad, S. Schmauder, A micro mechanical study on failure initiation of dual phase steels under tension using single crystal plasticity model, *Int. J. Plast.* 27 (2011) 1103–1125.
- [25] T.W.J. de Geus, R.H.J. Peerlings, M.G.D. Geers, Competing damage mechanisms in a two-phase microstructure: how microstructure and loading conditions determine the onset of fracture, *Int. J. Solid Struct.* 97–98 (2016) 687–698.
- [26] C.C. Tasan, J.P.M. Hoefnagels, M. Diehl, D. Yan, F. Roters, D. Raabe, Strain localization and damage in dual phase steels investigated by coupled in-situ deformation experiments and crystal plasticity simulations, *Int. J. Plast.* 63 (2014) 198–210.
- [27] J. Besson, Continuum models of ductile fracture: a review, *Int. J. Damage Mech.* 19 (1) (2010) 3–52.
- [28] A.L. Gurson, Continuum theory of ductile rupture by void nucleation and growth: part I—yield criteria and flow rules for porous ductile media, 1977.
- [29] V. Tvergaard, Influence of voids on shear band instabilities under plane strain conditions, *Int. J. Fract.* 17 (4) (1981) 389–407.
- [30] A. Needleman, V. Tvergaard, An analysis of ductile rupture in notched bars, *J. Mech. Phys. Solid.* 32 (6) (1984) 461–490.
- [31] O. West, J. Lian, S. Münstermann, W. Bleck, Numerical determination of the damage parameters of a dual-phase sheet steel, *ISIJ Int.* 52 (4) (2012) 743–752.
- [32] Y. Bai, T. Wierzbicki, A new model of metal plasticity and fracture with pressure and Lode dependence, *Int. J. Plast.* 24 (6) (2008) 1071–1096.
- [33] F. Pütz, F. Shen, M. Könemann, S. Münstermann, The differences of damage initiation and accumulation of DP steels: a numerical and experimental analysis, *Int. J. Fract.* (2020).
- [34] B. Wu, X. Li, Y. Di, V. Brinnel, J. Lian, S. Münstermann, Extension of the modified Bai-Wierzbicki model for predicting ductile fracture under complex loading conditions, *Fatig. Fract. Eng. Mater. Struct.* 40 (12) (2017) 2152–2168.
- [35] A. Vedaldi, B. Fulkerson, *VLFeat: an open and portable library of computer vision algorithms*, <http://www.vlfeat.org/>, 2008.
- [36] J. Sander, M. Ester, H.-P. Kriegel, X. Xu, Density-based clustering in spatial databases: the algorithm DBSCAN and its applications, *Data Min. Knowl. Discov.* 2 (2) (1998) 169–194.
- [37] C. Szegedy, V. Vanhoucke, S. Ioffe, J. Shlens, Z. Wojna, Rethinking the inception architecture for computer vision, in: *Proceedings of the IEEE Conference on Computer Vision and Pattern Recognition*, 2016, pp. 2818–2826.
- [38] F.A. McClintock, A criterion for ductile fracture by the growth of holes, *J. Appl. Mech.* 35 (2) (1968) 363–371.
- [39] J. Lemaitre, J. Dufailly, Damage measurements, *Eng. Fract. Mech.* 28 (5–6) (1987) 643–661.
- [40] G. Avramovic-Cingara, C.A. Saleh, M. Jain, D. Wilkinson, Void nucleation and growth in dual-phase steel 600 during uniaxial tensile testing, *Metall. Mater. Trans.* 40 (13) (2009) 3117.
- [41] G. Requena, E. Maire, C. Leguen, S. Thuillier, Separation of nucleation and growth of voids during tensile deformation of a dual phase steel using synchrotron microtomography, *Mater. Sci. Eng.* 589 (2014) 242–251.
- [42] C. Landron, E. Maire, J. Adrien, O. Bouaziz, M. Di Michiel, P. Cloetens, H. Suhonen, Resolution effect on the study of ductile damage using synchrotron X-ray tomography, *Nucl. Instrum. Methods Phys. Res. Sect. B Beam Interact. Mater. Atoms* 284 (2012) 15–18.
- [43] J. Kang, Y. Ososkov, J.D. Embury, D.S. Wilkinson, Digital image correlation studies for microscopic strain distribution and damage in dual phase steels, *Scripta Mater.* 56 (2007) 999–1002.
- [44] K.S.C.X. Sun, W.N. Liu, M.A. Khaleel, Predicting failure modes and ductility of dual phase steels using plastic strain localization, *Int. J. Plast.* 25 (2009) 1888–1909.
- [45] J. Kadkhodapour, A. Butz, S.Z. Rad, Mechanisms of void formation during tensile testing in a commercial, dual-phase steel, *Acta Mater.* 59 (2011) 2575–2588.
- [46] L. Morsdorf, C.C. Tasan, D. Ponge, D.J.A.M. Raabe, 3D Structural and Atomic-Scale Analysis of Lath Martensite: Effect of the Transformation Sequence, 95, 2015, pp. 366–377.
- [47] D. Yan, C.C. Tasan, D.J.A.M. Raabe, High Resolution In Situ Mapping of Microstrain and Microstructure Evolution Reveals Damage Resistance Criteria in Dual Phase Steels, 96, 2015, pp. 399–409.

Publication #3

Global and High-Resolution Damage Quantification in Dual-Phase Steel Bending Samples with Varying Stress States

Rickmer Meya, Carl F. Kusche, Christian Löbbbe, Talal Al-Samman, Sandra Korte-Kerzel, A. Erman Tekkaya

Metals 2019, 9(3), 319; March 2019


<https://doi.org/10.3390/met9030319>

For this publication, the candidate performed all SEM observations, and computational analysis of the bending samples and extended the previously presented computational framework to measure individual void areas in order to site-specifically quantify damage in bending samples. The original and revised manuscripts were written by Rickmer Meya and the candidate.



Article

Global and High-Resolution Damage Quantification in Dual-Phase Steel Bending Samples with Varying Stress States

Rickmer Meya ^{1,*}, Carl F. Kusche ², Christian Löbbe ¹, Talal Al-Samman ², Sandra Korte-Kerzel ²  and A. Erman Tekkaya ¹

¹ Institute of forming technology and lightweight components, TU Dortmund University, Baroper Str. 303, 44227 Dortmund, Germany; christian.loebbe@iul.tu-dortmund.de (C.L.); erman.tekkaya@iul.tu-dortmund.de (A.E.T.)

² Institute of physical metallurgy and metal physics, RWTH Aachen, Kopernikusstr. 14, 52056 Aachen, Germany; kusche@imm.rwth-aachen.de (C.F.K.); alsamman@imm.rwth-aachen.de (T.A.-S.); korte-kerzel@imm.rwth-aachen.de (S.K.-K.)

* Correspondence: rickmer.meya@iul.tu-dortmund.de; Tel.: +49-231-755-2669

Received: 31 January 2019; Accepted: 6 March 2019; Published: 12 March 2019



Abstract: In a variety of modern, multi-phase steels, damage evolves during plastic deformation in the form of the nucleation, growth and coalescence of voids in the microstructure. These microscopic sites play a vital role in the evolution of the materials' mechanical properties, and therefore the later performance of bent products, even without having yet led to macroscopic cracking. However, the characterization and quantification of these diminutive sites is complex and time-consuming, especially when areas large enough to be statistically relevant for a complete bent product are considered. Here, we propose two possible solutions to this problem: an advanced, SEM-based method for high-resolution, large-area imaging, and an integral approach for calculating the overall void volume fraction by means of density measurement. These are applied for two bending processes, conventional air bending and radial stress superposed bending (RSS bending), to investigate and compare the strain- and stress-state dependent void evolution. RSS bending reduces the stress triaxiality during forming, which is found to diminish the overall formation of damage sites and their growth by the complimentary characterization approaches of high-resolution SEM and global density measurements.

Keywords: damage; characterization; automated void recognition; density; bending; stress superposition

1. Introduction

Over the past years, processes of damage formation have yielded tremendous interest in the field of materials science, due to the rising demand for advanced metallic materials combining high strength and excellent formability. For many of those materials, damage formation is a point that has to be addressed due to their intrinsic microstructural heterogeneity [1]. Typically, damage formation and accumulation take place during plastic deformation and are most commonly observed as the formation and growth of voids [2]. The interaction of these voids ultimately leads to failure; however, the mechanisms of damage formation and evolution themselves are not part of the process of material failure. During plastic deformation, processes of void nucleation, evolution and coalescence take place and lead to a continuous degradation of mechanical properties, and ultimately, failure.

Before the interaction and coalescence of voids start, void growth is the main mechanism of damage evolution. This process has been extensively researched, especially in the field of modeling,

ranging from the fundamental modelling of void growth [3] and also nucleation [4] to advanced, high-resolution microstructural simulations [5]. As experimental approaches as well as the modelling of void growth have shown, the growth behavior of microstructural voids is largely dependent not only on the magnitude of strain, but in a significant way on the applied stress state [6].

For structural parts in the automotive industry, high-strength values combined with good formability are required; this objective has, recently, mainly been achieved by the usage of advanced high-strength steels (AHSS). A widely used variety of this class are the dual-phase steels. These combine low production costs compared to other AHSS with beneficial ductility, high yield strength values and near-linear strain hardening properties [7]. These properties are realized by a microstructure made up of ferritic and martensitic constituents. However, the complementary properties of these constituents typically cause a strong contrast in plastic deformation between the two phases, leading to a stress and strain partitioning behavior in the local microstructure. This incompatibility leads to the nucleation of voids, caused by distinct mechanisms [8]; the hard martensite islands are prone to locally brittle damage initiation, i.e. martensite cracking. These cracks typically occur at prior austenite grain boundary sites [9]. In addition to this mechanism, decohesion processes at interfaces such as phase boundaries between martensite and ferrite or at ferrite grain boundaries can take place [10]. In many cases, the local morphology [11] and heterogeneity of the microstructure [12] is the main factor determining the dominant damage mechanism, and a wide variety of intermediate forms or combinations of the above-mentioned mechanisms are observed. Commercially used dual-phase steels such as the one employed in this work often show a significant banding of martensite, leading to a pattern of voids often described in the literature as “necklaces” [12]. These agglomerations of voids, typically observed at large strains, are caused by the basic mechanisms of martensite cracking, phase boundary and grain boundary decohesion, but represent a distinct pattern of damage sites in their own right.

In order to link damage formation and stress state, independent parameters—namely the Lode angle parameter, $\bar{\theta}$, and the stress triaxiality η —are used. Both parameters influence the damage evolution [13]. The stress triaxiality, η , is defined as the ratio of hydrostatic stress, σ_h , and the von Mises equivalent stress, σ_{VM} :

$$\eta = \frac{\sigma_h}{\sigma_{VM}} \quad (1)$$

The hydrostatic stress is thought to be responsible for the growth, or if negative, even shrinking of already nucleated voids in the microstructure. It is therefore expected for stress states with lower stress triaxialities to cause a delayed void evolution for forming-induced damage. With the deviatoric stress tensor, σ^{dev} , the third normalized invariant, ξ , can be derived:

$$\xi = \frac{27 \det(\sigma^{dev})}{2 \sigma_{VM}^3} = \frac{27/2 \cdot (\sigma_1 - \sigma_h) \cdot (\sigma_2 - \sigma_h) \cdot (\sigma_3 - \sigma_h)}{\{[(\sigma_1 - \sigma_2)^2 + (\sigma_2 - \sigma_3)^2 + (\sigma_3 - \sigma_1)^2]/2\}^{2/3}} \quad (2)$$

This invariant ξ is defined in the range of $-1 \leq \xi \leq 1$. The normalized Lode angle parameter, $\bar{\theta}$, is defined as

$$\bar{\theta} = 1 - \frac{2}{\pi} \arccos(\xi) \quad (3)$$

During plane strain plastic forming, the second principal stress is always

$$\sigma_2 = \frac{\sigma_1 + \sigma_3}{2} \quad (4)$$

In the bending of sheet with a much larger width compared to the thickness, plane strain deformation conditions can be assumed. This leads to a constant normalized Lode angle parameter, $\bar{\theta} = 0$.

Anderson et al. [14] revealed that the strain to fracture for a lower triaxiality is lower compared to higher triaxialities for a constant Lode angle parameter in DP800 steels. Thus, the stress state is

important for material failure, but it also influences damage evolution, as failure can be the consequence of damage. Technologically, the stress state during bending must then be influenced to reduce damage. Technological solutions are, for instance, bending with a solid counter punch [15], roll bending with additional rolls [16], bending with an elastomer [17] and radial stress superposed bending [18]. Bending using elastomers is capable of reducing the stress triaxiality during bending by applying a counter pressure due to the inserted elastomer. This leads to a delayed damage evolution in terms of void nucleation, which subsequently influences the fatigue lifetime of bent products [19]. Thus, the accumulation of damage during forming is important for lightweight design and has to be taken into account as it affects the product performance. For industrial purposes, elastomer-bending is not feasible for controlling the stress state, as the elastomer does not apply reproducible counter pressures during forming and is limited in the magnitude of applicable stresses (the maximum pressure is less than 150 MPa), as well as showing a rapid degradation over its lifetime. Recently, a new bending process with predetermined stress states was introduced [20]. The so-called radial stress superposed bending (RSS bending) is capable of reducing the stress triaxiality and applying pressures up to the flow stress of the material in a reproducible way. It has already been shown to protract damage nucleation, leading to a reduced number of voids [20].

For the product design or process modeling, the amount of damage can be expressed directly as the area or volume fractions of voids or indirectly via certain mechanical properties. Lemaitre and Dufailly (1987) showed eight methods for direct and indirect damage measurement techniques and rated their suitability [21]. Direct measurements include microscopic analysis, X-ray analysis and density measurements. Indirect damage measurements are, for example, the decrease in Young's modulus, micro hardness or indentation modulus [22]. For damage quantification, direct measurements are preferable as there is no mathematical model connected to the calculation of damage quantity. A damage variable, D_s , in surface observations is proposed by Lemaitre and Dufailly as the ratio of the void area, S_d , and the undamaged area, S [21].

For a DP600, the void volume fraction before failure is usually below 1–2% of the whole volume [22]. Consequently, the preparation of specimens for direct surface measurements is challenging. Samuels et al. showed that mechanical polishing might introduce strain hardening in the material surface [23]. Also, a void smearing effect could be shown due to different polishing steps [24]. Isik et al. revealed that ion beam slope cutting is capable of analyzing void sizes down to $0.05 \mu\text{m}^2$ [25]. Another quantification method is radiography. Using X-ray microtomography, specimens can be analyzed without metallographic preparation in a non-destructive way; this method is, however, limited by its spatial resolution [26].

For an integral approach to measuring void volume fractions, density measurements can be applied. Ratcliffe presented a method for measuring small density changes in solids using the Archimedean principle [27]. Schmitt et al. showed that different strain paths lead to different relative density changes [28]. Bompard proved the possibility of measuring density changes in a tensile specimen and correlated this to damage [29]. The method has equally been applied by Lemaitre and Dufailly to quantify damage evolution [21].

Lapovok et al. measured the density of specimens in a continuously cast aluminum alloy formed in an equal channel angular drawing process with the help of the Archimedean principle [30]. Tetrachloroethylene with a density of 1.62 g/cm^3 was used instead of distilled water for higher accuracy. They correlated the change in density to the stress and strain state that is responsible for different paths of damage evolution. Tasan et al. stated that tactile density measurements are not capable of analyzing damage for specimens with a volume of as low as 1 mm^3 for spatially resolved measurements [22] as the scatter observed for small volumes dominates the measurements.

Thus, in the current state of the art, it is shown that stress superposition during bending leads to delayed fracture. Despite this, it is not clear what influence the lowered stress triaxiality has on the void evolution and damage mechanisms. To quantify and characterize damage in bent samples, the methods for automated void recognition and density measurements have to be adopted to the

requirements set by bending samples. With these characterization tools, the influence of the alteration in stress state on damage evolution can be quantified and subsequently used for the modelling or prediction of the expected service life time.

2. Materials and Methods

The DP steel applied in this study is of DP800 grade, which usually indicates that it has a guaranteed tensile strength of more than 800 MPa and its microstructure consists mainly of ferritic and martensitic constituents. However, a very small fraction of remaining austenite and bainite might still be present in the microstructure in small volume percentages. The as-received DP800 sheet material was subjected to a hot-dip galvanizing process using a zinc bath, which provides the rolled sheets with corrosion protection. The average grain size ranges from 2 μm to 20 μm , with martensite particles of approx. 2 μm in diameter embedded in the matrix. The characterized microstructure material shows a strong banding of the martensite phase along the rolling direction (Figure 1).

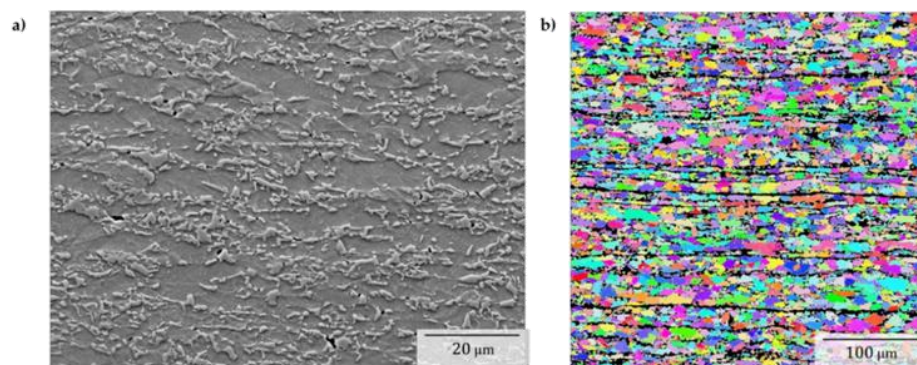


Figure 1. (a) Microstructure of the used dual-phase DP800 steel imaged by SEM, with visible deformation-induced voids. (b) Electron-backscatter-diffraction mapping of ferrite grains; martensite bands are visible as black areas.

The flow curve at room temperature (obtained by a Zwick Z250 universal testing machine, ZwickRoell GmbH & Co. KG, Ulm, Germany) is given by experimental data from uniaxial tensile tests and extrapolated according to Gosh (Figure 2).

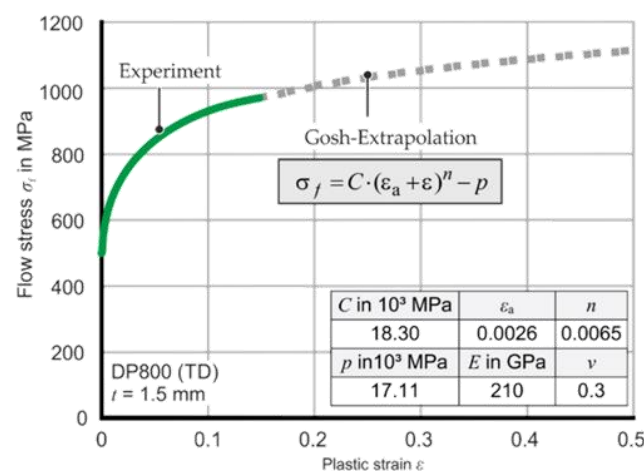


Figure 2. Flow curve of the investigated DP800 steel with experimental data and extrapolation according to Gosh.

The tensile tests were conducted with a specimen geometry (DIN 50125—H 20 × 80) according to DIN EN ISO 6892-1 with a velocity of 0.0067 s^{-1} to ensure a constant strain rate. The measurement of the elongation was done directly on the test sample with a tactile macro-extensometer (Gauge length of 80 mm, ZwickRoell GmbH & Co. KG, Ulm, Germany). The flow curve is derived up to the uniform elongation experimentally and then extrapolated. The extrapolation parameters (ϵ_a : strain at yielding, n : hardening exponent, C and p : fitting parameters) according to Gosh are derived with the least square fitting method. The Young's modulus E and Poisson's ratio ν are given in Figure 2.

2.1. SEM Panoramic Imaging, Void Recognition and Area Determination

Deformation-induced damage in these grades of dual-phase steels typically occurs in the form of microscopic voids with sizes in the range of several hundred nm [8] to a few μm [26]. To reliably quantify voids at such small scales, high-resolution measurements of large micrographs in the order of mm^2 are required. This was achieved in the present work by employing advanced scanning electron microscopy (LEO 1530, Carl Zeiss Microscopy GmbH, Jena, Germany) combined with panoramic imaging and an image stitching algorithm based on the VLFeat Matlab toolbox [31]. All panoramic images have been obtained at the tip of the bending sample (Figure 3) at a resolution of 32 nm/px using secondary electrons (SE) and a 20% area overlap. The field width of a single image was 100 μm , resulting in a total panoramic image size of 1000 $\mu\text{m} \times 500 \mu\text{m}$. Respective specimens were mechanically polished to 0.25 μm and subsequently etched in 1% Nital for 10 s. A consistent, light etching is critical for this method, as shadowing effects of the protruding martensite phase have to be minimized for a reliable automated image recognition. The panoramic images are subsequently split into 5 slices that follow a radial direction. This approach is chosen to ensure an accurate measurement of the respective distance to the outer radius, which would be altered as, in bending samples, the upper edge cannot be straight. A binning of 3000 pixels in a radial direction was applied, and each data point was attributed to the middle of this bin, resulting in the outermost value for the distance to the outer radius being calculated as 48 μm from the edge.

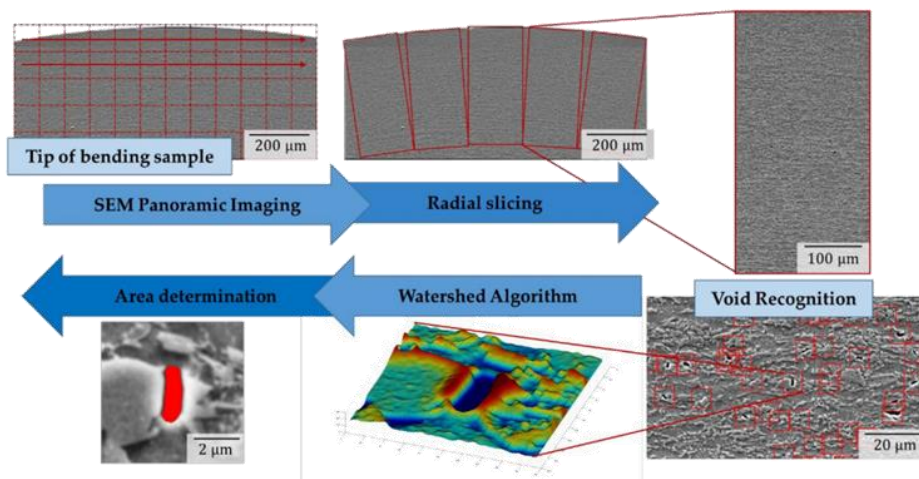


Figure 3. Schematic representation of void area measurements from panoramic SEM imaging. Individual images are stitched and voids recognized via a grayscale threshold. The identified voids are then individually processed using a watershed algorithm to measure their size.

Voids are identified using a grayscale threshold and the located sites from the original image processed further by the use of a watershed algorithm [32]. Here, by altering the grayscale threshold around the individual void, the optimum value for measuring the entire void area, but none of the surrounding microstructure, is determined. The calculation of the pixel areas results in a separate

measurement for each individual void. This approach makes it possible to collect data not only for overall void area fractions, but for any type of measurement where information about each individual damage site is required. To calculate area fractions over one spatial coordinate, a moving bin is applied to smooth out peaks in the area fraction generated by single, larger voids, made possible by the individual identification and localization of damage sites.

A considerable error in the void area measurements of deformation-induced damage voids is generated by inclusions. These, in commercial DP steel, typically being TiN, can be caused to fall out of the polished surface during preparation, leaving voids of a similar, slightly larger diameter in the observed images. Examples of this type of voids as well as the above-mentioned fundamental mechanisms of damage nucleation and formation are shown in Figure 4. These voids at the sites of inclusions have a very different morphology from martensite cracks or interface decohesion sites, making them an ideal subject for recognition by deep learning [33]. In this work, neural networks have been trained using an initial data set, with the goal of automatically detecting voids that have been caused by inclusions in the microstructure. A system for recognizing these inclusions from SEM pictures has been developed and tested to an accuracy of over 95% and is applicable to the SEM panoramas used in this study [33]; here, it is used for inclusion void recognition only. With smaller plastic equivalent strains towards the sheet center, voids caused by inclusions become increasingly dominant, as this type of observed void is in the majority of cases an artefact of metallographic preparation by mechanical polishing. Non-metallic inclusions leave the surface during this process, and therefore cause surface voids that did not develop during plastic deformation and are therefore not to be measured simultaneously with plasticity-induced damage. The error normally introduced by measuring these inclusions as part of the void fraction is avoided by the recognition and exclusion of these particular voids.

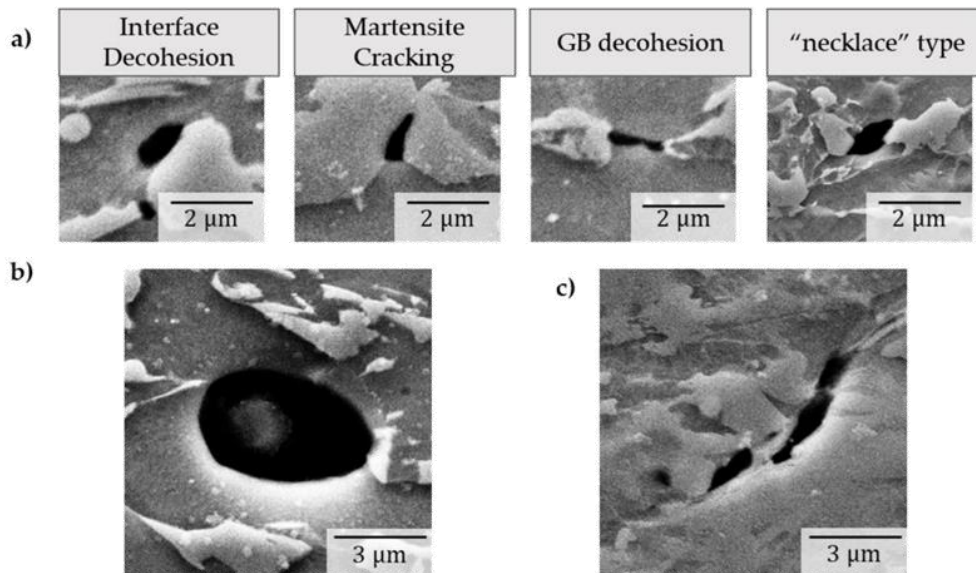


Figure 4. (a) Examples of fundamental damage mechanisms of martensite/ferrite interface decohesion, martensite cracking, ferrite grain boundary (GB) decohesion and “necklace” type voids between two adjacent martensite particles; (b) void observed due to (partly) removed inclusions from the surface, recognized by a deep learning algorithm; (c) void coalescence near the outer surface of an air bending sample.

The panoramic imaging method was carried out in the x - y plane ("in-plane") of a bending sample. To analyze all spatial directions, a second measurement was taken on a plane in the middle of the bending zone, parallel to the bending axis in z direction ("cross-section") (Figure 5).

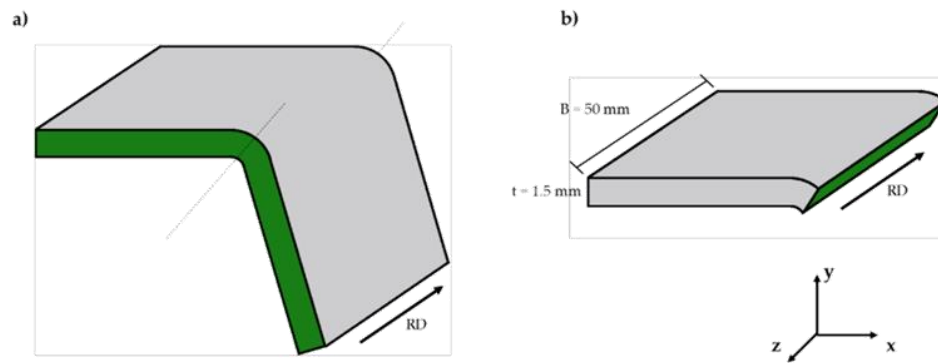


Figure 5. Evaluated planes in the bending samples (illustration): (a) cutting plane parallel to the bending plane ("in-plane", x - y plane); (b) cutting plane parallel to the bending axis ("cross-section", y - z plane). RD represents the rolling direction of the sheet.

The results were taken from these two perpendicular planes as the evolution and growth of voids are expected to be highly anisotropic due to the tensile stresses perpendicular to the bending radius, which will affect the morphology of voids.

2.2. Density Measurement Method

Density measurements of heavy metals for damage quantification require a high resolution in the order of 0.002 g/cm^3 as void volume fractions as low as 0.2% are investigated. The measurement principle is based on hydrostatic weighing. A solid immersed in liquid apparently reduces its weight by the liquid volume weight. It is necessary to know the density of the liquid to measure the density of the submerged solid. In contrast to the classical Archimedean density measurement, the volume of the displaced liquid is not measured by an overflow, but the weight differences are measured. Therefore, this method is strongly dependent on the volume of the specimen, as higher volumina lead to higher precision. The IMETERV6 device (IMETER/MSB Breitwieser MessSysteme, Augsburg, Germany) is used for the measurements in this work. The measuring process consists of taring the specimen holder in the measuring liquid at the predefined immersion depth, then withdrawing and connecting to the specimen (Figure 6).

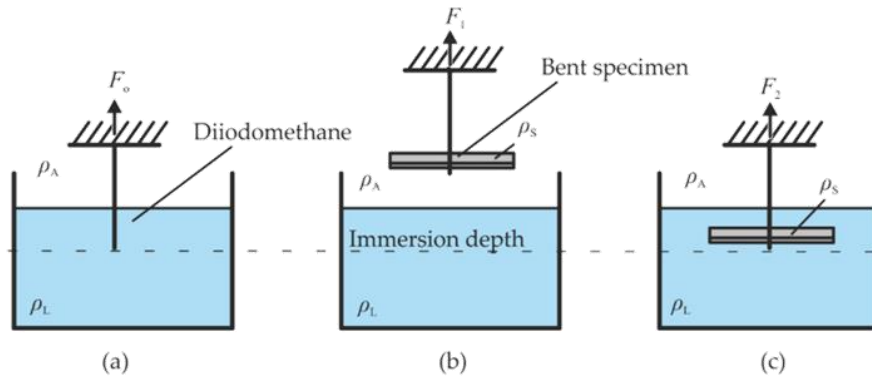


Figure 6. Buoyancy principle for density measurement: (a) calibration of the suspension in ambient air; (b) weighing of the specimen in ambient air; (c) weighing of the specimen in the measuring liquid.

Subsequently, the weighing of the specimen takes place in ambient air. Afterwards, specimens are immersed to exactly the same immersion depth with the same contact angle of the attached wire likewise at taring and weighing the buoyancy after the same predefined diving time. The same contact angle of the wire and liquid as well as the predefined immersion time are important for the measuring accuracy. Withdrawing and immersional weighing is repeated several times (15 to 25 times for 10 to 15 min) until the buoyancy values are constant. Thus, finally, all air bubbles from the surface are washed away and differences in the temperature of specimen and liquid have been compensated. The specimen is connected to a load cell (Sartorius AG, Göttingen, Germany) with a thin tungsten wire ($D = 40 \mu\text{m}$). The higher the density of the liquid, the higher the lifting force and therefore the measuring accuracy. Diiodomethane (CH_2I_2) is used as the immersion liquid, which is a so-called heavy liquid [34]. The measured density is 3.3027 g/cm^3 at 25°C [35]. The density of a solid ρ_s can thus be determined according to physical relationships [35]. This calculation requires the density of the liquid ρ_L , the density of the ambient air ρ_A , the resulting force on the specimen outside the measuring liquid W_1 and that immersed in the measuring liquid, W_2 .

$$\rho_s = \frac{\rho_L - \rho_A}{1 - \frac{W_2}{W_1}} + \rho_A \quad (5)$$

To calculate the void volume fraction in the bent product, specimens are cut out of the bending zone and the bending leg of the samples. Since the properties of a bent part deviate at the edge of the sheet (the assumption of plane strain is invalid), only the constant area of the bending zone is examined (5 mm apart from the outer edges) (Figure 7).

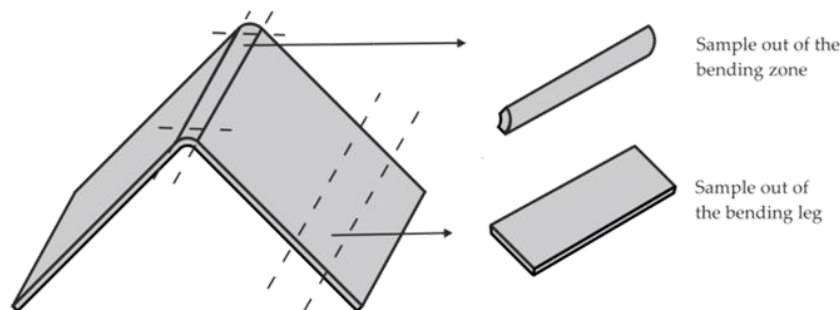


Figure 7. Area of sampling in a bent profile.

The investigated air-bending process is defined by the geometrical parameters: die width w_d , punch radius r_p and die radius r_d (Figure 8). The sheet is laser cut (100 mm \times 50 mm \times 1.5 mm) and bent parallel to the rolling direction to an unloaded bending angle of 66°.

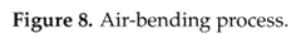
[illegible]

Figure 9. Technological implementation of radial stress superposed (RSS) bending.

The applied process parameters lead to a comparable geometry of the bent products. For the validation of the identical strain at the outer fiber, optical measurements and hardness measurements are used. Stress triaxiality values and the strain distribution over the sheet thickness is investigated numerically according to the model presented in previous work [37]. The FEM-modeling was carried out with the elastic-plastic modelling with ABAQUS2016/Implicit2D (Dassault Systèmes, Vélizy-Villacoublay Cedex, France). Plane strain conditions and a planar symmetry were assumed to reduce computational effort. The sheet is modelled with the flow curve given in Figure 2. The rotating tools are modelled to be purely elastic, and all other components are rigid. The smallest element size in the bending zone is 0.05 mm and in the bending leg is 0.3 mm. The friction between the tools is modelled by the Coulomb friction law ($\mu = 0.02$ between the lower rotating tools and the sheet/lower bearing shell, since it is lubricated; $\mu = 0.1$ between the upper rotating tool and the sheet/upper bearing shell; $\mu = 0.1$ in air bending). The maximum force deviation between the numerical and experimental punch force was lower than 10% [37].

Corresponding to Meya et al. [37], the stress triaxiality in air bending is $\eta_{\min} = 0.57$, while the minimum stress triaxiality during RSS bending in this set-up is calculated as $\eta_{\min} = -0.06$ at the outer fiber due to the superposed stresses.

3. Results

3.1. SEM-Based Damage Characterisation and Quantification

The measurements obtained by SEM observation yielded results for the global quantification of deformation-induced voids in the bent samples in the form of area fraction calculations, as well as achieving magnifications high enough to gain microstructural information about the individual mechanisms of damage nucleation and evolution, which have, however, not been considered in this work.

Firstly, the dominance of voids originating from inclusions in the steel microstructure becomes obvious when regarding the panoramic images; with greater distances from the outer radius, larger voids can almost exclusively be recognized as being caused by inclusions being removed from the polished surface during the preparation of the sample.

Secondly, regarding deformation-induced damage, both the absolute number of voids (Figure 10) and the mean size (Figure 11) of the voids are observed to increase towards the outer radius—the zone of the highest plastic equivalent strain. These observations are true for both applied bending methods and both observation planes. Representative examples of typical voids at the outer radius, at a distance of approx. 80 μm below the surface and at 400 μm below the outer radius, are given in Figure 11.

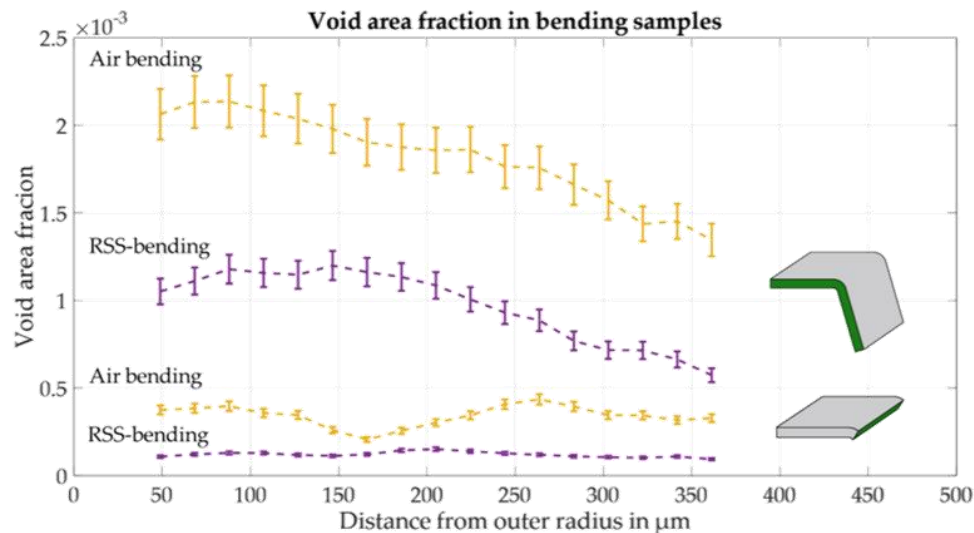


Figure 10. Void area fraction in air bending and RSS bending in the outer fibers measured by SEM imaging and automated void recognition.

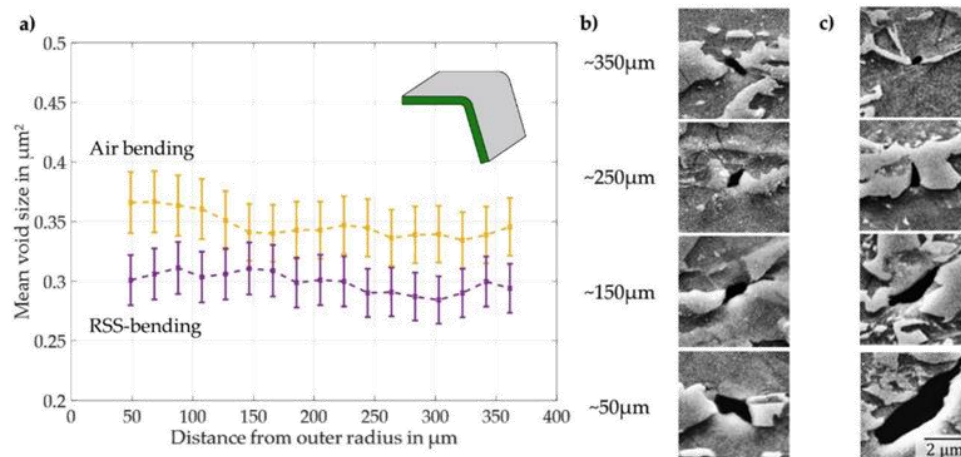


Figure 11. (a) Mean void size in the in-plane samples for air-bent and RSS-bent samples; representative void morphologies at various distances from the outer radius for (b) RSS bending and (c) air bending.

For each data point, an area of $33,379 \mu\text{m}^2$ was evaluated. The error for the measurements is calculated via the error for the watershed algorithm value for each single void, and summarized over all voids in the field of observation.

Comparing the area fractions, voids per area ($n = 5345 \text{ voids}/\text{mm}^2$ vs. $n = 3589 \text{ voids}/\text{mm}^2$ at the outer fiber) and void sizes ($S = 0.37 \mu\text{m}^2$ vs. $S = 0.30 \mu\text{m}^2$ at the outer fiber) across the two applied processes, a significant change in all these quantities is observable for the radial stress superposed (RSS) bending method compared with conventional air-bending. As calculating the void area fraction for various regions of the sample takes into account the overall magnitude of voids existing and nucleating in the observed area and their sizes, this property is able to deliver a more complete picture of void nucleation and growth compared to solely regarding void numbers or mean sizes. Area fraction calculations from the detected voids show an average decrease of 52.1% for the RSS bending.

The void area fractions measured in the cross-section are significantly smaller (up to 4 times), as the imaging plane is perpendicular to the bending strain ϵ_x and no macroscopic strain in the z-direction occurs. However, in these images an average decrease in void area fractions up to 69% for the triaxiality-reduced RSS-bending process is also visible.

Measurements in as-received, undeformed samples only found 3 to 5 voids that could not be reliably attributed to being caused by inclusions on the same field of view as used in the measurements above. Therefore, the void area fractions for the undeformed state of the sheet metal are assumed to be non-existent.

The results for mean void areas equally show a lower average void area for the RSS-bending process; this effect is, however, largely dominated by the scatter in void sizes, in particular at the region near the outer radius. On the one hand, large voids are found in this region in the air-bending samples, whereas the RSS-bending process does not provoke these large void sizes. A typical evolution of voids for both bending processes is shown in Figure 11. However, a clear difference in size emerges when regarding maximum void sizes instead of mean values; while for the air-bending process, void sizes at the outer radius reach up to $2.26 \mu\text{m}^2$, RSS-bent samples only showed void sizes lower than $1.22 \mu\text{m}^2$. This tendency does not appear in the mean void size calculations, as these are dominated by the large number of nucleating voids below $0.3 \mu\text{m}^2$ in size. This tendency for the growth of voids in air-bending samples can be underlined by normalizing the mean void sizes not by number, but by their respective area fractions. While for air bending, 74.9% of the total void area is made up by voids larger than the calculated mean void size per bin, this fraction calculates to a smaller value of 65.7% for the RSS-bending samples. Even though there is no clear threshold in size or morphology after which a void can clearly be classified as “grown”, this statistical approach shows a difference in the composition of the cumulative void area from small and large void sizes.

3.2. Density Measurements

The specimen is not tempered in advance, so it needs time to adapt its temperature to the measuring fluid. Also, the tempering of the measuring cup fluctuates because of the specimen immersion. The measurements are repeated several times to compensate and stabilize the influences of temperature differences and air bubbles (Figure 12).

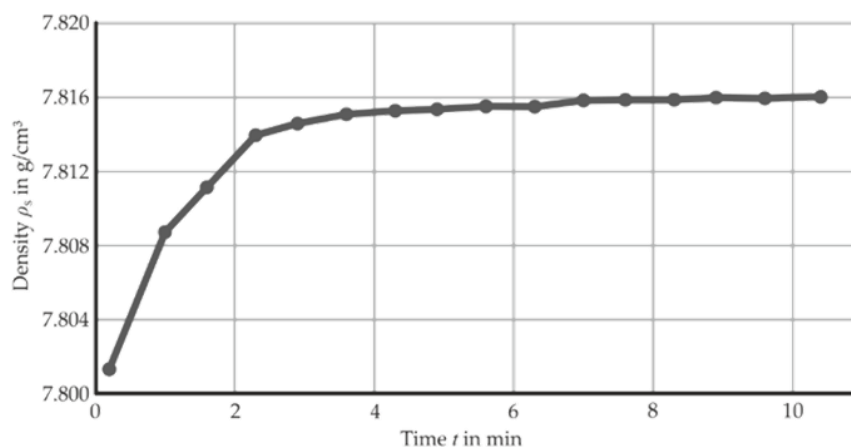


Figure 12. Density fluctuation due to bubbles and alternating temperature over time for an unbent sheet.

The overall uncertainty regarding the measured density is a function of the measuring accuracy of the loading cell, the tempering, the ambient air and fluid density as well as the calculated temperature dependency of the fluid. The uncertainty reduces with a higher specimen volume and higher density of

the fluid. In this set-up, the average uncertainty of the density is 0.0021 g/cm^3 for a specimen volume of 1 cm^3 . The influence of the altered stress triaxiality on macroscopic density and the uncertainty of different specimens shows a maximum fluctuation of $\pm 0.0008 \text{ g/cm}^3$ (Figure 13).

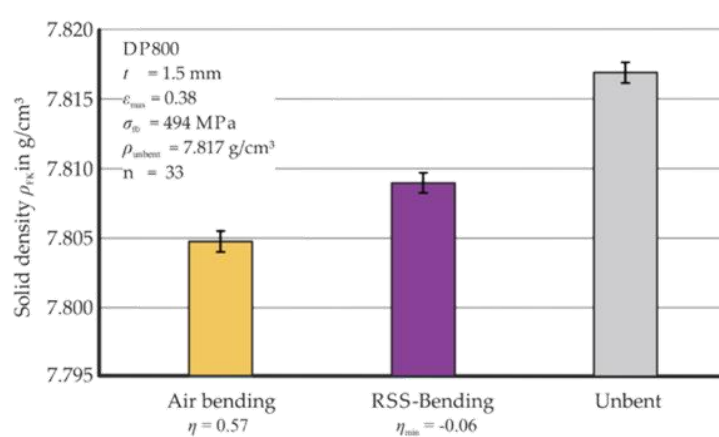


Figure 13. Density of different bent products in comparison to the as-received material.

The density of the air-bent part ($\eta_{\min} = 0.57$) is reduced by 0.15% compared to the as-received material. In comparison, the RSS-bent ($\eta_{\min} = -0.06$) product's density is reduced by 0.10%. Thus, a reduction of 33% in density loss is achieved by using the applied stress superposition during bending.

3.3. Resulting Strains and Stresses in Bending

The maximum curvature is measured by light optical microscopy and is revealed to be $0.307 \pm 0.002 \text{ mm}^{-1}$ for air bending and $0.310 \pm 0.004 \text{ mm}^{-1}$ for RSS-bending samples at the symmetry axis of the bending area. This difference of around 1% in curvature indicates similar plastic strains at the outer fiber. The numerically investigated strain distribution is also comparable, since the deviation of the equivalent plastic strain over the investigated area is less than 10% (Figure 14).

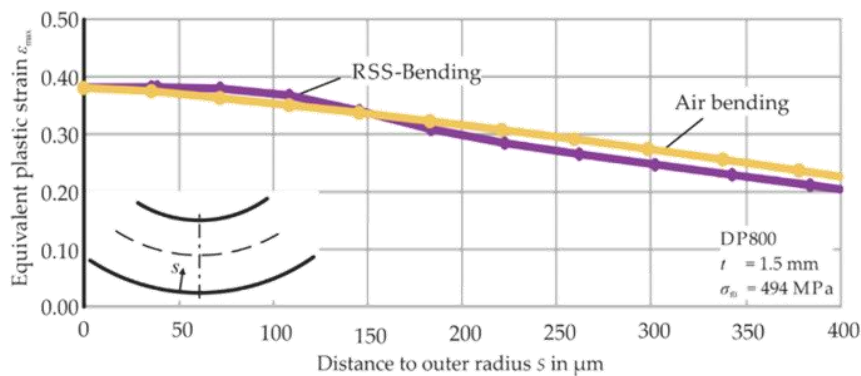


Figure 14. Equivalent strain distribution in air bending and RSS bending at the outer fiber.

In order to neglect the influence of strain hardening in the comparison of air bent and RSS-bent products, micro hardness measurements are also conducted. The average Vickers hardness HV0.1 over the bending zone at the circumference is measured as $327 \pm 23 \text{ HV0.1}$ ($\eta_{\min} = 0.57$) for air bending and $326 \pm 19 \text{ HV0.1}$ ($\eta_{\min} = -0.06$) for RSS bending. The Vickers measurements are conducted with an HMV-G21D hardness testing machine (Shimadzu Corporation, Kyoto, Japan) and a test

load of 980.7 mN. The duration time of indentation is 10 s and 40 indentations with a distance of 0.075 mm between the measuring were done per sample. For each bending process, two samples were investigated.

Due to this neglectable difference in sample geometry and applied strains, the undergone stress state during forming can be thought to be responsible for any measured deviations in damage characteristics. The stress triaxiality values calculated over the sheet thickness in the outer fiber differ from air bending to RSS bending (Figure 15).

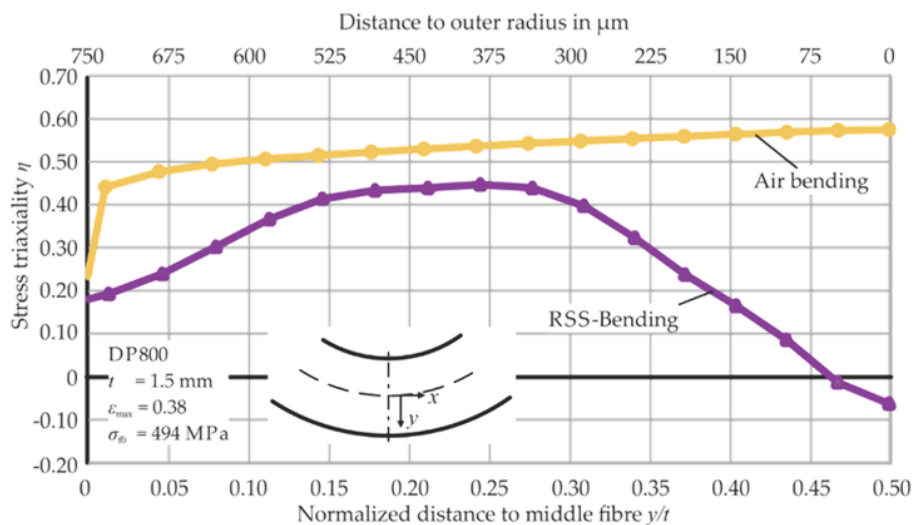


Figure 15. Triaxiality distribution in air bending and RSS bending during maximum stress superposition in the outer fibers.

In general, the air bending manifests a triaxiality of $\eta = 0.57$ at the outer fiber. In RSS bending, stress triaxialities are lower for every point at the outer fiber while superposed stresses are applied by the bending tool. During the superposition of compressive stresses, triaxiality reaches negative values at the outer fiber ($\eta_{\min} = -0.06$), where the highest void volume fraction is expected due to the highest plastic strains. After the point of maximum stress superposition (Figure 15), triaxiality increases to $\eta = 0.57$ at the outer fiber until the plastic strain remains constant due to the moving forming zone in RSS bending [37].

4. Discussion

In the direct SEM-based observations of void evolution in bending samples, all classically known mechanisms and patterns of damage formation in dual-phase steels could be observed. The samples did not yet enter the state of crack formation, which is essential for observing and evaluating single voids and establishing a clear distinction between damage formation and material failure.

Deformation-induced damage voids can be sighted for regions up to 500 μm under the outer surface; for the area further towards the middle of the sheet, tensile strains are not high enough to nucleate a measurable number of voids. However, a dominant result of the void area measurements is that the average void size over all voids observed in a region does not increase drastically. This is explained by the fact that the nucleation of voids does not stop at higher plastic equivalent strains, leading to a steadily increasing number of newly nucleated, small voids. These are as dominant for the evolution of average void sizes as the evolution and growth of a few, single voids and therefore overshadow the growth of single voids when regarding mean void sizes only. Contrasting the

observations of single, significantly larger voids near the outer radius, however, no increase in mean void size is observed for the RSS-bending process.

In comparison with the conventional air-bending process, the reduced triaxialities in the radial stress superposed bending process lead to a significant decrease in void area fractions. Compared to mean void size calculations, regarding area fractions yields a more complete picture of the damage state, as it takes both void nucleation and growth into account in its cumulative approach. This effect is particularly underlined by the previously-mentioned pronounced growth of voids that can be seen in the samples deformed with the conventional air-bending process. As shown in Figure 11, a clear evolution pattern of voids in a radial direction towards the outer radius could be observed; starting with mainly small voids, typically in the form of martensite cracking of void nucleation in martensite bands, the increasing tensile strains in all bending samples lead to a pronounced growth and additional nucleation of voids in that direction. Up to the outer radius of the sample, where significantly larger, evolved voids are observed, a considerable difference in void evolution behavior could be observed, as incidents of largely evolved voids over $2 \mu\text{m}^2$ in area are solely found in the air-bending samples, and not in the RSS-bent samples. This behavior of damage evolution is explained with the reduced triaxiality depicted in Figure 15 for the RSS-bending process. Corresponding to the damage model of Oyane [38], the measurements show a decrease in void area fraction for lower triaxialities in the RSS-bending process and equally in the maximum observed void sizes of $2.26 \mu\text{m}^2$ compared to $1.22 \mu\text{m}^2$.

The area fractions observed for the cross-section measurements range significantly under the in-plane measurements, but still show a clear distinction between air- and RSS-bending samples. As plane strain bending can be assumed in the middle of the sheet, no macroscopic strains in any of the plane directions for this observation plane occur. Here, tensile strains are perpendicular to the observation plane. The void morphology in the in-plane measurements was dominated by the growth of voids in the x-direction, this being the direction of tensile strains. Therefore, the growth in size of these voids is not to be observed in a cross-section of the sample. Void area fractions are therefore expected to be significantly higher for in-plane measurements as the major part of the void growth can be observed and measured.

The density measurements reveal a decrease in density of 0.15% for air bending and 0.10% for RSS bending compared to the unbent material. This implies an increase of void volume fraction by 33% for the air-bending process. Compared to the results of the undergone SEM analysis, values in a comparable magnitude are calculated: for RSS bending, the average decrease in void area fraction is calculated to be 44.7%.

Compared to previous work on bending processes, a drastic improvement in both damage-reduced bending technology and damage quantification is realized. Solid counter punches [15] as well as elastomer bending [17] reduce the tendency of cracking and reduce damage; however, these effects on damage void formation and growth have so far not been able to be quantified in a detailed way. The predicted damage reduction due to compressive stress superposition according to Lemaitre [3] has been calculated for elastomer bending [39]. In this work, the applied advanced characterization methods enable the experimental determination of damage quantity and its correlation to stress triaxiality. Additionally, in contrast to the aforementioned bending processes, RSS bending does not only reduce triaxiality and therefore damage, but also proves more controllable and reproducible.

5. Conclusions

A quantitative approach for the characterization of forming-induced damage is mandatory for accurately estimating product performance.

High-resolution SEM imaging coupled to automated void recognition has proven to enable the area measurement of a statistically significant proportion of microstructural, forming-induced voids. This leads to a large-area observation of void sizes and subsequent calculation of void area fractions. A detailed analysis of all occurring voids is therefore made possible.

Void area fractions as well as density measurements show a decrease in the same order of magnitude for damage quantity in the RSS-bending process, which is correlated to its lower triaxiality values, as differences in plastic strain are negligible.

Both the overall number of forming-induced voids and their maximum size is measured to be affected by the altered stress state. The nucleation as well as the growth of voids is therefore assumed to be dependent on the magnitude of triaxiality.

Compared to other bending processes that use superposed stresses to increase formability, the RSS-bending process has proven to also reduce microstructural damage occurring before the onset of fracture without their typical loss in reproducibility or restrictions in the magnitude of superposed stresses.

Designing geometrically identical bent parts using alternative load paths has proven to reduce damage, which will consequently lead to an increased performance. This will contribute to lightweight design via the realization of thinner sheet metal parts while maintaining their mechanical performance.

Author Contributions: R.M. performed the bending experiments and analyzed the data of the bending processes and the density measurements. C.F.K. performed the SEM-measurements and developed the methodology of automatic SEM-analysis. R.M. and C.F.K. wrote the manuscript. C.L., T.A.-S., S.K.-K. and A.E.T. reviewed the results and conclusions.

Funding: The investigations are kindly supported by the German Research Foundation in context of the Collaborative Research Centre CRC/Transregio 188 “Damage-Controlled forming processes”, projects A05 and B02.

Acknowledgments: The investigations are kindly supported by the German Research Foundation in context of the Collaborative Research Centre CRC/Transregio 188 “Damage-Controlled forming processes”, projects A05 and B02. We thank Mr. Michael Breitwieser for the density measurements and his lecture of the density theory.

Conflicts of Interest: The authors declare no conflict of interest.

References

1. Ghadbeigi, H.; Pinna, C.; Celotto, S.; Yates, J.R. Local plastic strain evolution in a high strength dual-phase steel. *Mater. Sci. Eng. A* **2010**, *527*, 5026–5032. [\[CrossRef\]](#)
2. Tasan, C.C.; Diehl, M.; Yan, D.; Bechtold, M.; Roters, F.; Schemmann, L.; Zheng, C.; Peranio, N.; Ponge, D.; Koyama, M.; et al. An Overview of Dual-Phase Steels: Advances in Microstructure-Oriented Processing and Micromechanically Guided Design. *Annu. Rev. Mater. Res.* **2015**, *45*, 391–431. [\[CrossRef\]](#)
3. Lemaitre, J. A Continuous Damage Mechanics Model for Ductile Fracture. *J. Eng. Mater. Technol.* **1985**, *107*, 83–89. [\[CrossRef\]](#)
4. Gurson, A.L. Continuum Theory of Ductile Rupture by Void Nucleation and Growth: Part I—Yield Criteria and Flow Rules for Porous Ductile Media. *J. Eng. Mater. Technol.* **1977**, *99*, 2–15. [\[CrossRef\]](#)
5. Tasan, C.C.; Diehl, M.; Yan, D.; Zambaldi, C.; Shanthraj, P.; Roters, F.; Raabe, D. Integrated experimental—Simulation analysis of stress and strain partitioning in multiphase alloys. *Acta Mater.* **2014**, *81*, 386–400. [\[CrossRef\]](#)
6. McClintock, F.A. A Criterion for Ductile Fracture by the Growth of Holes. *J. Appl. Mech.* **1968**, *35*, 363–371. [\[CrossRef\]](#)
7. Mukherjee, K.; Hazra, S.S.; Militzer, M. Grain Refinement in Dual-Phase Steels. *Metall. Mater. Trans. A* **2009**, *40*, 2145–2159. [\[CrossRef\]](#)
8. Kadkhodapour, J.; Butz, A.; Ziaei Rad, S. Mechanisms of void formation during tensile testing in a commercial, dual-phase steel. *Acta Mater.* **2011**, *59*, 2575–2588. [\[CrossRef\]](#)
9. Archie, F.; Li, X.; Zaefferer, S. Micro-damage initiation in ferrite-martensite DP microstructures: A statistical characterization of crystallographic and chemical parameters. *Mater. Sci. Eng. A* **2017**, *701*, 302–313. [\[CrossRef\]](#)
10. Landron, C.; Bouaziz, O.; Maire, E.; Adrien, J. Characterization and modeling of void nucleation by interface decohesion in dual phase steels. *Scr. Mater.* **2010**, *63*, 973–976. [\[CrossRef\]](#)
11. Erdogan, M. The effect of new ferrite content on the tensile fracture behaviour of dual phase steels. *J. Mater. Sci.* **2002**, *37*, 3623–3630. [\[CrossRef\]](#)

38. Oya, G.; Mo, S.; Kimoto, K.; Shimada, T.; Ueda, M. *Crack Initiation and Propagation in Dual-Phase Steels: Influence of Martensite Volume Fraction*. *Mater. Sci. Eng. A* **2015**, *616*, 1–10. [CrossRef]
39. El-Badry, A.; Clausmeyer, T.; Gebhard, J.; Chen, L.; Tekkaya, A.E. *Erweiterung des Biegeprozesses für die Herstellung von Blechen mit einer hohen Biegegeschwindigkeit*. *Praxis der Fertigung* **2018**, *106*, 1–10. [CrossRef]
13. Bei, K. *Korrosionsverhalten von Blechen aus Stahlwerkstoffen bei Biege- und Zugversuch*. *Praxis der Fertigung* **2018**, *106*, 1–10. [CrossRef]
14. Germany, D. *Butcher, C.; Pathak, N.; Worswick, M.J. Failure parameter identification and validation for a dual-phase 780 steel sheet*. *Int. J. Solids Struct.* **2017**, *124*, 89–107. [CrossRef]
- © 2019 by the authors. Licensee MDPI, Basel, Switzerland. This article is an open access article distributed under the terms and conditions of the Creative Commons Attribution (CC BY) license (<http://creativecommons.org/licenses/by/4.0/>).
17. Schiefenbusch, J. *Untersuchungen zur Verbesserung des Umformverhaltens von Blechen beim Biegen*. Ph.D. Thesis, Universität Dortmund, Dortmund, Germany, 1983.
18. Meya, R.; Löbke, C.; Tekkaya, A.E. Stress State Control by a novel bending process and its effect on damage evolution. In Proceedings of the 2018 Manufacturing Science and Engineering Conference MSEC, College Station, TX, USA, 18–22 June 2018.
19. Tekkaya, A.E.; Ben Khalifa, N.; Hering, O.; Meya, R.; Myslicki, S.; Walther, F. Forming-induced damage and its effects on product properties. *CIRP Ann. Manuf. Technol.* **2017**, *66*, 281–284. [CrossRef]
20. Meya, R.; Löbke, C.; Hering, O.; Tekkaya, A.E. New bending process with superposition of radial stresses for damage control. In Proceedings of the Forming Technology Forum, Enschede, The Netherlands, 12–13 October 2017.
21. Lemaitre, J.; Dufailly, J. Damage measurements. *Eng. Fract. Mech.* **1987**, *28*, 643–661. [CrossRef]
22. Tazan, C.C.; Hoefnagels, J.P.M.; Geers, M.G.D. Identification of the continuum damage parameter: An experimental challenge in modeling damage evolution. *Acta Mater.* **2012**, *60*, 3581–3589. [CrossRef]
23. Samuels, L.E. The nature of mechanically polished metal surfaces: The surface deformation produced by the abrasion and polishing of 70: 30 brass. *Wear* **1957**, *1*, 261. [CrossRef]
24. Zhong, Z.; Hung, N.P. Grinding of alumina/aluminum composites. *J. Mater. Process. Technol.* **2002**, *123*, 13–17. [CrossRef]
25. Isik, K.; Gerstein, G.; Clausmeyer, T.; Nürnberger, F.; Tekkaya, A.E.; Maier, H.J. Evaluation of Void Nucleation and Development during Plastic Deformation of Dual-Phase Steel DP600. *Steel Res. Int.* **2016**, *87*, 1583–1591. [CrossRef]
26. Maire, E.; Bouaziz, O.; Di Michiel, M.; Verdu, C. Initiation and growth of damage in a dual-phase steel observed by X-ray microtomography. *Acta Mater.* **2008**, *56*, 4954–4964. [CrossRef]
27. Ratcliffe, R.T. The measurement of small density changes in solids. *Br. J. Appl. Phys.* **1965**, *16*, 1193–1196. [CrossRef]
28. Schmitt, J.H.; Jalinier, J.M.; Baudalet, B. Analysis of damage and its influence on the plastic properties of copper. *J. Mater. Sci.* **1981**, *16*, 95–101. [CrossRef]
29. Bompard, D.P. Effets Endommageants de la Porosité sur la Propagation des Fissures Dans le Nickel Fritté. Ph.D. Thesis, Université de Technologie de Compiègne, Compiègne, France, 1986.
30. Lapovok, R. Damage evolution under severe plastic deformation. *Int. J. Fract.* **2002**, *115*, 159–172. [CrossRef]
31. Vedaldi, A.; Fulkerson, B. Vlfeat. In Proceedings of the International Conference on Multimedia—MM 2010, Firenze, Italy, 25–29 October 2010; ACM Press: New York, NY, USA, 2010; p. 1469.
32. Vincent, L.; Soille, P. Watersheds in digital spaces: An efficient algorithm based on immersion simulations. *IEEE Trans. Pattern Anal. Mach. Intell.* **1991**, *13*, 583–598. [CrossRef]
33. Kusche, C.; Reclik, T.; Freund, M.; Al-Samman, T.; Kerzel, U.; Korte-Kerzel, S. High-resolution, yet statistically relevant, analysis of damage in DP steel using artificial intelligence. *arXiv*, 2018; arXiv:1809.09657.
34. Rappoport, Z. *CRC Handbook of Tables for Organic Compound Identification*; CRC Press: Boca Raton, FL, USA, 1967.
35. Breitwieser, M. Bestimmungsmethoden der Dichte—IMETER. Available online: www.imeter.de (accessed on 15 January 2019).
36. Akeret, R. Versagensmechanismen beim Biegen von Aluminiumblechen und Grenzen der Biegefähigkeit. *Aluminium* **1978**, *54*, 117–123.
37. Meya, R.; Löbke, C.; Tekkaya, A.E. Stress state analysis of radial stress superposed bending. *Int. J. Precis. Eng. Manuf.* **2018**, *20*, 53–66. [CrossRef]

Publication #4

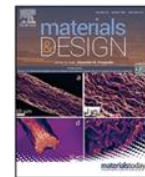
On the mechanical properties and deformation mechanisms of manganese sulphide inclusions

Carl F. Kusche, James S.K.-L. Gibson, Maximilian A. Wollenweber, Sandra Korte-Kerzel

Materials & Design, Volume 193, August 2020, 108801

<https://doi.org/10.1016/j.matdes.2020.108801>

For this publication, the candidate performed (in cooperation with James S.K.-L. Gibson as Supervisor and Maximilian A. Wollenweber as part of his bachelor's thesis that the candidate supervised) the experiments, evaluated the results and wrote the original manuscript as well as the final reviewed version of the manuscript together with James S.K.-L. Gibson.



On the mechanical properties and deformation mechanisms of manganese sulphide inclusions

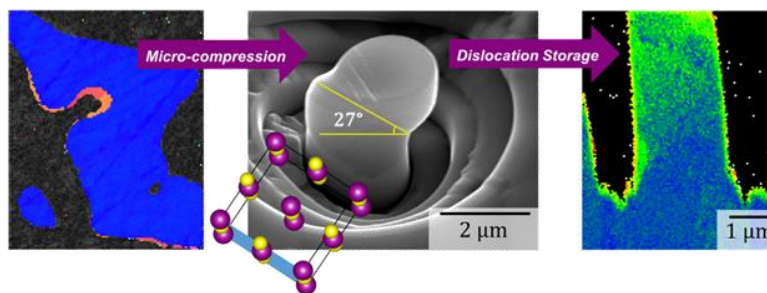
Carl F. Kusche^{*}, James S.K.-L. Gibson, Maximilian A. Wollenweber, Sandra Korte-Kerzel

Institute for Physical Metallurgy and Materials Physics, RWTH Aachen University, 52062 Aachen, Germany

HIGHLIGHTS

- MnS inclusions were studied with EBSD and micro-mechanics.
- Plastic deformation was primarily accommodated on $\{110\}\langle\bar{1}10\rangle$ slip systems.
- This was confirmed by EBSD cross-sections of the compressed micropillars.
- Additionally, for specific orientations, $\{100\}\langle\bar{1}10\rangle$ slip systems could be activated.

GRAPHICAL ABSTRACT



ARTICLE INFO

Article history:

Received 13 January 2020
Received in revised form 24 April 2020
Accepted 11 May 2020
Available online 13 May 2020

ABSTRACT

Manganese sulphide (MnS) inclusions are present in many steels. Some are deliberately introduced to increase machinability (Ånmark et al., 2015 [1]), for example in case-hardened 16MnCr5S. Others are present to the detriment of mechanical behaviour, causing anisotropic properties, a reduction in fatigue resistance as well as the formation of deformation-induced voids during forming. In order to improve the performance of MnS-containing steels, the mechanical properties and deformation mechanisms of these inclusions need to be understood. Due to their small size, micro-mechanical testing using nanoindentation and micropillar compression was performed in order to study the properties of MnS.

$\{110\}\langle\bar{1}10\rangle$ -type slip systems were, in accordance with literature, found as the primary slip system. For specific orientations with low Schmid factors for these systems, however, slip on $\{100\}$ planes could be activated in micropillar compression, and for both obtained systems, the critical resolved shear stresses for their activation was measured. These findings were subsequently confirmed by electron backscatter-diffraction on cross-sections of deformed micropillars.

© 2020 Published by Elsevier Ltd. This is an open access article under the CC BY-NC-ND license (<http://creativecommons.org/licenses/by-nc-nd/4.0/>).

1. Introduction

Modern steels seek to reduce the concentration of embrittling sulphur by adding higher-affinity elements such as manganese [1,2].

^{*} Corresponding author.
E-mail addresses: kusche@imm.rwth-aachen.de (C.F. Kusche),
korte-kerzel@imm.rwth-aachen.de (S. Korte-Kerzel).

While the resultant manganese sulphide (MnS) precipitates are effective in reducing the hot shortness caused by FeS, they nevertheless result in a detrimental influence on the mechanical properties. This influence manifests in particular in the form of anisotropic fatigue properties after hot rolling [3] or after forging [4]. An additional influence, the reduction of fatigue life, has been noted in railway steels [5], ultra-high strength steels [6], and high-strength 100Cr6 [7]. This last work by Gonzalez et al. is particularly striking, in that the majority of the

failures that occurred at high loads were due to the MnS precipitates, despite the presence of much harder TiCN precipitates, which would be expected to be greater stress concentrators. The shape of the precipitates appears to play a key role, with the anisotropy in the steel resulting from elongated precipitates after mechanical work. In contrast, in twelve steels formed by power metallurgical routes, the presence of MnS was seen to not impair the fatigue crack resistance, nor change the crack path during failure [8].

The detrimental behaviour to fatigue lifetime and therefore product performance in case-hardened steels used for bulk forming processes like extrusion can be explained by the MnS inclusions acting as a nucleation point for deformation-induced damage due to their mechanical contrast to the steel matrix [9]. For a damage-tolerant process and material design of these steels, it is therefore vital to understand the deformation behaviour of the MnS inclusions and include it in process and material modelling.

Due to their small size, there are very few works studying the mechanical properties of MnS precipitates. Bulk crystals of MnS with the typical rock-salt (NaCl) structure were studied by Chao et al. [10], who determined a primary slip system of $\{110\}\langle\bar{1}10\rangle$, with secondary slip on $\{111\}$ planes. Cleavage was observed on $\{100\}$ planes, with cleavage along $\{110\}$ planes observed when indentation was performed due to dislocation intersection on $\{110\}$ planes [10]. This primary slip system has also been reported for many ionic compounds with this rock-salt structure in a review by Gilman, including MgO, LiF, NaCl, KCl, AgBr, and more [11].

More recent work by Zhou et al. [12] studied MnS crystals deformed by hot rolling the parent steel. Aberration-corrected STEM was used to observe the Burgers vector and slip plane of a dislocation in MnS, which were determined as $\frac{a}{2}[\bar{1}10]$ and $\{110\}$, respectively. A deformation twin was also observed on $\{111\}$ planes via $\frac{a}{6}\langle 112 \rangle$ dislocations, which are explained to glide via the synchroshear mechanism. This was supported by DFT calculations that demonstrated this would be energetically favourable. Importantly, the DFT calculations also showed that synchroshear is not favourable in PbS or MgO, as the ionicity of the crystal is, as noted by the authors, critical in determining the deformation behaviour of ionic crystals, even where they share the same crystal structure.

To further study the deformation mechanisms of MnS, and to determine its mechanical properties, micro-mechanical testing techniques are very well-suited. In particular, micropillar compression is ideal for isolating specific slip planes to be tested under uniaxial conditions, while preventing fracture in even very brittle materials [13]. This is due to a combination of the reduction of the specimen volume to below the critical flaw size in the material with a simultaneous reduction in the stored elastic energy in the deformed specimen [14]. A recent review of the technique [13] demonstrates the applicability to a vast range of materials, including similar ionic crystals such as MgO [15,16] and LiF [17], with Zou et al. testing NaCl, KCl, LiF and MgO [18].

Here, we use micropillar compression and electron backscatter diffraction (EBSD) to study the plasticity mechanisms in MnS precipitates and measure the indentation modulus, hardness and underlying critical stresses. Ultimately, this information may be used to facilitate damage modelling and improvement of the processes associated with damage-controlled forming of steels containing MnS precipitates [19]. A second goal is to further the general understanding of how plastic deformation takes place in macroscopically brittle ionic crystals.

2. Materials and methods

To obtain MnS inclusions of sufficient size suitable for nanomechanical testing by both indentation and micropillar compression, an as-cast material was used as the typical directional morphology in extruded material makes it impossible to assure a plastic zone of the indents entirely in the inclusion. Nanoindentation was performed using an iNano nanoindenter (Nanomechanics Inc., TN, USA) and a diamond Berkovich tip, calibrated prior to indentation on fused silica according to the Oliver-Pharr method [20]. Nanoindentation to obtain hardness and modulus values was carried out to a final depth of 300 nm because of an average inclusion size of 20 μm , in order to minimise the influence of the steel matrix on the mechanical data. The calculated values were taken at the final penetration depth, to reduce size effects in these shallow indents.

After indentation, the indented area was checked with scanning electron (SE) imaging and indents touching the steel-MnS interface were excluded, leaving 31 indents in the MnS at a constant strain rate of 10^{-3} s^{-1} . Strain rate jump tests were additionally performed with two jumps from a base indentation strain rate of 10^{-3} s^{-1} to 10^{-4} s^{-1} and 10^{-5} s^{-1} . The same post-mortem examination for validity was performed, leaving 14 valid indents.

SEM observations of the microstructure, EBSD maps and micropillar milling were all carried out using an FEI Helios Dual-Beam FIB equipped with an EDAX EBSD detector (EDAX, NJ, USA). Micropillars were milled with a coarse beam current of 9.3 nA for the initial cuts, followed by annular milling at successively lower beam currents to achieve the final dimensions at a beam current of 80 pA. All micropillars have nominal dimensions of a 2 μm diameter and a 4 μm height, although the exact dimensions of each pillar were used in the calculations of stress and strain. A total of 37 pillars were compressed, of which only five showed clear, unambiguous slip traces as required for quantitative evaluations of critical resolved shear stress. Of these five, the first micropillar (micropillar 1 in Table 1) was compressed under displacement control at a constant rate of 10 nm/s. This method was however found to give a poor success rate in terms of analysable pillars, therefore the remaining pillars were tested under a constant loading rate of 0.1 mN/s. This resulted in a minor decrease in the strain rate in the elastic region: $5 \times 10^{-4} \text{ s}^{-1}$ for pillar 1 under displacement control and $2.5 \times 10^{-4} \text{ s}^{-1}$ for the remaining pillars.

In order to confirm the active slip systems, site-specific lift-out of the micropillars via focused ion beam (FIB) was performed, followed by

Table 1
Evaluated micropillars with activated slip systems, Schmid factors and critical resolved shear stresses (CRSS) from SE slip line analysis.

Micropillar	Compression axis orientation	Primary slip system	CRSS (MPa)	Schmid factor
1	(55 14 82)	(001)[110]	130.8	0.40
2	(25 $\bar{1}8$ 95)	(001)[110]	134.9	0.42
3	(6 61 79)	(0 $\bar{1}$ 1)[011]	72.7	0.31
4	(6 61 79)	(0 $\bar{1}$ 1)[011]	70.3	0.31
5	(6 61 79)	(0 $\bar{1}$ 1)[011]	68.5	0.31

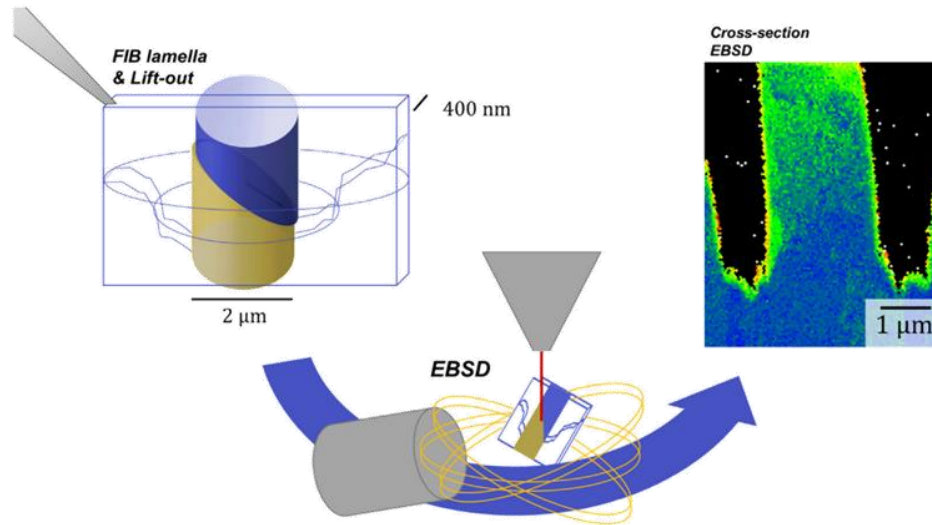


Fig. 1. Lift-out of focused ion beam (FIB)-prepared lamella of deformed micropillar with subsequent EBSD investigation of the cross-section perpendicular to the slip plane (schematic).

thinning the pillar into a lamella on which EBSD was carried out, as shown in Fig. 1.

3. Results

A typical inclusion prior to indentation can be seen in Fig. 2a, with the load-displacement data from one of the 31 constant strain rate indents shown in Fig. 2b. The hardness-depth and Young's modulus-

depth curves are shown in Fig. 2c and d, respectively. An average hardness of 2.4 ± 0.2 GPa and modulus of 121 ± 10 GPa was measured, from data taken at 300 nm.

The hardness data from the strain rate jump tests are shown in Fig. 3a, with Fig. 3b displaying the corresponding modulus. The strain-rate sensitivity and activation volume were determined according to the equations of Mathur et al. [21]. Here it is also assumed that dislocation motion is subject to a large Peierls stress, and

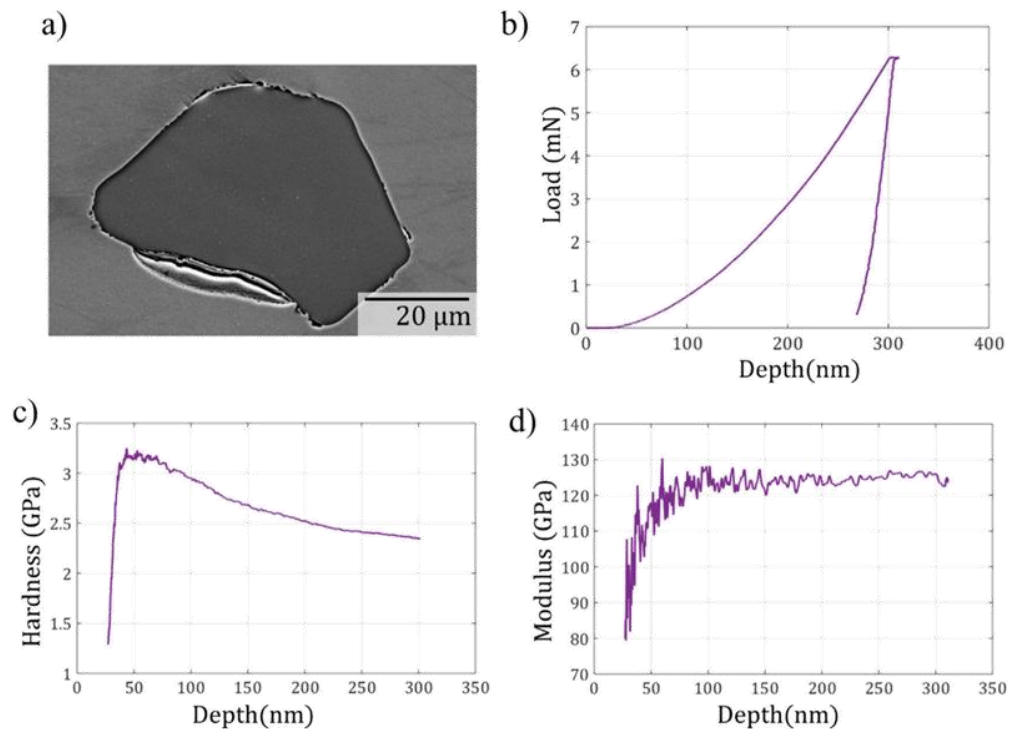


Fig. 2. (a) Typical MnS precipitate in the investigated as-cast material, (b) load-displacement curve obtained from nanoindentation, (c) hardness with depth and (d) Young's modulus with depth from continuous stiffness measurements (CSM) during indentation.

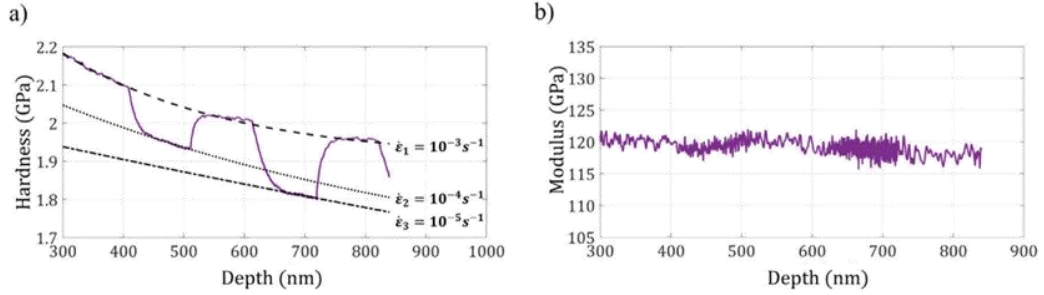


Fig. 3. (a) Hardness-depth data obtained from nanoindentation strain-rate jump tests, with curves fitted to the constant strain-rate sections in order to allow calculation of the hardness change at the strain jump. (b) Modulus-depth data obtained from the jump test in (a).

indentation hardness is converted to shear stress by a simple factor of $H/6$. This conversion factor is a combination of the Tabor conversion between (tensile) yield stress and hardness ($\sigma_y = \frac{H}{3}$ [22]) combined with a simple Tresca yield criterion that states $\tau_y = \frac{\sigma_y}{2}$.

The strain rate sensitivity, m , was subsequently calculated to be 0.0284 ± 0.0016 . Assuming a lattice parameter of 5.225 \AA [23], the commonly observed $\frac{a}{2} \langle 011 \rangle$ Burgers vector in the rock salt structure has a length of 3.7 \AA , and thus the activation volume was determined to be $10.4 \pm 5 b^3$.

It can be seen in the hardness data from both the constant strain rate tests (Fig. 2c) and the strain rate jump tests (Fig. 3a) that an indentation size effect is present, with the hardness decreasing with indentation depth. Given the consistent modulus data in both cases, it is presumed that this is simply due to an increased density of geometrically necessary dislocations at small depth (a Nix-Gao effect [24]), rather than any influences of the steel substrate.

A typical micropillar, in this case oriented with a maximum Schmid factor on $\{100\}$ planes, can be seen in Fig. 4a, with the slip lines on the surface of the pillar implying that slip has indeed occurred on these planes. To determine the slip plane, the measured angle on the 45° tilted images was corrected using the tilt correction given in Eq. (1). The

obtained angles are then compared with the elementary cells from initial EBSD measurements.

$$\gamma_{90} = \arctan(\tan(\gamma_{45}) \cdot \sqrt{2}) \quad (1)$$

Equally, for the pillars with the primarily activated slip system of $\{110\}$ type, slip lines were observed on the deformed pillars and attributed to the corresponding lattice planes as seen in Fig. 4b. To determine a value of stress from which the critical resolved shear stress (CRSS) could be determined, an $R_{p0.2}$ criterion was applied, i.e. the stress at 0.2% plastic strain was taken as the yield stress. This point is marked on the load-displacement curve in Fig. 4c by a black point at 325 MPa, corresponding to a load of 1.02 mN. The difficulty of identifying the yield point, especially in micropillars with identified $\{110\}$ slip planes, points to the existence of slip on multiple planes, leading to strain hardening effects. As in SE observations, there was no clear evidence of secondary slip planes from slip traces at the surface, further investigations were carried out with lift-out EBSD (compare Fig. 1) to characterise the deformation mechanisms.

The EBSD performed on a thinned pillar to confirm slip along $\{110\}$ is presented in Fig. 5. The SE image previously shown in Fig. 4b shows a slip trace for an $(0\bar{1}1)$ plane on the side of the micropillar inclined at

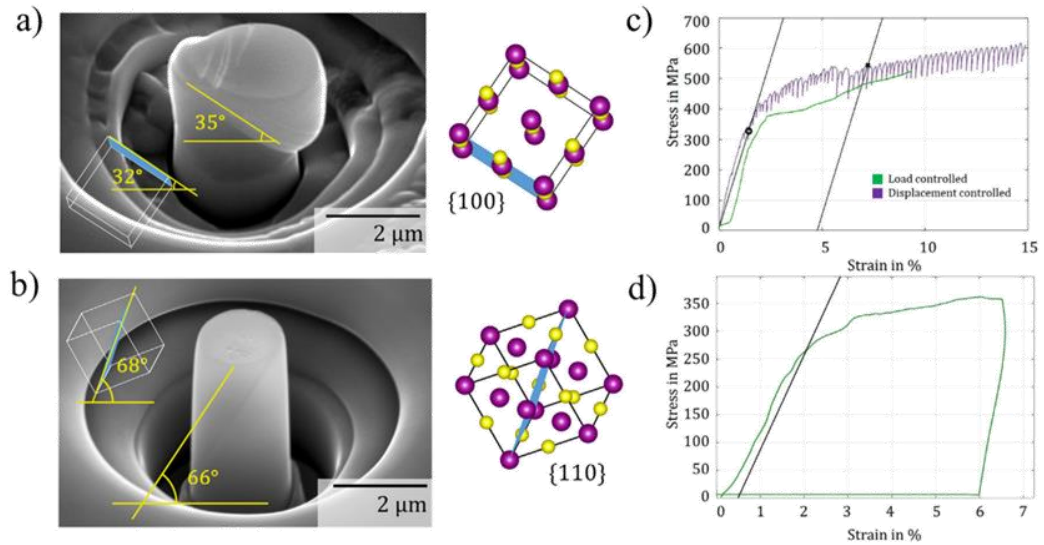


Fig. 4. (a) Compressed micropillar and crystal orientation, indicating that slip has occurred along $\{100\}$ planes. (b) Compressed micropillar and crystal orientation, indicating that slip has occurred along $\{110\}$ planes. (c) Stress-strain curves from the compressed micropillars with slip along $\{100\}$ planes (pillar 1 under displacement control, pillar 2 under load control). The load at yield, as defined from a 0.2% offset strain, is marked with a dot, the stress at 5% plastic strain marked with a cross. The angles measured on the pillars have been corrected for 45° tilt. (d) Typical stress-strain curve from a compressed micropillar with slip along $\{110\}$ planes, the 0.2% offset strain is again shown.

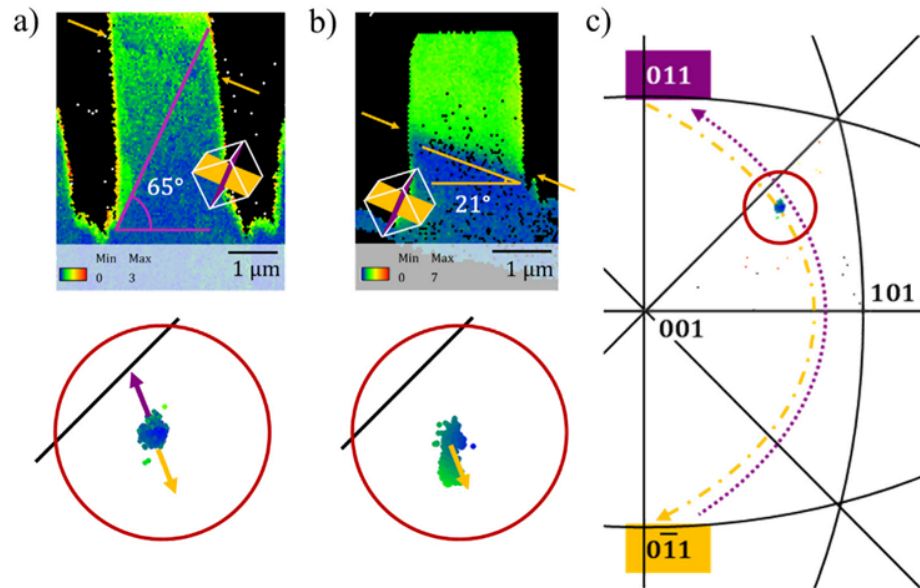


Fig. 5. (a) EBSD of a compressed micropillar showing angular misorientation from the undeformed material well below the pillar, with two active $\{110\}$ slip planes visible, with no pronounced crystal rotation visible in the IPF mapping below. (b) EBSD of a compressed micropillar of the same orientation, showing single slip on a single $\{110\}\bar{1}10$ -type slip system, with the corresponding crystal rotation visible in the enlarged inverse pole figure segment (c) Inverse pole figure showing the orientation of the compression axis in the same pillar as shown in (a), with corresponding change in orientation due to two activated $\{110\}\bar{1}10$ -type slip systems, the red circle marks the enlarged areas in (a) and (b).

66° to the image horizontal. This is marked by the purple line in the EBSD cross section in Fig. 5a, and indeed it can be seen that the crystal misorientation relative to the undeformed material is concentrated above this line. With this slip system activated, the crystal orientation is expected to move towards the $(0\bar{1}1)$ slip plane normal during compression, as shown in Fig. 5b. However, a second $\{110\}$ -type plane can be seen by the misorientation in the EBSD data in Fig. 5a, in this case the (011) -plane, marked with the yellow arrows. The combination of these two slip systems that have an opposing direction of crystal rotation leads to a barely visible crystal rotation. This is depicted in Fig. 5c, in line with the observed data. Note that is a fairly special situation: the fact that the two slip systems have identical Schmid factors (as the slip direction of one system is the slip plane normal of the other) means that both systems operate immediately, and equally, once slip begins. Although source stochasticity can dominate the onset of slip in small-scale testing, this does not appear to be the case here based on the relatively steady increase in flow stress measured. These equally-operating slip systems are then combined with the fact that the initial crystal orientation is such that the rotation of the slip plane normal for each system “cancel out” and the system is effectively left in a local, unstable equilibrium, rather than rotating towards a zone containing the normal to both planes: $[100]$.

4. Discussion

The nanoindentation tests determined an average hardness of 2.4 GPa, and fitting a Nix-Gao curve to the hardness data (Fig. 2c) determines a bulk hardness of 2.0 GPa. This is fairly close to the value of ~1.6 GPa for stoichiometric MnS measured by Matsuno by Vickers indentation [25]. The residual discrepancy could be due to the precipitates investigated here having some small impurity content; Matsuno also shows for example that 0.39 wt% Ca increases the hardness of MnS to ~2.8 GPa. The value of 121 GPa determined here for the indentation modulus is very close to the calculated value of 120 GPa [26] and matches well with values for sulphides in steel collated by Murakami

of 69–138 GPa [27]. The strain rate sensitivity, m , of 0.0284 is relatively high, comparable to that of nanocrystalline nickel [28]. Hence, the corresponding activation volume is only $10.4 b^3$, implying that deformation is limited by the lattice resistance. Note that despite the work-hardening taking place in a nanoindentation test, it is nevertheless possible to determine such a mechanism, as these tests are designed to differentiate the rate-limiting step of plasticity. This has been demonstrated on BCC tungsten [29] and chromium [30], as well as complex intermetallics such as $Mg_{17}Al_{12}$ [21]. That deformation is controlled by lattice resistance is not unsurprising for a hard, ionic crystal; a similar limitation is indeed reported in magnesium oxide [31,32]. Haasen [33] also shows a Peierls mechanism controls plasticity on $\{100\}$ planes in NaCl and KCl at room temperature, and on $\{110\}$ planes in PbS this mechanism operates all the way to 500 °C. Finally, the value of activation volume calculated here is very close to that of $11.4 b^3$ as determined by Soler et al. measured via strain-rate variations of LiF micropillars at room temperature [34].

Zou et al. tested the size effect in pillars of NaCl, KCl, LiF and MgO along $\langle 100 \rangle$ directions, such that the four primary slip systems were active [18]. Their plots of resolved shear stress at 5% strain normalised by the shear modulus show two groups, with values of 0.002 for NaCl and KCl and values of 0.009 for LiF and MgO, for normalised pillar diameters comparable to those tested here (diameter/Burgers vector ~5400). This was attributed to the higher defect formation energies in LiF and MgO leading to less residual damage from the FIB-milling [18]. For MnS, the shear modulus, G , is 48.1 GPa [26], and the micropillar data from the “soft” micropillars, evaluated in an analogous way to Fig. 4c, corresponds to a stress at 5% strain of 322 MPa, i.e. a resolved shear stress of 119 MPa, giving an RSS/ G of ~0.003. Note this value is higher than those detailed in Table 1 due to the work hardening present by 5% strain. MnS prepared by FIB milling therefore yields critical stress values in good agreement with those measured elsewhere on the above-mentioned ionic crystals. However, as the values in LiF have been shown to vary between researchers [18,34], whether the value of RSS/ G is strongly influenced by FIB-induced damage, material purity or other effects cannot be concluded here.

The CRSS for the primary and secondary slip systems have been determined as 70.5 ± 2.1 MPa and 132.8 ± 2.9 MPa, respectively. As mentioned, when comparing with the work of Zou [18], these are comparable with those in LiF and MgO for similarly-sized micropillars. To compare these data with the hardness data from nanoindentation, it has been shown that the indentation hardness can be divided by a constraint factor of 2.8 to determine a flow stress at 8% plastic strain, which can be compared with the compression data [35]. The majority of the pillars compressed in this work were only compressed to ~5% strain, as additional deformation precluded the clear identification of the operating slip systems. At this 5% strain level, the average flow stress of all the micropillars is 425 MPa, compared with an indentation yield stress of 860 MPa. Assuming similar work-hardening rates for all slip systems as shown in Fig. 4c, an 8% strain level results in a stress around 10% higher than at 5%, i.e. the micropillar flow stress comparable to the indentation flow stress can be considered to be around 470 MPa. The higher value from the indentation yield stress likely comes from the additional work-hardening in nanoindentation due to a larger number of intersecting active slip planes compared to uniaxial deformation. Additionally, indentation has been shown to activate additional, presumably harder slip systems (e.g. $\{011\}\{211\}$) [36] due to the strong and complex stress field of the indenter. Similar mechanisms have been seen in work on other plastically-anisotropic crystals (CMSX-4, a nickel superalloy) [37], which showed that there can resultantly be substantial differences between the mechanical responses from indentation and uniaxial loading.

In both cases, these flow stresses are clearly somewhat higher than the CRSS values for the primary and secondary slip systems. With $\{110\}\{110\}$ -type slip systems, two individual systems always have equal Schmid factors, due to the slip directions being identical to the slip plane normal of another $\{110\}$ plane. Therefore, double slip is expected and observed in these pillars, shown directly via the lift-out EBSD in Fig. 5a, which confirms the activation of two $\{110\}\{110\}$ -type slip systems. The combined crystal rotation due to the two activated systems additionally matches the practically stable crystal orientation visible in the inverse pole figure given in Fig. 5c.

It is this activation of multiple slip systems that leads directly to the work hardening occurring during compression, as depicted in the compression data in Fig. 4d. In this curve, the peak stress in the test reaches 140% of that at yield. This cannot be attributed to 'hardening' from an increase in cross-sectional area in the micropillars, either from plastic deformation, or from the taper in the pillar. Based on the SEM image (Fig. 4b), after compression the lowest part of the pillar has a 0.1 μm greater diameter than the top, equivalent to a mere 10% increase in area. In other words, if this distance is taken as the new diameter and the pillar is assumed to still be circular to give a geometrical upper-bound, the peak stress would only be expected to reach 110% of the yield stress if no work hardening took place. This difference, and the direct evidence of multiple operating slip systems in the EBSD data, leads to the conclusion that these intersecting systems contribute to the observed work hardening. For pillars where only a single slip system operates (Fig. 4a and the corresponding stress-strain curve in Fig. 4c), this difference is not as stark. Taking the pillar diameter just underneath the displaced upper part (2.7 μm) as an average value leads to a corresponding increase in area to 180% of the initial area. This is almost identical to the difference between the yield stress (330 MPa) and the peak stress in the test (590 MPa).

It has been shown for several materials that the magnitude of the size effect depends on the intrinsic resistance to dislocation motion determined by any length scale much smaller than the pillar length, e.g. the length of a kink in lattice resistance controlled hard crystals [13,15] and the precipitate [38], particle [39] or dislocation [40] spacing in hardened or pre-deformed alloys. As a result, the size effect is also slip-system dependent in the strongly anisotropic ionic crystals. LiF and MgO micropillars with a range of diameters were compressed along $\{111\}$ directions by Soler, Korte and co-workers, thereby

suppressing slip on the primary, soft slip systems [15,41]. No significant effect of pillar size on the shear yield stress was subsequently seen, unlike the pillars oriented for slip on the soft slip systems [15,41,42]. Korte and Clegg proposed that when size effects in micropillars empirically follow the equation $\tau_{\text{CRSS}} = \tau_0 + Kd^n$ [15], with the second term commonly associated phenomena of truncated dislocations and their sources [43], then higher values of the bulk shear yield stress, τ_0 , lead to a weakening of the size effect, exactly as described above for the experiments on the hard and soft slip systems. Similar trends would therefore be expected in the case of MnS, however, as the properties of MnS inclusions in steels are of interest here, which are of comparable size to the pillars and indents, the stresses measured here are directly relevant to those encountered in application. As such, no size effect studies were carried out in this work.

The activation of $\{100\}$ planes was also observed TEM after micropillar compression experiments of MgO [15,41]. Slip on $\{100\}$ planes in the rock-salt structure is in itself not unusual. Gilman and Johnston [44] showed that screw dislocations can cross-slip and glide on $\{100\}$ planes in LiF, still with a $\langle 110 \rangle$ glide direction, which is expected from the charges dominating the process of slip in this crystal structure. While the obtained CRSS of this slip system in MnS is unsurprisingly significantly higher than the one for the primary $\{110\}\{110\}$ slip system - 132 MPa compared with 72 MPa - this difference is far less pronounced than in MgO or PbS at room temperature [45], presumably due to the thermally activated softening of the hard slip system which does diminish to similar stress levels around room temperature in KCl, KBr and KI [46]. Consequently, both the soft and hard system could be observed here, as a difference in Schmid factor of the order of 2 (here $0.40_{\{100\}}/0.18_{\{110\}}$ in the pillar shown in Fig. 4b) is sufficient. This suggests that MnS inclusions are moderately anisotropic at room temperature and that at slightly more elevated temperatures, they should become largely isotropic in behaviour with similar critical resolved shear stresses on the $\{110\}$ and $\{100\}$ planes.

It should be noted that under most application conditions, the loading conditions are likely not as straightforward as those investigated here, although simple forming operations such as rolling may well be close. As to what effect these differences have is not fully clear. In one study on the fatigue strength of Al-Si alloys, uniaxial loading proved to be a 'worst-case' scenario, with the critical defect size for $R = -1$ loading being 3.5 times smaller in uniaxial tests compared to pure torsion [5]. However, in modelling work comparing damage evolution in biaxial vs triaxial loading, damage rates were significantly higher in triaxial loading [47]. Nevertheless, MnS inclusions have been shown to result in poorer, and isotropic, fatigue behaviour. This is ascribed to MnS-steel interface decohesion after forming and the resultant presence of elongated cracks in the microstructure [48] [49], rather than through deformation of the MnS precipitates themselves. Resultantly, the importance of these findings - i.e. the operating deformation mechanisms and their critical stresses - is for the development of crystal-plasticity based models of MnS-containing steels. By determining the properties of the inclusions, this enables the design of forming operations that produce more spherical precipitates, or to understand the evolving stresses at MnS-steel interfaces to ultimately improve their strength. In both cases, this ultimately results in improved properties of the parent steel.

5. Conclusions

- Nanoindentation and micropillar compression tests were carried out on MnS precipitates in order to determine mechanical properties relevant for the interpretation and modelling deformation in and around MnS inclusions in steels.
- A combination of constant strain-rate and strain-rate jump tests determined an average hardness of 2.4 ± 0.2 GPa, a modulus of 121 ± 10 GPa, a strain-rate sensitivity of 0.0284 ± 0.0016 , and an activation volume of 10.4 ± 5 b³.

- Corresponding with literature data, $\{110\}\{110\}$ was observed as the primary slip system, the critical resolved shear stress for its activation was found to be 70.5 ± 2.1 MPa.
- $\{100\}\{110\}$ was observed as a second active slip system at a higher CRSS of 132.8 ± 2.9 MPa.
- EBSD measurements confirmed slip on two separate $\{110\}\{110\}$ systems, which corresponds to the observed crystal rotation and the strain hardening during compression.

CRedit authorship contribution statement

Carl F. Kusche: Investigation, Data curation, Writing - original draft, Writing - review & editing. **James S.K.-L. Gibson:** Investigation, Writing - original draft, Supervision, Writing - review & editing. **Maximilian A. Wollenweber:** Investigation, Writing - review & editing. **Sandra Korte-Kerzel:** Conceptualization, Supervision, Project administration, Funding acquisition, Writing - review & editing.

Declaration of competing interest

No conflict of interest exists.

Acknowledgements

Funding from the Deutsche Forschungsgemeinschaft (DFG) within project B02 of TRR188 is gratefully acknowledged. The initial material was provided from IEHK, RWTH Aachen University, synthesised in SFB 761 funded by the DFG. We thank Mr. Martin Heller from the IMM, RWTH Aachen for assistance with the pillar lift-out.

References

- [1] N. Anmark, A. Karasev, P.G. Jönsson, The effect of different non-metallic inclusions on the machinability of steels, *Materials* 8 (2) (2015) 751–783.
- [2] R. Diederichs, W. Bleck, Modelling of manganese sulphide formation during solidification, part I: description of MnS formation parameters, *Steel Research International* 77 (3) (2006) 202–209.
- [3] J. Schumacher, H. Bomas, H.W. Zoch, Microstructure and mechanical properties of sulphur-alloyed spray-formed steels, *Mater. Werkst.* 41 (7) (2010) 585–596.
- [4] E. Pessard, et al., Modelling the role of non-metallic inclusions on the anisotropic fatigue behaviour of forged steel, *Int. J. Fatigue* 33 (4) (2011) 568–577.
- [5] D. Kalisz, et al., Computer simulation of microsegregation of sulphur and manganese and formation of MnS inclusions while casting rail steel, *Arch. Metall. Mater.* 61 (4) (2016) 1939–1944.
- [6] H. Tervo, et al., Effect of impurity level and inclusions on the ductility and toughness of an ultra-high-strength steel, *Materials Science and Engineering A-Structural Materials Properties Microstructure and Processing* 697 (2017) 184–193.
- [7] L. Gonzalez, et al., Influence of non-metallic second phases on fatigue behaviour of high strength steel components, *Rev. Metal.* 41 (1) (2005) 45–52.
- [8] H. Drar, Metallographic and fractographic examination of fatigue loaded PM-steel with and without MnS additive, *Mater. Charact.* 45 (3) (2000) 211–220.
- [9] A.E. Tekkaya, et al., Forming-induced damage and its effects on product properties, *CIRP Ann.* 66 (1) (2017) 281–284.
- [10] H.-c. Chao, Lawrence H. van Vlack, F. Oberlin, Lars Thomassen, Inclusion Deformation : I : The Mechanism of Fracture and Deformation in MnS, 1962.
- [11] J.J. Gilman, Mechanical behavior of ionic crystal, *Progress in Ceramic Science* 146 (1961).
- [12] Y.T. Zhou, et al., Atomic-scale configurations of synchro-shear-induced deformation twins in the ionic MnS crystal, *Sci. Rep.* 4 (2014).
- [13] S. Korte-Kerzel, Microcompression of brittle and anisotropic crystals: recent advances and current challenges in studying plasticity in hard materials, *Mrs Communications* 7 (2) (2017) 109–120.
- [14] F. Östlund, et al., Ductile-brittle transition in micropillar compression of GaAs at room temperature, *Philos. Mag.* 91 (7–9) (2011) 1190–1199.
- [15] S. Korte, W.J. Clegg, Discussion of the dependence of the effect of size on the yield stress in hard materials studied by microcompression of MgO, *Philos. Mag.* 91 (7–9) (2011) 1150–1162.
- [16] S. Korte, et al., Three-dimensional electron backscattered diffraction analysis of deformation in MgO micropillars, *Acta Mater.* 59 (19) (2011) 7241–7254.
- [17] R. Soler, et al., Micropillar compression of LiF $[111]$ single crystals: effect of size, ion irradiation and misorientation, *Int. J. Plast.* 36 (2012) 50–63.
- [18] Y. Zou, R. Spolenak, Size-dependent plasticity in micron- and submicron-sized ionic crystals, *Philos. Mag. Lett.* 93 (7) (2013) 431–438.
- [19] R. Meya, et al., Global and high-resolution damage quantification in dual-phase steel bending samples with varying stress states, *Metals* 9 (3) (2019).
- [20] W.C. Oliver, G.M. Pharr, Improved technique for determining hardness and elastic modulus using load and displacement sensing indentation experiments, *J. Mater. Res.* 7 (6) (1992) 1564–1580.
- [21] H.N. Mathur, V. Maier-Kiener, S. Korte-Kerzel, Deformation in the γ -Mg17Al12 phase at 25–278 °C, *Acta Mater.* 113 (2016) 221–229.
- [22] D. Tabor, The hardness of solids, *Reviews of Physics in Technology* 1 (3) (1970) 145–179.
- [23] J. Guo, et al., Effect of sulfur content on the properties and MnS morphologies of DH36 structural steel, *Metals* 8 (11) (2018) 945.
- [24] W.D. Nix, H. Gao, Indentation size effects in crystalline materials: a law for strain gradient plasticity, *Journal of the Mechanics and Physics of Solids* 46 (3) (1998) 411–425.
- [25] F. Matsumo, S.-i. Nishikida, H. Ikesaki, Mechanical properties of manganese sulphides in the temperature range between room temperature and 1000° C, *Transactions of the Iron and Steel Institute of Japan* 25 (9) (1985) 989–998.
- [26] O. Kavci, S. Cabuk, First-principles study of structural stability, elastic and dynamical properties of MnS, *Comput. Mater. Sci.* 95 (2014) 99–105.
- [27] Y. Murakami, *Metal Fatigue: Effects of Small Defects and Nonmetallic Inclusions*, Elsevier Science, 2002.
- [28] V. Maier, et al., Nanoindentation strain-rate jump tests for determining the local strain-rate sensitivity in nanocrystalline Ni and ultrafine-grained Al, *J. Mater. Res.* 26 (11) (2011) 1421–1430.
- [29] V. Maier, et al., Microstructure-dependent deformation behaviour of bcc-metals – indentation size effect and strain rate sensitivity, *Philos. Mag.* 95 (16–18) (2015) 1766–1779.
- [30] V. Maier-Kiener, K. Durst, Advanced nanoindentation testing for studying strain-rate sensitivity and activation volume, *JOM* 69 (11) (2017) 2246–2255.
- [31] J. Amodeo, et al., Multiscale modelling of MgO plasticity, *Acta Mater.* 59 (6) (2011) 2291–2301.
- [32] R. Reali, et al., Modeling plasticity of MgO by 2.5D dislocation dynamics simulations, *Mater. Sci. Eng. A* 690 (2017) 52–61.
- [33] P. Haasen, Dislocations and the plasticity of ionic crystals, *Mater. Sci. Technol.* 1 (12) (1985) 1013–1024.
- [34] R. Soler, et al., Understanding size effects on the strength of single crystals through high-temperature micropillar compression, *Acta Mater.* 81 (2014) 50–57.
- [35] C. Zenk, et al., Low temperature deformation of MoSi2 and the effect of Ta, Nb and Al as alloying elements, *Acta Mater.* 181 (2019) 385–398.
- [36] C. Tromas, J.C. Girard, J. Woignard, Study by atomic force microscopy of elementary deformation mechanisms involved in low load indentations in MgO crystals, *Philosophical Magazine A* 80 (10) (2000) 2325–2335.
- [37] J.S.K.-L. Gibson, et al., On extracting mechanical properties from nanoindentation at temperatures up to 1000° C, *Extreme Mechanics Letters* 17 (2017) 43–49.
- [38] M.D. Uchic, et al., Sample dimensions influence strength and crystal plasticity, *Science* 305 (5686) (2004) 986–989.
- [39] B. Girault, et al., Strength effects in micropillars of a dispersion strengthened superalloy, *Adv. Eng. Mater.* 12 (5) (2010) 385–388.
- [40] C. Frick, et al., Size effect on strength and strain hardening of small-scale $[111]$ nickel compression pillars, *Mater. Sci. Eng. A* 489 (1–2) (2008) 319–329.
- [41] R. Soler, et al., Micropillar compression of LiF $[111]$ single crystals: effect of size, ion irradiation and misorientation, *Int. J. Plast.* 36 (2012) 50–63.
- [42] Y. Zou, R. Spolenak, Size-dependent plasticity in micron- and submicron-sized ionic crystals, *Philos. Mag. Lett.* 93 (7) (2013) 431–438.
- [43] T.A. Parthasarathy, et al., Contribution to size effect of yield strength from the stochasticity of dislocation source lengths in finite samples, *Scr. Mater.* 56 (4) (2007) 313–316.
- [44] J.J. Gilman, W.G. Johnston, Behavior of individual dislocations in strain-hardened LiF crystals, *J. Appl. Phys.* 31 (4) (1960) 687–692.
- [45] P. Haasen, C. Barthel, T. Suzuki, Choice of slip system and Peierls stresses in the NaCl structure, *Dislocations in solids* (1985) 455.
- [46] W. Skrotzki, P. Haasen, Hardening mechanisms of ionic crystals on $\{110\}$ and $\{100\}$ slip planes, *Le Journal de Physique Colloques* 42 (C3) (1981) (p. C3-119-C3-148).
- [47] C.J.A. Thomson, et al., Modeling void nucleation and growth within periodic clusters of particles, *Journal of the Mechanics and Physics of Solids* 47 (1) (1999) 1–26.
- [48] C. Temmel, N.-G. Ingesten, B. Karlsson, Fatigue anisotropy in cross-rolled, hardened medium carbon steel resulting from MnS inclusions, *Metall. Mater. Trans. A* 37 (10) (2006) 2995–3007.
- [49] A. Kaijalainen, et al., Effect of inclusions on the properties of ultra-high strength low-alloy steel with a martensitic-bainitic microstructure, *Proceedings of the 8th International Conference on Clean Steel*, 2012.

Bibliography

References

- [1] W. Bleck, S. Papaefthymiou, A. Frehn, Microstructure and Tensile Properties in Dual Phase and Trip Steels, *Steel research int.* 75(11) (2004) 704-710.
- [2] H. Ghadbeigi, C. Pinna, S. Celotto, J.R. Yates, Local plastic strain evolution in a high strength dual-phase steel, *Materials Science and Engineering* 527 (2010) 5023-5032.
- [3] J.P.M. Hoefnagels, C.C. Tasan, F. Maresca, F.J. Peters, V.G. Kouznetsova, Retardation of plastic instability via damage-enabled microstrain delocalization, *Journal of Materials Science* 50 (2015) 6882-6897.
- [4] M. Avrami, Kinetics of phase change. II transformation-time relations for random distribution of nuclei, *The Journal of Chemical Physics* 8(2) (1940) 212-224.
- [5] A.N. Kolmogorov, On the statistical theory of the crystallization of metals, *J. Bull. Acad. Sci. USSR* 1(3) (1937) 355-359.
- [6] G. Gottstein, D.A. Molodov, L.S. Shvindlerman, Grain boundary migration in metals: Recent developments, *Interface Science* 6(1-2) (1998) 7-22.
- [7] G. Gottstein, T. Al Samman, Texture development in pure Mg and Mg alloy AZ31, *Materials Science Forum, Trans Tech Publ*, 2005, pp. 623-632.
- [8] N. Peranio, F. Roters, D. Raabe, Microstructure evolution during recrystallization in dual-phase steels, *Materials Science Forum, Trans Tech Publ*, 2012, pp. 13-22.
- [9] J. Kang, Y. Ososkov, J.D. Embury, D.S. Wilkinson, Digital image correlation studies for microscopic strain distribution and damage in dual phase steels, *Scripta Materialia* 56 (2007) 999-1002.
- [10] O.B. C. Landron, E. Maire, J. Adrien, Characterization and modeling of void nucleation by interface decohesion in dual phase steels, *Scripta Materialia* 63 (2010) 973-996.
- [11] K. Moehring, F. Walther, Load Direction-Dependent Influence of Forming-Induced Initial Damage on the Fatigue Performance of 16MnCrS5 Steel, *Materials & Design* 13(12) (2020) 2680.
- [12] T.M. E. Ahmad, K. Ali, J.I. Akhter, Effect of Microvoid Formation on the Tensile Properties of Dual-Phase Steel, *JMPEG* 9 (2000) 306-310.
- [13] A.E. Tekkaya, N.B. Khalifa, O. Hering, R. Meys, S. Myslicki, F. Walther, Forming-induced damage and its effects on product properties, *CIRP Annals* 66(1) (2017) 281-284.
- [14] T. de Geus, J. van Duuren, R. Peerlings, M. Geers, Fracture initiation in multi-phase materials: A statistical characterization of microstructural damage sites, *Materials Science and Engineering: A* 673 (2016) 551-556.
- [15] J.R. Rice, D.M. Tracey, On the ductile enlargement of voids in triaxial stress fields*, *Journal of the Mechanics and Physics of Solids* 17(3) (1969) 201-217.
- [16] A.L. Gurson, Continuum theory of ductile rupture by void nucleation and growth: Part I—Yield criteria and flow rules for porous ductile media, *Journal of engineering materials and technology* 99(1) (1977) 2-15.
- [17] G. Avramovic-Cingara, C.A. Saleh, M. Jain, D. Wilkinson, Void nucleation and growth in dual-phase steel 600 during uniaxial tensile testing, *Metallurgical and materials transactions A* 40(13) (2009) 3117.
- [18] A. Hosokawa, D.S. Wilkinson, J. Kang, E. Maire, Effect of triaxiality on void growth and coalescence in model materials investigated by X-ray tomography, *Acta Materialia* 60(6-7) (2012) 2829-2839.
- [19] C.C. Tasan, J.P.M. Hoefnagels, E.C.A. Dekkers, M.G.D. Geers, Multi-Axial Deformation Setup for Microscopic Testing of Sheet Metal to Fracture, *Experimental Mechanics* 52 (2012) 669-678.
- [20] C. Tian, D. Ponge, L. Christiansen, C. Kirchlechner, On the mechanical heterogeneity in dual phase steel grades: Activation of slip systems and deformation of martensite in DP800, *Acta Materialia* (2019).
- [21] C. Du, Micro-plasticity characterization of martensite, ferrite, and dual-phase steel, Ph. D. Thesis, Technische Universiteit Eindhoven, Eindhoven, The Netherlands, 2016.
- [22] J. Lemaitre, J. Dufailly, Damage measurements, *Engineering Fracture Mechanics* 28(5-6) (1987) 643-661.
- [23] T. De Geus, F. Maresca, R. Peerlings, M. Geers, Microscopic plasticity and damage in two-phase steels: On the competing role of crystallography and phase contrast, *Mechanics of Materials* 101 (2016) 147-159.
- [24] C.C. Tasan, M. Diehl, D. Yan, C. Zambaldi, P. Shanthraj, F. Roters, D. Raabe, Integrated experimental-simulation analysis of stress and strain partitioning in multiphase alloys, *Acta Materialia* 81 (2014) 386-400.
- [25] C. Tasan, J. Hoefnagels, M. Geers, Indentation-based damage quantification revisited, *Scripta materialia* 63(3) (2010) 316-319.

- [29] T.W.J. de Geus, F. Maresca, R.H.J. Peerlings, M.G.D. Geers, Microscopic plasticity and damage in two-phase steels: On the competing role of crystallography and phase contrast, *Mechanics of Materials* 101 (2016) 147-159.
- [30] M. Calcagno, Y. Adachi, D. Ponge, D. Raabe, Deformation and fracture mechanisms in fine. and ultrafine-grained ferrite/martensite dual-phase steels and the effect of aging, *Acta Materialia* 59 (2011) 658-670.
- [31] S. Joo, J.K. Lee, J. Koo, S. Lee, D. Suh, H.S. Kim, Method for measuring nanoscale local strain in a dual phase steel using digital image correlation with nanodot patterns, *Scripta Materialia* 68 (2013) 245-248.
- [32] G. Hirt, A.E. Tekkaya, T. Clausmeyer, J. Lohmar, Potential and status of damage controlled forming processes, *Production Engineering* (2020).
- [33] M. Zubair, S. Sandlöbes-Haut, M.A. Wollenweber, K. Bugelnig, C.F. Kusche, G. Requena, S. Korte-Kerzel, Strain heterogeneity and micro-damage nucleation under tensile stresses in an Mg–5Al–3Ca alloy with an intermetallic skeleton, *Materials Science and Engineering: A* 767 (2019) 138414.
- [34] F. Archie, X. Li, S. Zaefferer, Micro-damage initiation in ferrite-martensite DP microstructures: A statistical characterization of crystallographic and chemical parameters, *Materials Science and Engineering A* 701 (2017) 302-313.
- [35] M. Calcagno, D. Ponge, E. Demir, D. Raabe, Orientation gradients and geometrically necessary dislocations in ultrafine grained dual-phase steels studied by 2D and 3D EBSD, *Materials Science and Engineering A* 527 (2010) 2738-2746.
- [36] D. Krajcinovic, Continuous damage mechanics revisited: basic concepts and definitions, (1985).
- [37] Y. Ososkov, D.S. Wilkinson, M. Jain, T. Simpson, In-situ measurement of local strain partitioning in a commercial dual-phase steel, *International journal of materials research* 98(8) (2007) 664-673.
- [38] M. Diehl, D. An, P. Shanthraj, S. Zaefferer, F. Roters, D. Raabe, Crystal plasticity study on stress and strain partitioning in a measured 3D dual phase steel microstructure, *Physical Mesomechanics* 20(3) (2017) 311-323.
- [39] J. Kadkhodapour, A. Butz, S.Z. Rad, Mechanisms of void formation during tensile testing in a commercial, dual-phase steel, *Acta Materialia* 59 (2011) 2575-2588.
- [40] Q. Lai, O. Bouaziz, M. Gouné, L. Brassart, M. Verdier, G. Parry, A. Perlade, Y. Bréchet, T. Pardoen, Damage and fracture of dual-phase steels: Influence of martensite volume fraction, *Materials Science and Engineering A* 646 (2015) 322-331.
- [41] C.C. Tasan, Micro-mechanical characterization of ductile damage in sheet metal, Eindhoven University of Technology, Eindhoven, 2010.
- [42] G. Avramovic-Cingara, Y. Ososkov, M.K. Jain, D.S. Wilkinson, Effect of martensite distribution on damage behaviour in DP600 dual phase steels, *Materials Science and Engineering* 516 (2009) 7-16.
- [43] M. Mazinani, W. Poole, Effect of martensite plasticity on the deformation behavior of a low-carbon dual-phase steel, *J Metallurgical materials transactions A* 38(2) (2007) 328-339.
- [44] M. Nouroozi, H. Mirzadeh, M. Zamani, Effect of microstructural refinement and intercritical annealing time on mechanical properties of high-formability dual phase steel, *Materials Science and Engineering: A* 736 (2018) 22-26.
- [45] C.C. Tasan, M. Diehl, D. Yan, M. Bechtold, F. Roters, L. Schemmann, C. Zheng, N. Peranio, D. Ponge, M. Koyama, An overview of dual-phase steels: advances in microstructure-oriented processing and micromechanically guided design, *Annual Review of Materials Research* 45 (2015) 391-431.
- [46] C.C. Tasan, J.P.M. Hoefnagels, M. Diehl, D. Yan, F. Roters, D. Raabe, Strain localization and damage in dual phase steels investigated by coupled in-situ deformation experiments and crystal plasticity simulations, *International Journal of Plasticity* 63 (2014) 198-210.
- [47] C. Thomser, V. Uthaisangskuk, W. Bleck, Influence of martensite distribution on the mechanical properties of dual phase steels: experiments and simulation, *Steel research international* 80(8) (2009) 582-587.
- [48] O. Hering, A. Dunlap, A.E. Tekkaya, A. Aretz, A. Schwedt, Characterization of damage in forward rod extruded parts, *International Journal of Material Forming* (2019) 1-12.
- [49] E. Aşık, E. Perdahcioğlu, A. van den Boogaard, Microscopic investigation of damage mechanisms and anisotropic evolution of damage in DP600, *Materials Science and Engineering: A* 739 (2019) 348-356.
- [50] C. Tian, D. Ponge, L. Christiansen, C. Kirchlechner, On the mechanical heterogeneity in dual phase steel grades: Activation of slip systems and deformation of martensite in DP800, *Acta Materialia* 183 (2020) 274-284.
- [51] A.C. Darabi, H.R. Chamani, J. Kadkhodapour, A.P. Anaraki, A. Alaie, M.R. Ayatollahi, Micromechanical analysis of two heat-treated dual phase steels: DP800 and DP980, *Mechanics of Materials* (2017).

- [52] T.W.J. de Geus, R.H.J. Peerlings, M.G.D. Geers, Microstructural topology effects on the onset of ductile failure in multi-phase materials – A systematic computational approach, *International Journal of Solids and Structures* 67-68 (2015) 326-339.
- [53] T.W.J. de Geus, R.H.J. Peerlings, M.G.D. Geers, Competing damage mechanisms in a two-phase microstructure: How microstructure and loading conditions determine the onset of fracture, *International Journal of Solids and Structures* 97-98 (2016) 687-698.
- [54] D. Yan, C.C. Tasan, D. Raabe, High resolution in situ mapping of microstrain and microstructure evolution reveals damage resistance criteria in dual phase steels, *Acta Materialia* 96 (2015) 399-409.
- [55] C.C. Roth, T.F. Morgeneyer, Y. Cheng, L. Helfen, D. Mohr, Ductile damage mechanism under shear-dominated loading: In-situ tomography experiments on dual phase steel and localization analysis, *International Journal of Plasticity* 109 (2018) 169-192.
- [56] T.F. Morgeneyer, L. Helfen, H. Mubarak, F. Hild, 3D digital volume correlation of synchrotron radiation laminography images of ductile crack initiation: an initial feasibility study, *Experimental Mechanics* 53(4) (2013) 543-556.
- [57] E.M. C. Landron, O. Bouaziz, J. Adrien, L. Lecarme, A. Bareggi, Validation of void growth models using X-ray microtomography characterization of damage in dual phase steels, *Acta Materialia* 59 (2011) 7564-7573.
- [58] K. Matoy, T. Detzel, M. Müller, C. Motz, G. Dehm, Interface fracture properties of thin films studied by using the micro-cantilever deflection technique, *Surface Coatings Technology* 204(6-7) (2009) 878-881.
- [59] E. Tarleton, D. Balint, J. Gong, A. Wilkinson, A discrete dislocation plasticity study of the micro-cantilever size effect, *Acta Materialia* 88 (2015) 271-282.
- [60] W. Luo, C. Kirchlechner, X. Fang, S. Brinckmann, G. Dehm, F. Stein, Influence of composition and crystal structure on the fracture toughness of NbCo₂ Laves phase studied by micro-cantilever bending tests, *Materials & Design* 145 (2018) 116-121.
- [61] C. Motz, T. Schöberl, R. Pippan, Mechanical properties of micro-sized copper bending beams machined by the focused ion beam technique, *Acta Materialia* 53(15) (2005) 4269-4279.
- [62] S. Brinckmann, K. Matoy, C. Kirchlechner, G. Dehm, On the influence of microcantilever pre-crack geometries on the apparent fracture toughness of brittle materials, *Acta Materialia* 136 (2017) 281-287.
- [63] A.K. Saxena, S. Brinckmann, B. Völker, G. Dehm, C. Kirchlechner, Experimental conditions affecting the measured fracture toughness at the microscale: Notch geometry and crack extension measurement, *Materials & Design* 191 (2020) 108582.
- [64] N. Jaya B, V. Jayaram, S.K. Biswas, A new method for fracture toughness determination of graded (Pt, Ni) Al bond coats by microbeam bend tests, *Philosophical Magazine* 92(25-27) (2012) 3326-3345.
- [65] S. Liu, J. Wheeler, P. Howie, X. Zeng, J. Michler, W. Clegg, Measuring the fracture resistance of hard coatings, *Applied Physics Letters* 102(17) (2013) 171907.
- [66] C.F. Kusche, A. Dunlap, F. Pütz, C. Tian, C. Kirchlechner, A. Aretz, A. Schwedt, T. Al-Samman, S. Münstermann, S. Korte-Kerzel, Efficient characterization tools for deformation-induced damage at different scales, *Production Engineering* 14(1) (2020) 95-104.
- [67] C. Du, J. Hoefnagels, R. Vaes, M. Geers, Block and sub-block boundary strengthening in lath martensite, *Scripta Materialia* 116 (2016) 117-121.
- [68] Y. Tokuda, S. Tsurekawa, D.A. Molodov, Local mechanical properties in the vicinity of $(11\bar{1}0)\Sigma 3/[111]$ symmetric tilt grain boundary in aluminum bicrystal, *Materials Science and Engineering: A* 716 (2018) 37-41.
- [69] S. Schröders, S. Sandlöbes, C. Birke, M. Loeck, L. Peters, C. Tromas, S. Korte-Kerzel, Room temperature deformation in the Fe₇Mo₆ μ -Phase, *International Journal of Plasticity* 108 (2018) 125-143.
- [70] C. Zehnder, K. Czerwinski, K.D. Molodov, S. Sandlöbes-Haut, J.S.-L. Gibson, S. Korte-Kerzel, Plastic deformation of single crystalline C14 Mg₂Ca Laves phase at room temperature, *Materials Science & Engineering: A* 759 (2019) 754-761.
- [71] S. Korte, W. Clegg, Discussion of the dependence of the effect of size on the yield stress in hard materials studied by microcompression of MgO, *Philosophical Magazine* 91(7-9) (2011) 1150-1162.
- [72] R. Soler, J.M. Wheeler, H.-J. Chang, J. Segurado, J. Michler, J. Llorca, J.M. Molina-Aldareguia, Understanding size effects on the strength of single crystals through high-temperature micropillar compression, *Acta Materialia* 81 (2014) 50-57.
- [73] R. Chen, S. Sandlöbes, C. Zehnder, X. Zeng, S. Korte-Kerzel, D. Raabe, Deformation mechanisms, activated slip systems and critical resolved shear stresses in an Mg-LPSO alloy studied by micro-pillar compression, *Materials & Design* 154 (2018) 203-216.
- [74] A. Chowdhury, E. Kautz, B. Yener, D. Lewis, Image driven machine learning methods for microstructure recognition, *Computational Materials Science* 123 (2016) 176-187.

- [75] M. Müller, D. Britz, L. Ulrich, T. Staudt, F. Mücklich, Classification of Bainitic Structures Using Textural Parameters and Machine Learning Techniques, *Metals* 10(5) (2020) 630.
- [76] S.M. Azimi, D. Britz, M. Engstler, M. Fritz, F. Mücklich, Advanced Steel Microstructural Classification by Deep Learning Methods, *Scientific Reports* 8(2128) (2018).
- [77] B. Han, Y. Lin, Y. Yang, N. Mao, W. Li, H. Wang, K. Yasuda, X. Wang, V. Fatemi, L. Zhou, Deep-Learning-Enabled Fast Optical Identification and Characterization of 2D Materials, *Advanced Materials* (2020) 2000953.
- [78] M. Müller, D. Britz, F. Mücklich, Application of Trainable Segmentation to Microstructural Images Using Low-alloy Steels as an Example, *Practical Metallography* 57(5) (2020) 337-358.
- [79] S. Masubuchi, E. Watanabe, Y. Seo, S. Okazaki, T. Sasagawa, K. Watanabe, T. Taniguchi, T.J.n.D.M. Machida, Deep-learning-based image segmentation integrated with optical microscopy for automatically searching for two-dimensional materials, *J npj 2D Materials Applications* 4(1) (2020) 1-9.
- [80] I. Arganda-Carreras, V. Kaynig, C. Rueden, K.W. Eliceiri, J. Schindelin, A. Cardona, H. Sebastian Seung, Trainable Weka Segmentation: a machine learning tool for microscopy pixel classification, *Bioinformatics* 33(15) (2017) 2424-2426.
- [81] F.-Z. Dai, B. Wen, Y. Sun, H. Xiang, Y. Zhou, Theoretical prediction on thermal and mechanical properties of high entropy (Zr_{0.2}Hf_{0.2}Ti_{0.2}Nb_{0.2}Ta_{0.2}) C by deep learning potential, *Journal of Materials Science Technology* 43 (2020) 168-174.
- [82] Z. Yang, Y.C. Yabansu, R. Al-Bahrani, W.-k. Liao, A.N. Choudhary, S.R. Kalidindi, A. Agrawal, Deep learning approaches for mining structure-property linkages in high contrast composites from simulation datasets, *Computational Materials Science* 151 (2018) 278-287.
- [83] J. Zhang, X. Liu, S. Bi, J. Yin, G. Zhang, M. Eisenbach, Robust data-driven approach for predicting the configurational energy of high entropy alloys, *Materials & Design* 185 (2020) 108247.
- [84] K. Kaufmann, D. Maryanovsky, W.M. Mellor, C. Zhu, A.S. Rosengarten, T.J. Harrington, C. Oses, C. Toher, S. Curtarolo, K.S. Vecchio, Discovery of high-entropy ceramics via machine learning, *J Npj Computational Materials* 6(1) (2020) 1-9.
- [85] K.T. Butler, D.W. Davies, H. Cartwright, O. Isayev, A. Walsh, Machine learning for molecular and materials science, *Nature* 559(7715) (2018) 547-555.
- [86] N. Vajragupta, P. Wechsuanmanee, J. Lian, M. Sharaf, S. Münstermann, A. Ma, A. Hartmaier, W. Bleck, The modeling scheme to evaluate the influence of microstructure features on microcrack formation of DP-steel: The artificial microstructure model and its application to predict the strain hardening behavior, *Computational materials science* 94 (2014) 198-213.
- [87] F. Pütz, M. Henrich, N. Fehleemann, A. Roth, S. Münstermann, Generating Input Data for Microstructure Modelling: A Deep Learning Approach Using Generative Adversarial Networks, *Materials* 13(19) (2020) 4236.
- [88] F. Pütz, M. Henrich, A. Roth, M. Könnemann, S. Münstermann, Reconstruction of Microstructural and Morphological Parameters for RVE Simulations with Machine Learning, *Procedia Manufacturing* 47 (2020) 629-635.
- [89] M. Ceriotti, Unsupervised machine learning in atomistic simulations, between predictions and understanding, *The Journal of Chemical Physics* 150(15) (2019) 150901.
- [90] V.L. Deringer, N. Bernstein, A.P. Bartók, M.J. Cliffe, R.N. Kerber, L.E. Marbella, C.P. Grey, S.R. Elliott, G. Csányi, Realistic atomistic structure of amorphous silicon from machine-learning-driven molecular dynamics, *The journal of physical chemistry letters* 9(11) (2018) 2879-2885.
- [92] S. Medghalchi, C.F. Kusche, E. Karimi, U. Kerzel, S. Korte-Kerzel, Damage Analysis in Dual-Phase Steel Using Deep Learning: Transfer from Uniaxial to Biaxial Straining Conditions by Image Data Augmentation, *JOM* (2020) 1-11.
- [93] J. Sander, M. Ester, H.-P. Kriegel, X. Xu, Density-Based Clustering in Spatial Databases: The Algorithm GDBSCAN and Its Applications, *Data Mining and Knowledge Discovery* 2(2) (1998) 169-194.
- [94] C. Szegedy, V. Vanhoucke, S. Ioffe, J. Shlens, Z. Wojna, Rethinking the inception architecture for computer vision, *Proceedings of the IEEE conference on computer vision and pattern recognition*, 2016, pp. 2818-2826.
- [95] G. Pharr, W. Oliver, Measurement of thin film mechanical properties using nanoindentation, *MRS Bulletin* 17(7) (1992) 28-33.
- [96] V. Maier-Kiener, K. Durst, Advanced nanoindentation testing for studying strain-rate sensitivity and activation volume, *JOM* 69(11) (2017) 2246-2255.
- [97] M. Heller, J.S.K.-L. Gibson, R. Pei, S. Korte-Kerzel, Deformation of μm - and mm -sized Fe₂Si single- and bi-crystals with a high angle grain boundary at room temperature, *Acta Materialia* (2020).
- [98] M. Zapara, E. Augenstein, D. Helm, Prediction of damage in cold bulk forming processes, *Pamm* 14(1) (2014) 1037-1040.

Publications part of this Dissertation

[15 - Publ. #1] C. Kusche, T. Reclik, M. Freund, T. Al-Samman, U. Kerzel, S. Korte-Kerzel, Large-area, high-resolution characterisation and classification of damage mechanisms in dual-phase steel using deep learning, PloS one 14(5) (2019) e0216493.

[16 - Publ. #2] C.F. Kusche, F. Pütz, S. Münstermann, T. Al-Samman, S. Korte-Kerzel, On the effect of strain and triaxiality on void evolution in a heterogeneous microstructure – A statistical and single void study of damage in DP800 steel, Materials Science and Engineering: A 799 (2021) 140332.

[21 - Publ. #3] R. Meya, C.F. Kusche, C. Löbbbe, T. Al-Samman, S. Korte-Kerzel, A.E. Tekkaya, Global and High-Resolution Damage Quantification in Dual-Phase Steel Bending Samples with Varying Stress States, Metals 9(3) (2019) 319.

[91 - Publ. #4] C.F. Kusche, J.S.K.-L. Gibson, M.A. Wollenweber, S. Korte-Kerzel, On the mechanical properties and deformation mechanisms of manganese sulphide inclusions, Materials & Design (2020) 108801.

Curriculum Vitae

Personal Information

Surname, Given Names	Kusche, Carl Felix
Adress	Adenauerallee 135a, 52066 Aachen
Nationality	German
Date of Birth	22. May 1992
Place of Birth	Cologne, Germany
E-Mail	carl.kusche@rwth-aachen.de

Professional experience

Since 05/2017	Institute for Physical Metallurgy and Materials Physics, RWTH Aachen University, Aachen, Germany Research associate: -Mesoscale damage characterisation in DP800 dual-phase steel -Electron microscopy and EBSD -Teaching assistant for "Werkstoffphysik" / "Materialkunde"
02/2020 and 09/2020	EMPA, Thun, Switzerland Visiting researcher: - μ -tensile testing
Since 2018	Transregio 188 (DFG) Head of work group "Efficient damage characterisation"
04/2017	Master thesis, Institute for Physical Metallurgy and Metal Physics, RWTH Aachen University, Aachen, Germany <i>"Growth of Al bicrystals with specifically oriented isolated grains and evaluation of grain shrinkage behaviour"</i> Final grade 1,0

07/2016 – 08/2016	Hydro Aluminium R&D, Bonn Internship research and development: Heat treatment of automotive Al alloys, Quality control of rolled Al products
10/2014 – 04/2017	Institute for Physical Metallurgy and Metal Physics, RWTH Aachen University, Aachen, Germany Research student: Growth of Al bicrystals Student tutor: Exercise “Werkstoffphysik” / “Materialkunde”
06 /2015	Bachelor thesis, Institute for Physical Metallurgy and Metal Physics, RWTH Aachen University, Aachen, Germany <i>“Faceting and migration of mixed tilt/twist grain boundaries close to {110} twin boundaries”</i> Final grade 1,3
07/2014 – 08/2014	CNC Knauf, Aachen, Germany Internship: metalworking, welding

Education

04/2012 – 04/2017	RWTH Aachen University, Aachen, Germany Werkstoffingenieurwesen, Bachelor / Master of Science Final grade 1.9
10/2009 – 04/2012	RWTH Aachen University, Aachen, Germany Physik
06/2009	Collegium Augustinianum Gaesdonck, Goch, Germany Abitur Final Grade 1,4

List of publications

C. Kusche, T. Reclik, M. Freund, T. Al-Samman, U. Kerzel, S. Korte-Kerzel, *Large-area, high-resolution characterisation and classification of damage mechanisms in dual-phase steel using deep learning*, PloS one 14(5) (2019) e0216493.

R. Meya, C.F. Kusche, C. Löbbe, T. Al-Samman, S. Korte-Kerzel, A.E. Tekkaya, *Global and High-Resolution Damage Quantification in Dual-Phase Steel Bending Samples with Varying Stress States*, Metals 9(3) (2019) 319.

C.F. Kusche, F. Pütz, S. Münstermann, T. Al-Samman, S. Korte-Kerzel, *On the effect of strain and triaxiality on void evolution in a heterogeneous microstructure – A statistical and single void study of damage in DP800 steel*, Materials Science and Engineering: A 799 (2021) 140332.

C.F. Kusche, J.S.K.-L. Gibson, M.A. Wollenweber, S. Korte-Kerzel, *On the mechanical properties and deformation mechanisms of manganese sulphide inclusions*, Materials & Design (2020) 1088

S. Medghalchi, C.F. Kusche, E. Karimi, U. Kerzel, S. Korte-Kerzel, *Damage Analysis in Dual-Phase Steel Using Deep Learning: Transfer from Uniaxial to Biaxial Straining Conditions by Image Data Augmentation*, JOM (2020) 1-11

C.F. Kusche, A. Dunlap, F. Pütz, C. Tian, C. Kirchlechner, A. Aretz, A. Schwedt, T. Al-Samman, S. Münstermann, S. Korte-Kerzel, *Efficient characterization tools for deformation-induced damage at different scales*, Production Engineering 14(1) (2020) 95-104

M. Zubair, S. Sandlöbes-Haut, M.A. Wollenweber, K. Bugelnig, C.F. Kusche, G. Requena, S. Korte-Kerzel, *Strain heterogeneity and micro-damage nucleation under tensile stresses in an Mg–5Al–3Ca alloy with an intermetallic skeleton*, Materials Science and Engineering: A 767 (2019) 138414

M. Zubair, S. Sandlöbes., M.A. Wollenweber, C.F. Kusche, W. Hildebrandt, C. Broeckmann, S. Korte-Kerzel (2019). *On the role of Laves phases on the mechanical properties of Mg-Al-Ca alloys*. Materials Science and Engineering: A, 756, 272-283.